

Dissertation for Doctor of Philosophy

Ultrasound Medical Imaging:
A Novel Super-Resolution Imaging Technique
Utilizing Random Interference

by

Pavel S. Ni

School of Electrical Engineering and Computer Science

Gwangju Institute of Science and Technology

2021

박 사 학 위 논 문

초음파 의료 영상:

랜덤 간섭을 활용하는 새로운 초 고해상도 영상
기법

니 파 벨

전 기 전 자 컴 퓨 터 공 학 부

광 주 과 학 기 술 원

2021

Ultrasound Medical Imaging:
A Novel Super-Resolution Imaging Technique
Utilizing Random Interference

Advisor: Professor Heung-No Lee

by

Pavel S. Ni

School of Electrical Engineering and Computer Science

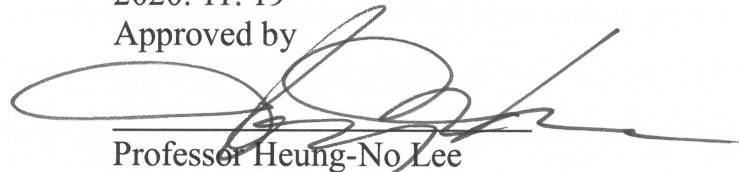
Gwangju Institute of Science and Technology

A dissertation submitted to the faculty of the Gwangju Institute of Science and Technology in partial fulfillment of the requirements for the degree of Doctor of Philosophy in the Science of Electrical Engineering and Computer Science

Gwangju, Republic of Korea

2020. 11. 19

Approved by



Professor Heung-No Lee
Committee Chair

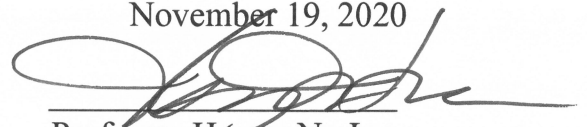
Ultrasound Medical Imaging:
A Novel Super-Resolution Imaging Technique
Utilizing Random Interference

Pavel S. Ni

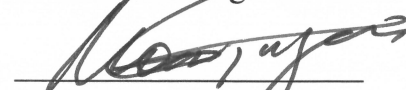
Accepted in partial fulfillment of the requirements for
the degree of Doctor of Philosophy

November 19, 2020

Committee Chair


Professor Heung-No Lee

Committee Member


Professor Moongu Jeon

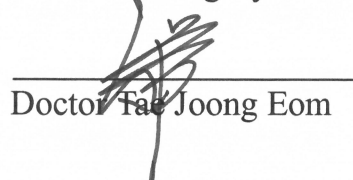
Committee Member


Professor Jong Won Shin

Committee Member


Professor Gregory T. Clement

Committee Member


Doctor Tae Joong Eom

To my parents

Ph.D./EC
20124020

Pavel S. Ni, Ultrasound Medical Imaging: A Novel Super-Resolution Imaging Technique Utilizing Random Interference. School of Electrical Engineering and Computer Science, 2021. 119p.

Abstract

Medical imaging modalities are used every day in hospitals to examine medical conditions, consequently allowing us to analyze anatomical, physiological, metabolic, and functional information of the human body. Ultrasound is one of the most widely used diagnostic tools because it is affordable and non-invasive. Ultrasound is used to assess the tissue, vessels, and organs within the human body. In the past few decades, a lot of effort was put by the academic community to improve the quality of ultrasound images. However, despite decades of innovation, the main disadvantage of ultrasound is low image resolution.

In this dissertation, we develop a novel super-resolution imaging technique utilizing constructive and destructive interference of ultrasonic waves. In particular, we first introduce a method to generate an incident ultrasonic wavefront of random interference. This wavefront then has a spatially variant property that yields individual spatial points, in the region of interest, to reflect mutually incoherent spatial impulse responses. Second, we develop an image reconstruction method based on an L_1 -norm minimization algorithm that is capable of identifying the scattering points by the presence of spatial impulse responses in the received echo signals.

The natural synergy between the properties of the wavefront of random interference and the image reconstruction algorithm allowed us to create the necessary conditions for a successful reconstruction of super-resolution ultrasound images. Lastly, we demonstrate using numerical simulations and phantom experiments that the proposed method can achieve four times better spatial resolution. In the simulation study, the proposed method achieved a resolution of 0.25 mm. In the real phantom experiment, we demonstrated that the proposed method can successfully reconstruct ultrasound images of nylon wires as small as 0.08 mm in diameter using a tissue-mimicking phantom. We argue that the proposed method is a big step towards achieving super-resolution ultrasound imaging and offers a new perspective on ultrasound imaging. The proposed imaging method bypasses the diffraction resolution limit by eliminating the need for the conventional focused ultrasound beam.

©2021

Pavel S. Ni

ALL RIGHTS RESERVED

List of Contents

Abstract.....	i
List of Contents	iii
List of Tables	vi
List of Figures.....	vii
Chapter 1	1
Introduction.....	1
1.1. Contributions and Outline.....	2
Chapter 2	4
Biomedical Imaging	4
2.1. Ultrasound imaging.....	4
2.1.1. Basics of Acoustics.....	6
2.1.2. Ultrasound Imaging Modes	9
2.1.3. Resolution of Ultrasound.....	11
2.1.4. Compressed Sensing.....	12
2.1.5. Related Work.....	13
2.2. Overview of Biomedical Imaging Modalities.....	14
2.2.1. Optical imaging	14
2.2.2. Optoacoustic imaging.....	18
2.2.3. X-ray CT.....	20
2.2.4. Magnetic resonance imaging	22
2.2.5. Positron emission tomography	22
2.3. Summary.....	23
Chapter 3	25

A Novel Interference-based Imaging.....	25
3.1. Motivation.....	25
3.2. Random Interference.....	27
3.3. Interference-based Imaging	30
3.3.1. System Description.....	30
3.3.2. Image Reconstruction – Compound	33
3.3.3. Image Reconstruction – Joint	37
3.3.4. Random Excitation Signals.....	39
3.3.5. Theoretical Resolution.....	43
Chapter 4	46
Research Equipment.....	46
4.1. Research Ultrasound Equipment	46
4.2. Operating Instructions.....	49
4.3. System Control Script.....	52
4.4. Data Acquisition and Test Measurements	55
Chapter 5	59
Simulation and Experimental Results.....	59
5.1. Simulation Study	59
5.1.1. Image Reconstruction – Compound	61
5.1.2. Image Reconstruction – Joint	67
5.2. Experimental Study.....	68
5.2.1. Transmission Matrices – Experimental Study.....	73
5.2.2. Experimental Results – Compound	78
5.2.3. Experimental Results – Joint	84
Chapter 6	90

Conclusion	90
Acknowledgment.....	92
Curriculum Vitae	93
References.....	94

List of Tables

Table 1.1 Dependency of Image Quality On The Number of Array Elements	65
Table 1.2 Mean-squared error (MSE), peak signal-to-noise ratio (PSNR), signal-to-noise ratio (SNR), and structural similarity index (SSIM) values for conventional and proposed imaging methods.	68

List of Figures

Figure 2.1 Biomedical imaging modalities.....	5
Figure 2.2 Focusing and steering are the basic components in the formation of an ultrasound image. a) a focused ultrasound pulse is achieved by appropriately delaying the excitation signals, b) similarly, an ultrasound beam can be steered in different directions.....	6
Figure 2.3 Imaging modes of ultrasound. a) conventional focused B-mode displays the amplitude of the echo signals as brightness, b) M-mode uses a single ultrasound beam to display tissue displacement over time, c) Pulsed Wave Doppler mode displays spectral information of moving tissue and flow of fluids, and provides audio signal, d) Color flow mode displays motion and flow in larger area where direction of motion encoded in color.	8
Figure 2.4 Spatial resolution. In conventional ultrasound, the lateral resolution depends on width an ultrasound beam. Axial resolution depends on duration of an ultrasound beam.	10

Figure 2.5 Types of microscopes.	16
Figure 2.6 Examples of microscopic images.	17
Figure 2.7 Optoacoustic imaging.	19
Figure 2.8 Optoacoustic image of two 10 μm diameter tungsten wires in a water tank.	19
Figure 2.9 X-ray and CT imaging.	20
Figure 2.10 X-ray and X-ray CT images of head.	21
Figure 2.11 Diagram of MRI scanner	22
Figure 2.12 MRI and PET-MRI images of human brain.	23
Figure 3.1 System description of the proposed method. The elements of the linear transducer	

are excited with random signals. The transmitted wavefront has a spatially randomized pressure distribution due to the interference of several ultrasound waves. The columns of the transmission matrix are derived from the spatial impulse response of individual points on the virtual grid. Owing to the effect of interference of random signals, the spatial impulse responses have low mutual coherence. The high-resolution ultrasound images

can be reconstructed from recorder ultrasound echo signals and the transmission matrix.

.....26

Figure 3.2 A wavefront of random interference is reflected from a group of scatterers and

received echo signals visualized as grayscale images: (a) the group of point scatterers

consists of four points located at lateral distances of -5, -1, 1, and 5 mm, respectively; (b)

the group of point scatterers located at lateral distances of -4.75, -1, 1, and 5 mm

respectively; and c) absolute difference between image (a) and image (b).27

Figure 3.3 Illustration of an acoustic system model.29

Figure 3.4. Examples of random excitation signals. (a) random excitation signal $w_1(t)$ and (b)

random excitation signal $w_2(t)$ 40

Figure 3.5. Simulated ultrasound signals of two point scatterers with lateral separation of 0.5

mm: when only two array elements transmitted random signals.41

Figure 3.6. Simulated ultrasound signals of point scatterers with lateral separation of 0.5 mm:

when all 128 array elements transmitted random signals.41

Figure 4.1. Image of the experimental setup.....	47
Figure 4.2. Block-diagram of research scanner.	48
Figure 4.3. Transducer and dimension of the piezoelectric elements; a) height, b) width, and c) separation of elements.....	48
Figure 4.4. User interface – main display.	49
Figure 4.5. 2D imaging controls (UI – touch screen).	50
Figure 4.6. Research system controls (UI – touch screen).	50
Figure 4.7. Script controls (UI – touch screen).....	51
Figure 4.8. Script controls (UI – touch screen).....	51
Figure 4.9. An example of transmit waveform Tw defined in a script.	53
Figure 4.10. An example of transmit instance Tx defined in a script.	53
Figure 4.11. An example of receipt Rx instance defined in a script.	54
Figure 4.12. An example of buffer defined in a script.	54
Figure 4.13. An example of buffer defined in a script.	55

Figure 4.14. Experimental setup three different targets: a plastic plane mounted on metal frame, a metal rode, and a plastic sphere.	56
Figure 4.15. Water tank measurements of echo signal reflected off a plastic plane, a metal rode, and a plastic sphere.	57
Figure 4.16. Experimental setup with a hydrophone.	58
Figure 5.1. Simulation study using a two-point phantom. The phantom features two point targets that are 45 mm from the transducer array with a 0.25-mm separation in the lateral direction between the targets. (a) Image of the scatterer map; (b) image of the focused B-mode method; (c) image of the proposed method. (d) The ultrasound signal acquired at the single receiving channel is plotted in blue; this signal consists of the superposition of impulse responses that correspond to two point targets. The red plot is the reconstructed signal using the interference-based method. (e) Plot of the intensity profiles of the original image, focused B-mode image, and the image obtained using the proposed method. Images are shown with a 60 dB dynamic range.....	60

Figure 5.2. Simulation study using the Shepp–Logan phantom. (a) Original phantom image; (b) reconstruction using the focused b-mode method; (c) reconstruction using the interference based method. Images are shown with 60 dB dynamic range.62

Figure 5.3. Intensity profiles from the Shepp–Logan phantom study. Image intensity profiles are taken at 45 mm in the axial direction. Blue color indicates intensity profile of the original scatterer map. Orange color indicates intensity profile of focused B-mode, and red color indicates intensity profile of interference-based method.62

Figure 5.4. Simulation study on dependence of image quality on the number of receiving elements. (a) original image of the Shepp–Logan phantom. (b)-(h) represent corresponding ultrasound images when different numbers of receiving elements are used. The details of different array configurations are given in Table I. Images are shown with 60 dB dynamic range.63

Figure 5.5. Simulation results: (a) scattering map of a Shepp–Logan phantom; (b) an image reconstructed using conventional focused B-mode; (c) an image reconstructed using

synthetic aperture beamforming; (d) an image reconstructed using previously proposed interference-based compound reconstruction method; and (e) an image reconstructed using the proposed interference-based joint image reconstruction method.66

Figure 5.6. Raw RF data acquired during a real phantom experiment. Each line corresponds to a single RF signal acquired using one of the 128 array elements when all of the array’s elements were simultaneously excited with the proposed random excitation signals.69

Figure 5.7. Raw RF data acquired during a real phantom experiment. Comparison of the RF signals acquired using 64-th element of the array. The RF signal acquired using the conventional focused B-mode method is plotted in black; the sampled RF signal features strong reflections from nylon wires at 1, 2, 3 and 4 cm depths, respectively. The RF signal acquired at the 64-th element of the array using the proposed interference-based method is plotted in blue; the sampled RF signal features strong echo reflections across all time samples..... 70

Figure 5.8. Analysis of the bandwidth of echo signals. a) bandwidth of echo signal acquired using conventional focused B-mode, b) bandwidth of echo signal acquired using random interference method.....	71
---	----

Figure 5.9. Echo signals of the proposed excitation signals measured in the water tank experiment for the corresponding pair of transducer elements (j,i) . Only the first $j = 1$ transmitting element were activated; all N_{Rx} receiving elements were used to receive the echo signals	74
---	----

Figure 5.10. Echo signals of the proposed excitation signals measured in the water tank experiment for the corresponding pair of transducer elements (j,i) . Each transmitting element j was assigned with a unique random excitation signal. The transmitting elements were activated one by one. The receiving element $i = 1$ is used to record echo signals.....	75
--	----

Figure 5.11. The delayed echo signals of the proposed excitation signals measured in the water tank experiment for the corresponding pair of transducer elements (j,i) and the spatial point at \mathbf{r}_k	76
--	----

Figure 5.12. Illustration of how a subset of spatial points is selected using acceptance angle of the array element.	77
---	----

Figure 5.13. Experimental results using a vertical/horizontal target groups of the tissue mimicking phantom. A side-by-side comparison of the region with vertical/horizontal groups (a) the image reconstructed using the conventional focused B-mode (delay-and-sum-beamforming) method; (b) an image reconstructed using the proposed interference-based method. Images are shown with 60 dB dynamic range.	80
---	----

Figure 5.14. Experimental results using a high-resolution target groups of the tissue mimicking phantom. (a) the image reconstructed using the conventional focused B-mode method (delay-and-sum-beamforming); (b) an image reconstructed using the proposed	
--	--

interference-based method. (c)–(d) a two time magnified images of the conventional and	
the proposed methods. All images are shown with 60 dB dynamic range.....	81
Figure 5.15. Experimental results. Images of a dental floss in the water tank: a) conventional	
B-mode, b) plane-wave mode, c) synthetic aperture, d) joint image reconstruction method	
using random interference.....	85
Figure 5.16. Experimental results using tissue mimicking phantom. The ROI includes seven	
0.1-mm-diameter nylon wires and a cyst. a) conventional B-mode, b) plane-wave mode,	
c) synthetic aperture, d) joint image reconstructions method using random interference	86
Figure 5.17. Experimental results using tissue mimicking phantom. The ROI includes twelve	
0.08-mm-diameter nylon wires. a) conventional B-mode, b) plane-wave mode, c)	
synthetic aperture, d) joint image reconstructions method using random interference	88

Chapter 1

Introduction

Ultrasound is a versatile imaging modality with many imaging modes and practical applications. Diagnostic ultrasound is universally accepted as the preferred modality because it is non-invasive and affordable. However, in conventional ultrasound, the axial and lateral resolution is limited by diffraction. We argue that the diffraction limit applies only to systems that use focused ultrasound pulses. Achieving ultrasound resolution beyond the diffraction limit would significantly improve the accuracy of medical diagnosis. To achieve significant improvements in resolution, we believe that it is insufficient to modify only the signal processing (software) part without modifications to the imaging protocol (hardware). The main contribution of this dissertation is improving the spatial resolution of ultrasound. We develop a new imaging method that uses an incident ultrasound wavefront of random interference and an L1-minimization algorithm. The synergy between the properties of random interference and the image reconstruction algorithm allowed us to create a perfect condition for super-resolution ultrasound imaging. The feasibility of the proposed method has been tested using numerical simulations and real phantom experiments.

1.1. Contributions and Outline

In this dissertation, we demonstrate a new interference-based method that improves the spatial resolution of ultrasound. We propose using a novel unfocused transmission of excitation signals coded with pseudorandom sequences that yields an incident wavefront of random interference. The received echo signals are the result of multiple reflections of the incident ultrasound wavefront from the scatterers. Super-resolution ultrasound images are reconstructed using the *a priori* measurements of spatial impulse responses of individual point scatterers and an L_1 -norm minimization algorithm. An ultrasound research system has been developed that is capable of generating the proposed wavefront of random interference. The feasibility of the proposed method has been tested using numerical simulations and real phantom experiments.

In Chapter 2 we provide a detailed introduction to ultrasound imaging. We explain the basic principles of ultrasound imaging, sound-matter interactions, and discuss the resolution limit of ultrasound. We also provide an overview of other biomedical imaging modalities such as optical microscopy, optoacoustic, X-ray computed tomography (X-ray CT), magnetic resonance imaging (MRI), and positron emission tomography (PET). Understanding the physics mechanisms, and properties of various imaging modalities was an essential step in the development of the proposed random interference imaging method.

In Chapter 3 we introduce the proposed Super-resolution ultrasound imaging method called Random Interference Imaging. In the proposed method, ultrasound images reconstructed using *a priori* measurements of spatial impulse responses and the L_1 -norm minimization algorithm. We provide a system description of the interference based imaging method and propose two image reconstruction methods: random interference compound method and random interference joint method. We provide a detailed description and analysis of the proposed method

and demonstrate new resolution capabilities. The content of this chapter is based on two published peer-reviewed journal papers of Pavel S. Ni and Heung-No Lee [1][2].

In Chapter 4 we provide descriptions of used equipment and detailed instructions to obtain simulation and experimental data which can be used to reproduce this research. We describe the procedures used to generate ultrasound data.

In Chapter 5 we present simulation and experimental results. We compare our results with conventional ultrasound imaging methods and explain the importance of our work.

Finally, in Chapter 6 we identify the remaining challenges, outline our future work, and conclude the outcomes of this dissertation.

Chapter 2

Biomedical Imaging

The focus of this Chapter is to introduce different biomedical imaging modalities. While the main focus of this dissertation is improving the spatial resolution of ultrasound, we would like to start with an overview of ultrasound, optical microscopy, optoacoustic, X-ray computed tomography, magnetic resonance imaging, and positron emission tomography. Today, biomedical imaging modalities utilize a wide range of electromagnetic spectrum and sound. A short comparison of biomedical imaging modalities is given in Figure 2.1. We believe that understanding the physics and mechanisms of various imaging modalities helped us to establish a big picture perspective. It was an important step towards correctly identifying the present and future challenges in ultrasound imaging.

2.1. Ultrasound imaging

The ultrasound is an imaging device that uses a high-frequency sound source to image the internal body parts. Sound is a mechanical wave that requires a medium to propagate. Ultrasound imaging works according to the pulse-echo principle: an incident ultrasound wave is transmitted into a medium in which waves are partially reflected back to an array of transducers.

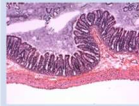
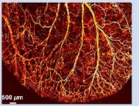

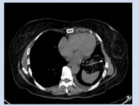
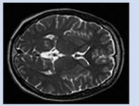
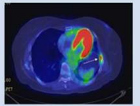
	Optical	Photoacoustic	Ultrasound	CT	MRI	PET/SPECT
Images						
Source	▪Light	▪Light ▪Sound	▪Sound	▪X-ray	▪Magnetic field	▪γ-rays
PROS	▪Real-time ▪Contrast Resolution	▪Contrast Resolution	▪Availability ▪Cost ▪Real-time	▪Sensitivity Resolution	▪Sensitivity Resolution	▪Contrast Resolution
CONS	▪Depth	▪Depth ▪Real-time	▪Contrast ▪Speckle	▪Contrast Radiation	▪Cost ▪Throughput	▪Cost ▪Radiation Throughput
Resolution	▪0.1 μm	▪10 μm	▪0.3–1 mm	▪50–200 μm	▪25–100 μm	▪2–10 mm

Figure 2.1 Biomedical imaging modalities.

Subsequently, the signals received at the array are processed to create the final ultrasound image. Sound waves interact with a medium through transmission, reflection, refraction, scattering, absorption, attenuation, and diffraction. Spatial resolution in conventional sonography is achieved through focusing and steering of an ultrasound beam [3], see Figure 2.2. The resolution in ultrasound imaging varies spatially and depends on parameters such as frequency of the transmitted signal, beam width, size of the aperture, and transmit focal depth. These parameters restrict the ability to focus the ultrasound waves, thus imposing a physical limitation on the final resolution. Similar to optical imaging, ultrasound resolution is defined by the diffraction limit [4]. The theoretical spatial resolution in ultrasound imaging, for a single-cycle pulse, is equal to half the acoustic wavelength [5][6]. However, the best axial and lateral resolution is several times lower than the diffraction limit due to high ultrasound attenuation and speckle noise [7]. Modern ultrasound scanners are capable to achieve a spatial resolution of 0.3–1 mm and an imaging depth up to 15 cm.

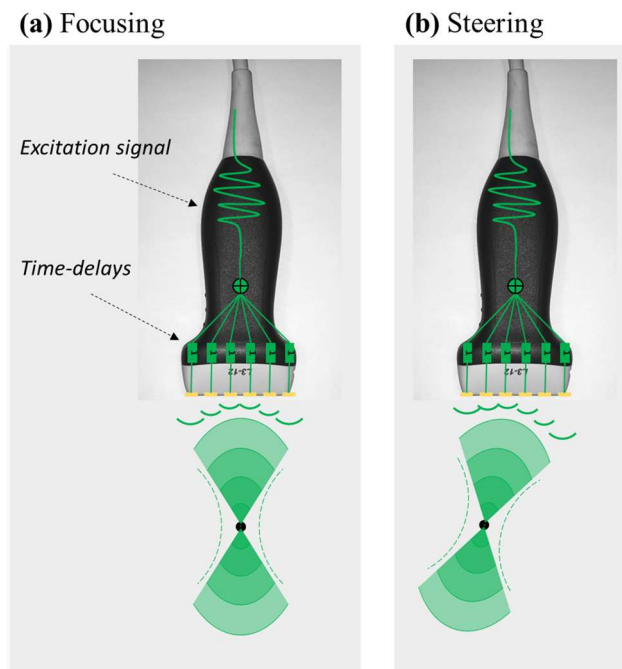


Figure 2.2 Focusing and steering are the basic components in the formation of an ultrasound image. a) a focused ultrasound pulse is achieved by appropriately delaying the excitation signals, b) similarly, an ultrasound beam can be steered in different directions.

2.1.1. Basics of Acoustics

In this section, we review the physics of sound generation, sound propagation, and sound-matter interaction. In ultrasound, a transducer consisting of an array of piezoelectric elements is used to generate an incident ultrasonic wavefront and record backscattered echo signals. Piezoelectric elements generate mechanical vibrations when exposed to an electrical field. When piezoelectric elements of the transducer array are excited with electrical signals a rapid vibration of elements produces a sound wave. Similarly, when piezoelectric elements undergo mechanical stress the elements produce an electrical charge. A sound wave has a frequency, wavelength, and propagation speed. Frequency of sound refers to the number of cycles of compressions and rarefactions per second. In ultrasound, we use high-frequency sound

waves in the range of 3–15 MHz. The sound wavelength refers to a distance between two identical points of a sound wave. The speed of sound refers to how fast sound waves propagate and depends on the density of the tissue. The human body has a complex tissue structure, often we use the speed of sound in water as an approximation because tissue contains a high amount of water.

The energy of sound propagates as a series of compression and rarefaction waves of pressure. When ultrasound waves travel through a medium, they undergo a series of physical phenomena such as reflection, scattering, attenuation, etc.

- **Reflection.** Sound waves are reflected from an obstacle or at an interface between two media. Specular reflections occur when the wave encounters large objects with high impedance such as bones. Specular reflection abides the law of reflection, where an angle of the reflected wave is equal to the incident wave. In ultrasound, the amplitude of the reflected echo signals is displayed as brightness.
- **Scattering.** Another type of reflection is scattering also called diffuse reflection. Scattering occurs when the wave encounters rough surfaces or cells of soft tissues. Scattering waves propagate in all directions. In ultrasound, scattering waves create constructive and destructive interference which is displayed as speckle noise.
- **Attenuation.** Sound waves encounter losses as they propagate in the medium. The amplitude of waves becomes smaller. The attenuation is frequency-dependent and losses increase with higher frequencies. The attenuation of sound waves limits imaging depth.

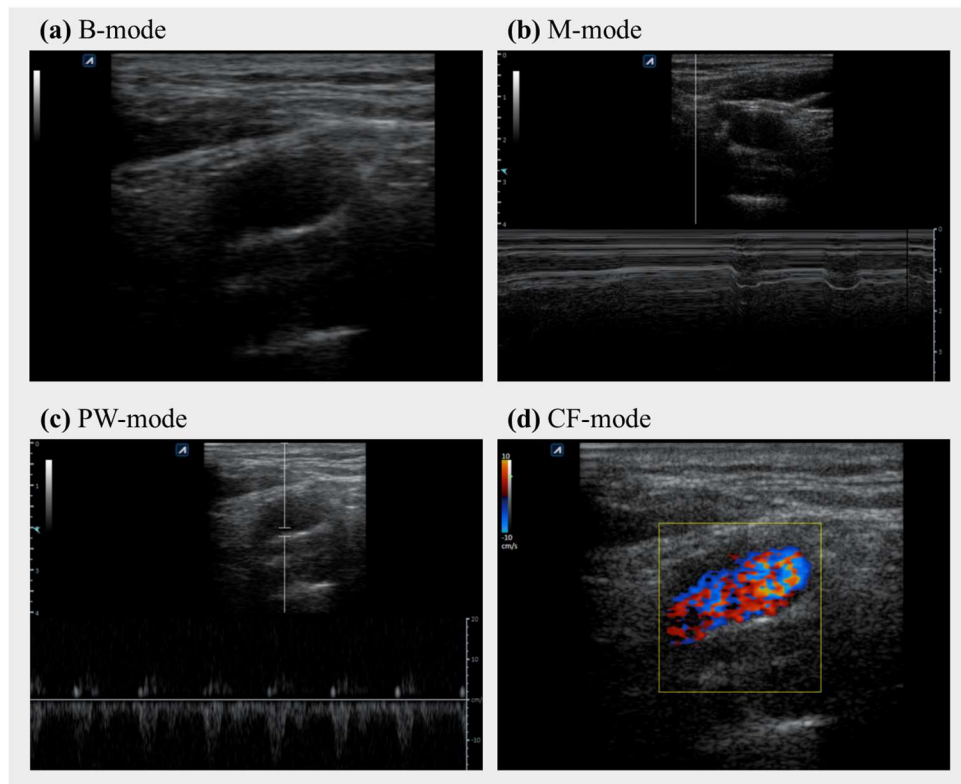


Figure 2.3 Imaging modes of ultrasound. a) conventional focused B-mode displays the amplitude of the echo signals as brightness, b) M-mode uses a single ultrasound beam to display tissue displacement over time, c) Pulsed Wave Doppler mode displays spectral information of moving tissue and flow of fluids, and provides audio signal, d) Color flow mode displays motion and flow in larger area where direction of motion encoded in color.

- **Diffraction.** When a sound wave travels through a medium its energy spreads in a lateral direction. This phenomenon is called diffraction. The diffract effect limits our ability to create a perfectly focused ultrasound pulse. Hence, the resolution of conventional ultrasound systems is diffraction limited.

- **Interference.** When multiple waves meet at the same point they superpose and create a resultant wave of constructive and destructive interference. Interference in ultrasound imaging is treated as an undesirable effect that degrades image quality and creates speckle noise.

2.1.2. Ultrasound Imaging Modes

Ultrasound is a versatile imaging modality with many imaging modes, focusing techniques, and clinical applications. Modern ultrasound scanners provide four main imaging modes: brightness mode (B-mode), motion mode (M-mode), pulsed wave Doppler mode (PW-mode), and color flow mode (CF-mode). B-mode ultrasound is used to generate a two-dimensional image of the anatomical structures of soft tissues. An example of a B-mode image of a thyroid vein is shown in Figure 2.3(a). B-mode image is acquired using an array of transducer that collectively generate a focused ultrasound beam. Multiple transmissions of the beam are used to produce a two-dimensional B-mode image. The image consists of multiple lines called scanlines. A scanline is generated by applying a beamforming operation to the received echo signals. Then, the amplitude (strength) of the beamformed signal is displayed as brightness in the image. M-mode ultrasound is used to accurately measure the motion of organs and muscles. An example of an M-mode image of the thyroid is shown in Figure 2.3(b). The figure consists of a B-mode image and an M-mode trace of a moving thyroid vein. The M-mode image is formed by using a single scanline to measure the displacement of the moving tissue. PW-mode ultrasound uses the Doppler principle that measures the frequency shift in an ultrasound signal caused by the motion of the object. The PW-mode is used to measure blood flow, see Figure 2.3(c). CF-mode is similar to PW-mode. CF-mode uses the Doppler effect to estimate the

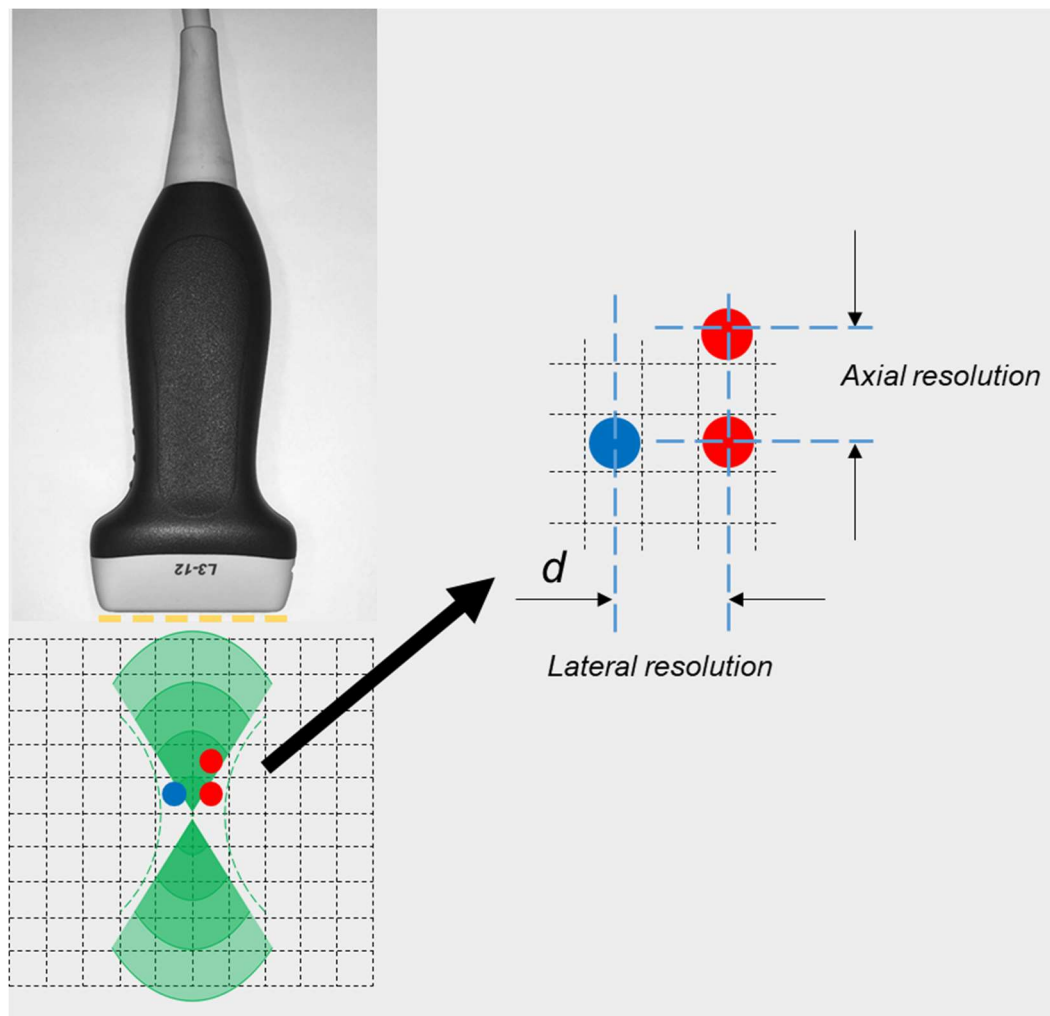


Figure 2.4 Spatial resolution. In conventional ultrasound, the lateral resolution depends on width an ultrasound beam. Axial resolution depends on duration of an ultrasound beam.

movement of blood in a large area and displays the motion as a color. The image of CF-mode is shown in Figure 2.3(d), where the blue color corresponds to motion away from the observer and red towards.

2.1.3. Resolution of Ultrasound

Spatial resolution describes how closely two objects (target points) in space can be estimated separately. Ultrasound has a spatially variant resolution that depends on many factors such as aperture size, center frequency, bandwidth, focal depth, etc. Similar to optical imaging spatial resolution of ultrasound systems limited by the diffraction limit. In ultrasound, we also identify temporal and contrast resolutions. The temporal resolution depends on the frame rate of ultrasound systems and refers to the ability of ultrasound systems to detect rapid movements. The contrast resolution is the ability of the ultrasound system to accurately represent the acoustic reflection properties of the tissue. The spatial resolution of 2D images further could be divided into two components: axial resolution and lateral resolution as shown in Figure 2.4.

Axial resolution refers to the smallest distance separating two objects lying along the axis of the ultrasound beam, at which the objects can be identified in the image. In conventional focusing based ultrasound, the axial resolution is limited by the length of the ultrasound beam. The best axial resolution is equal to two wavelengths λ

$$R_{axial} = \frac{c}{2f_c} \quad (1)$$

where c is the propagation velocity, f_c is the transducer frequency bandwidth. Ultrasound pulse generated with high frequency will give a shorter transmit pulse and therefore a better axial resolution. For typical frequencies in the range of 3–15 MHz, the axial resolution corresponds to 1.0 mm to 0.2 mm.

Lateral resolution refers to the smallest distance separating two objects along the lateral direction or perpendicular to the axis of the ultrasound beam, at which the objects can be identified in the image. The width of the beam determines the effective lateral resolution of the

ultrasound system. The best lateral resolution of conventional ultrasound systems is one wavelength λ of the transmit pulse

$$R_{lateral} = \lambda \cdot f_{\#} \quad (2)$$

where $\lambda = \frac{c}{f_0}$ is the sound wavelength. For typical frequencies in the range of 3–15 MHz,

the lateral resolution corresponds to 0.5 mm to 0.1 mm.

2.1.4. Compressed Sensing

Originally, compressive sensing theory was introduced to reconstruct a signal using fewer measurements than that proposed by the Shannon–Nyquist sampling theorem [17][18][19][20][21]. However, later studies have shown that CS theory can be used to significantly improve the resolution of imaging modalities. During the past few decades, CS theory has been successfully used to improve the resolution of spectrometers, microscopes, and many other imaging modalities [22][23][24][25][26][27][28][29][30].

The concept of classical CS theory can be explained using a system of linear equations $\mathbf{y} = \mathbf{Ax} = \mathbf{\Phi\Psi x}$, where $\mathbf{x} \in \mathbb{R}^N$ is a signal to be reconstructed, $\mathbf{A} \in \mathbb{R}^{M \times N}$ is a specially constructed matrix consisting of a sensing matrix $\mathbf{\Phi}$ and a sparsifying basis $\mathbf{\Psi}$, and $\mathbf{y} \in \mathbb{R}^M$ is a vector representing the signal acquired using a measuring instrument. The goal of CS is to reconstruct \mathbf{x} from \mathbf{y} and \mathbf{G} when $M \ll N$. In such a case, $\mathbf{y} = \mathbf{Ax}$ is an underdetermined system because we have more unknowns than equations. The matrix \mathbf{A} must characterize the transmission properties of the imaging system therefore it is called the transmission matrix. The CS theory guarantees the successful reconstruction of \mathbf{x} under the following two conditions. The first condition requires the signal \mathbf{x} to be sparse in some domains. The signal

is called sparse if K non-zero values of the signal satisfy $K < M \ll N$. The second condition requires a sensing matrix to be incoherent. The matrix is called incoherent when the cross-correlation of its columns is small. Many good algorithms were recently introduced to solve the L1-norm minimization problem and reliably reconstruct the signal of interest. In particular, we use the YALL1 MATLAB package solver [31][32].

Several works have used compressive sensing (CS) theory [19][20][21] to prove the effectiveness of some ultrasound applications. For example, a sub-Nyquist sampling scheme based on CS was proposed in [29] to speed up data acquisition. In [30], a beamforming process was integrated directly into the sub-Nyquist sampling scheme, which yielded an even higher temporal resolution. In [39], CS was applied to STA imaging to reduce the number of firings, which can potentially increase the system frame rate. In [40], a CS framework derived from the ultrasound propagation theory was introduced to reconstruct the complete ultrasound image from the transmission of a single plane wave. Such methods can increase temporal resolution at the cost of computationally complex algorithms.

2.1.5. Related Work

The components of ultrasound resolution can be classified into detail, contrast, and temporal. Various methods have been proposed in the past few decades to improve the image quality in ultrasound systems. For example, enhanced detail and contrast resolution were achieved with the introduction of multi-element transducer arrays and phased arrays [3]. These array types enable advanced beamforming techniques such as plane-wave imaging [10], synthetic transmit aperture (STA) [11], and dynamic focusing [12]. Various filtering techniques have been developed to suppress speckle noise [13][14]. Coded excitation has been used to

achieve extended imaging depth [15]. Other excitation sequences have also been investigated; for example, a delay-encoded transmission scheme was proposed in [16] to increase the signal-to-noise ratio (SNR). Such methods can improve image quality; however, the resolution remains limited by the diffraction.

“Super-resolution” refers to an imaging technique that is capable of imaging objects smaller than the initial wavelength of the transmitted ultrasound signal. Multiple studies have demonstrated the feasibility of super-resolution techniques in ultrasound imaging. For example, in [41][42][6], different techniques were proposed to visualize microvessels and blood flow speed estimation using contrast agents such as microbubbles. However, super-resolution techniques that can be used without contrast agents are limited in acoustic imaging due to high attenuation and the distortion of backscattered signals. A promising super-resolution technique was proposed in [43], which uses a back-projection approach to visualize objects that are entirely within the ultrasound beam.

2.2. Overview of Biomedical Imaging Modalities

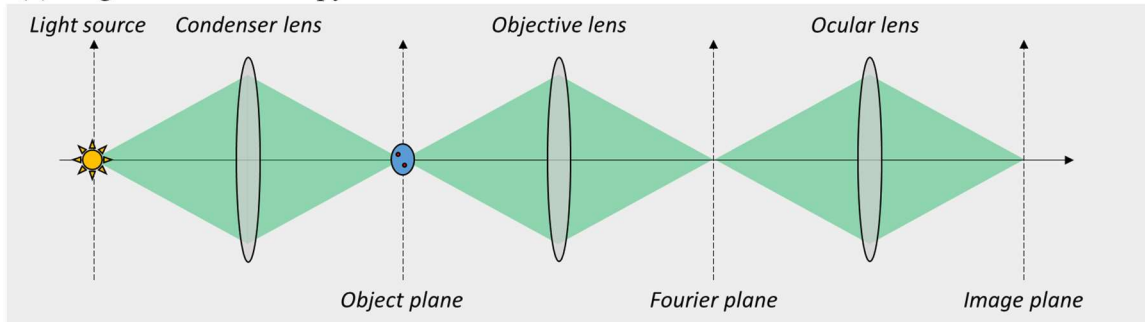
2.2.1. Optical imaging

In this section, we review the basic principles and physics of microscopy. The microscope is an imaging device that uses a light source and optical lenses to achieve a magnified image of an object. The first microscope was invented in the 16th century by Dutch scientist Antonie van Leeuwenhoek. The continuous advancements in microscopy lead to many breakthrough discoveries and gave us several Nobel Prize winners. Nowadays, advanced microscopy techniques allow achieving resolution beyond the diffraction limit of $0.25\text{ }\mu\text{m}$ [8]. The main

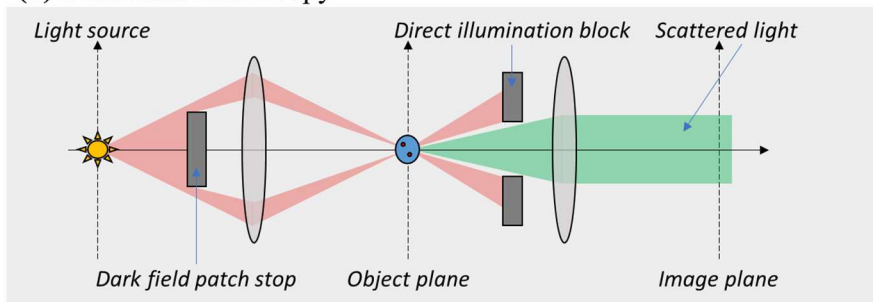
element of microscopy is light, a form of electromagnetic energy that interacts with matter through absorption, scattering, reflection, refraction, dispersion, diffraction, interference, and polarization. Next, we introduce some of the most notable types of microscopy.

Bright-field microscopy is the simplest and most known type of optical microscopy. The diagram of bright-field microscopy is shown in Figure 2.5(a). When illumination light passes through the object plane its energy is absorbed and reflected from the specimen causing the amplitude (brightness) of light to change. The image is a result of the light absorbance difference. However, the specimen absorbs only a small portion of illumination light which

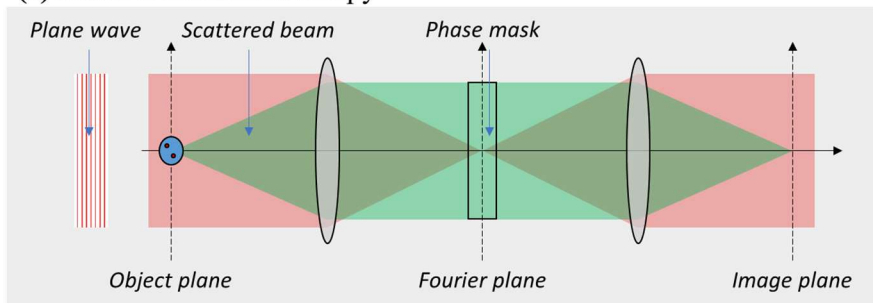
(a) Bright-field microscopy



(b) Dark-field microscopy



(c) Phase contrast microscopy



(d) Confocal microscopy

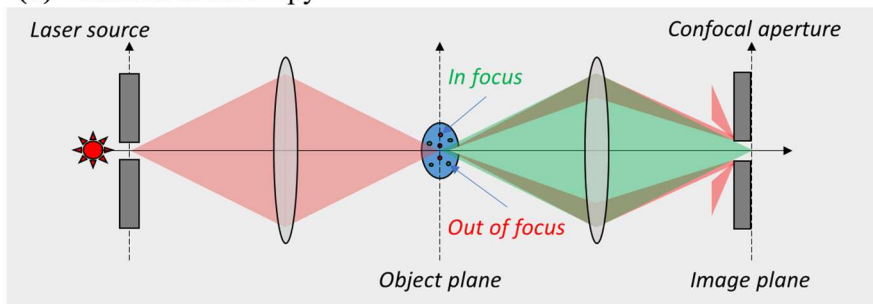


Figure 2.5 Types of microscopes.

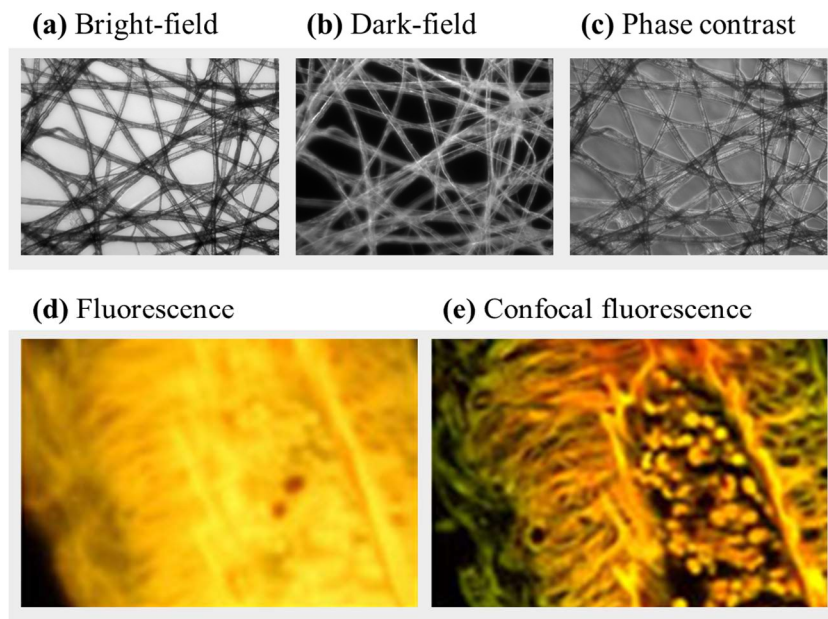


Figure 2.6 Examples of microscopic images.

results in pale images that lack contrast resolution. In bright-field microscopy, the illumination light overpowers the specimen-scattered light. Dark-field microscopy addresses the issue of excessively bright illumination and allows measuring only light scattered from the specimen. The diagram of the dark-field microscope is shown in Figure 2.5(b). The illumination light travels at an angle greater than allowed by the numerical aperture. Dark-field microscopy significantly improves the contrast resolution by preventing illumination light from entering the objective lens. Only the amplitude of the light is used in the bright-field and dark-field microscopes.

Phase-contrast microscopy enables visualization of transparent specimens that do not absorb the light. The diagram of the phase-contrast microscope is shown in Figure 2.5(c). Transparent specimens are not visible because they do not absorb the energy of light. However, when light passes through the specimens its phase slightly changes due to refraction. These

phase shifts are made visible by creating a phase difference of half the wavelength between the specimen-scattered and illumination light which consequently yields destructive interference that can be observed as a wave amplitude (brightness).

Confocal fluorescence microscopy enables three-dimensional visualization of a specimen by utilizing point illumination of fluorescent proteins, multiple focusing depths, and scanning techniques. The diagram of the confocal microscope is shown in Figure 2.5(d). Fluorescent proteins are used to label specific cells in the specimen. Confocal microscopy allows selectively activate fluorescence using point illumination. Then, three-dimensional fluorescent images are obtained using focusing at different depths and scanning across the image plane. In confocal fluorescence microscopy, an image is obtained from fluorescence light which makes the image more accurate compared to the previous microscopy methods.

For a more thorough introduction to optical imaging, we recommend visiting the online resources of Olympus Life Science (www.olympus-lifescience.com).

2.2.2. Optoacoustic imaging

Photoacoustic microscopy is an imaging device that combines principles of optical microscope and ultrasound. Optical microscopy has a limited imaging depth, a few millimeters, because of the high attenuation of light in the tissue. Ultrasound imaging has low resolution because of the diffraction that limits the ability to produce a narrow ultrasound pulse. In photoacoustic microscopy, a fast pulsing laser source is used to illuminate the tissue which consequently yields ultrasound waves. The optoacoustic image is then reconstructed from ultrasound signals. The diagram of the photoacoustic setup is shown in Figure 2.7. The optoacoustic image of two 10 μm diameter tungsten wires is shown in Figure 2.8. The optoacoustic probe consists

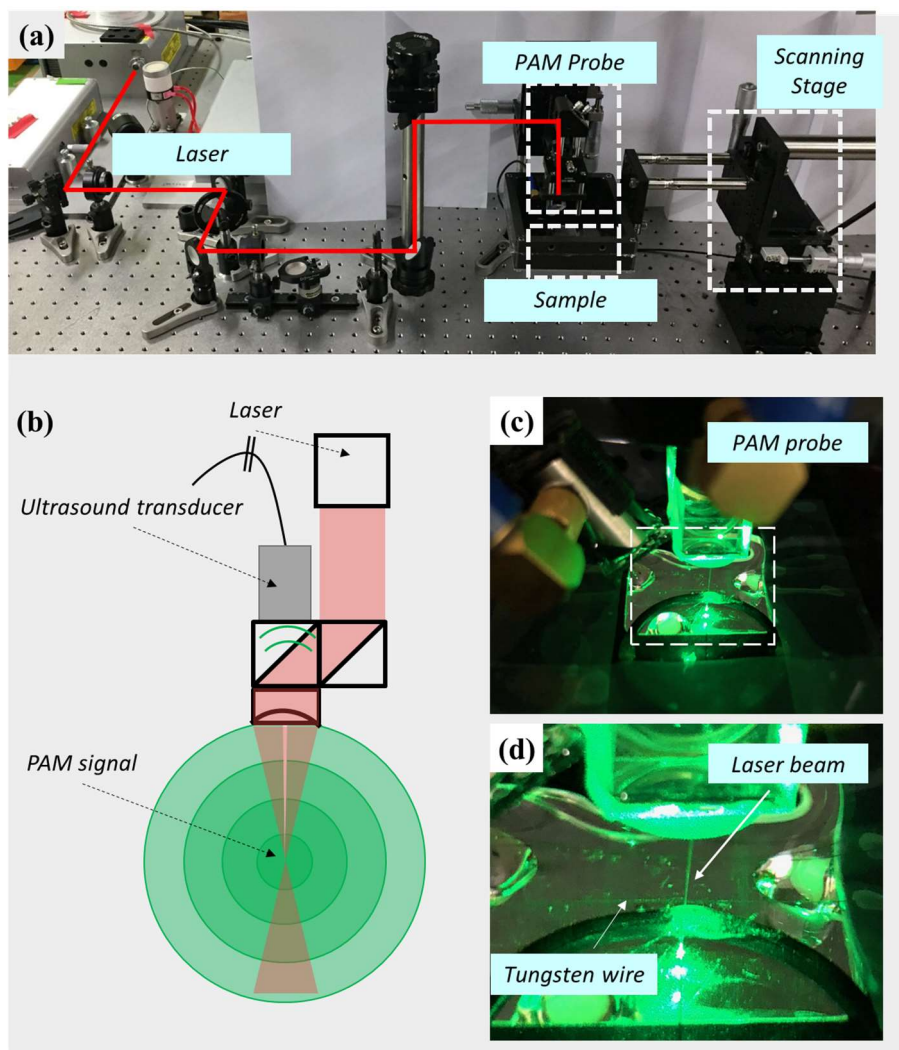


Figure 2.7 Optoacoustic imaging.



Figure 2.8 Optoacoustic image of two 10 μm diameter tungsten wires in a water tank.

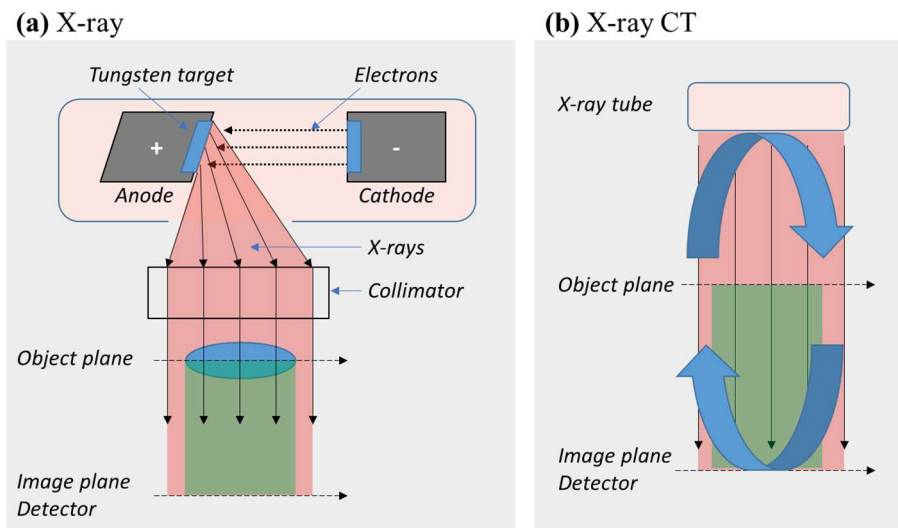


Figure 2.9 X-ray and CT imaging

of a laser source and an ultrasound transducer. The narrow laser beam is used to precisely assess the tissues of a sample and generate localized ultrasound waves at a focal point a few millimeters deep. The laser light disperses inside the tissue which makes obtaining an image of deep tissue impossible. However, laser-generated ultrasound waves have large penetration and are used to reconstruct an image. The photoacoustic microscopy enables deep tissue imaging with a spatial resolution of $10\text{ }\mu\text{m}$.

2.2.3. X-ray CT

X-ray computed tomography or CT is an imaging device that uses high-energy electromagnetic radiation. The X-ray radiation is generated when electrons from the cathode reach the anode. X-ray images are formed from photoelectric absorption by detecting the amount of X-ray energy reaching the detector after passing through the object. The diagram of an X-ray and X-ray CT is shown in Figure 2.9. An image of a single X-ray scan of a human head is

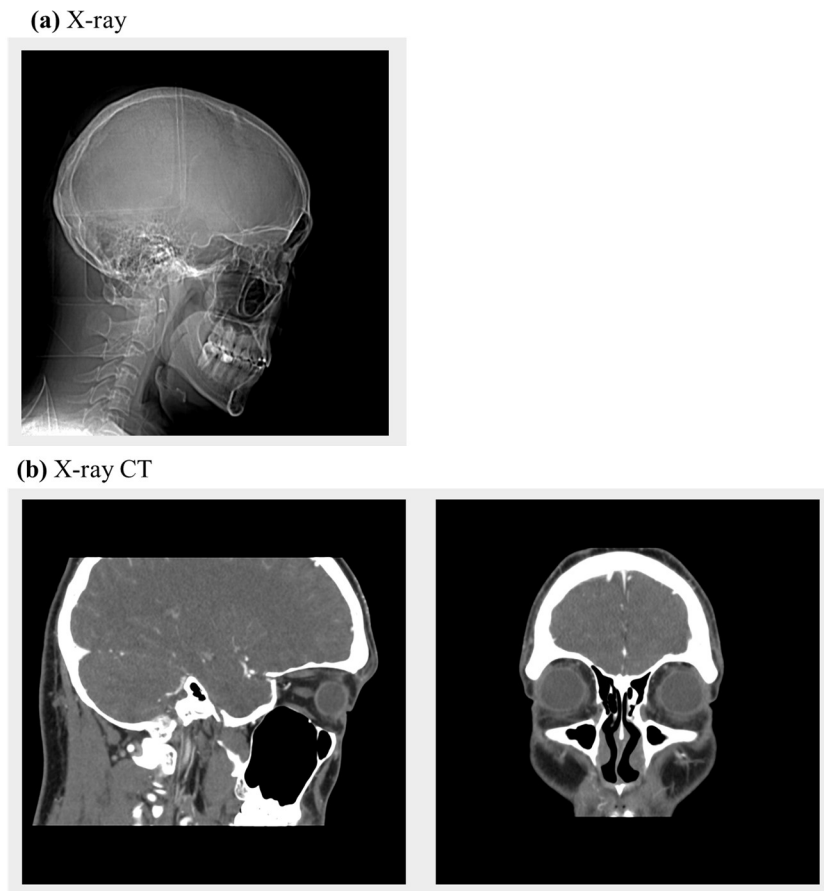


Figure 2.10 X-ray and X-ray CT images of head.

shown in Figure 2.10. A single X-ray image lacks depth information because a three-dimensional object is projected onto a two-dimensional detector. The X-ray CT scanners use multiple X-ray measurements acquired at different angles by rotating the X-ray tube and detector. By using CT techniques all three-dimensions can be reconstructed. Also, CT improves sensitivity to soft tissue. Modern X-ray CT scanners capable to generate tomographic images with 50 μm resolution.

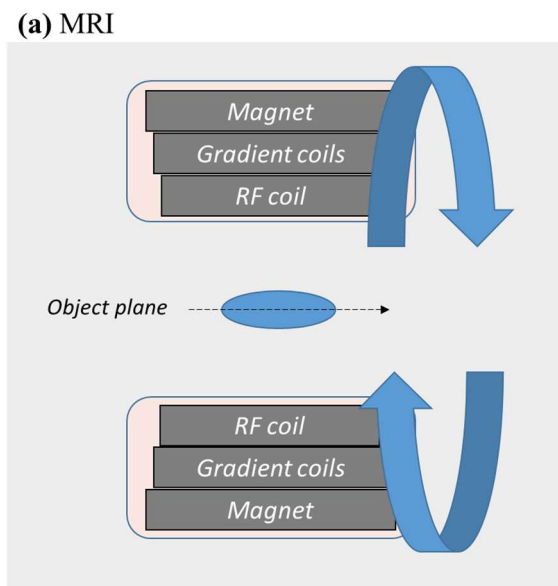


Figure 2.11 Diagram of MRI scanner

2.2.4. Magnetic resonance imaging

Magnetic resonance imaging (MRI) is an imaging device that uses a magnetic field to reconstruct the images of tissue. The diagram of the MRI scanner is shown in Figure 2.11. The MRI images are formed by exposing the tissue to a magnetic field that yields atoms in the tissue to emit radiofrequency (RF) signals which are measured by a receiving coil. MRI is used to examine bones, joints, and soft tissues and provides spatial resolution in the vicinity of 25 – 100 μm . An MRI image of a human brain is shown in Figure 2.12.

2.2.5. Positron emission tomography

Positron emission tomography (PET) and single-photon emission computed tomography (SPECT) are nuclear imaging devices that use radiotracers to measure the metabolic activity of the biological cells. The radiotracers have a positron-emitting radionuclide and are used to mark a specific tissue type. Then the collimated detector is used to determine the direction

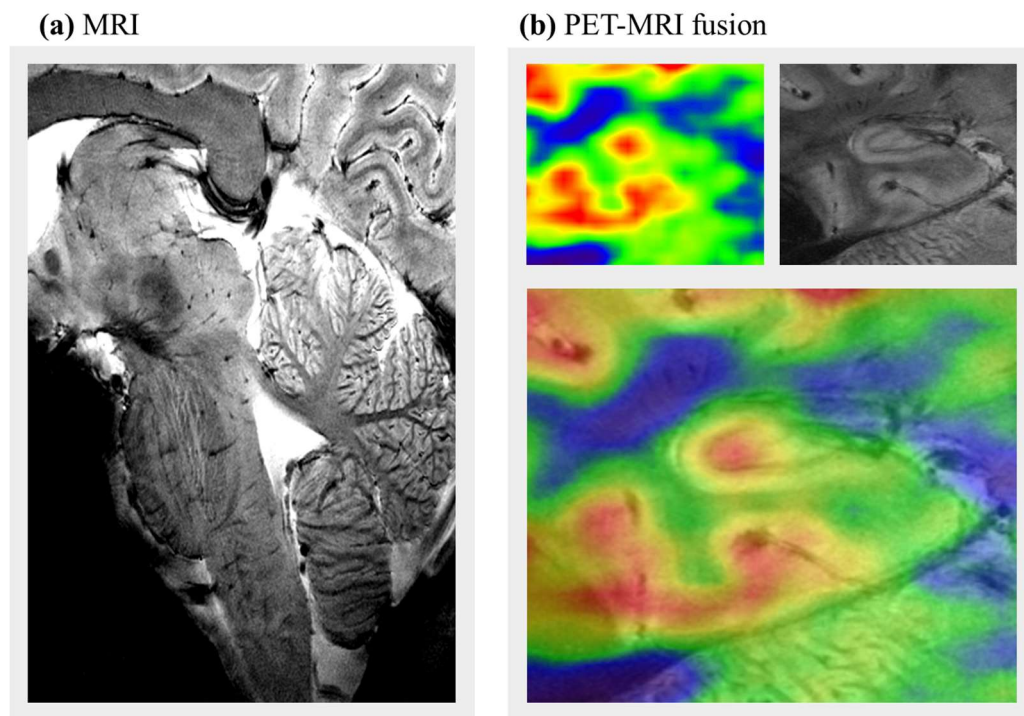


Figure 2.12 MRI and PET-MRI images of human brain.

of photon emission. PET/SPECT scanners are used to image the brain, kidney, and cancer cells at 1–2 mm resolution. A PET image of the human brain is shown in Figure 2.12.

2.3. Summary

There are a lot of similarities between the modalities that we reviewed in this Chapter. We summarize this Chapter by explaining our thought process behind developing random interference imaging. First, we notice how the development of new illumination techniques improved the resolution of microscopes. A strong illumination source can overshadow the evanescent details of the object. Indeed, a focused ultrasound pulse is designed to deliver a large amount of energy along one scanline. Strength of the echo signal visualized as brightness

in the final ultrasound image. Likewise, we can see that by nature ultrasound waves are not easy to focus due to the diffraction effect. For example, in optoacoustic microscopy, the laser-induced ultrasound enables the acquisition of 10 μm resolution images. Second, spatially dividing an object into multiple imaging zones enables significant improvement of confocal microscopy, X-ray CT, and MRI. The human body is a complex structure with multiple layers of tissue yet in ultrasound we usually reconstruct a two-dimensional image of a cross-section of the body. Third, the diffraction resolution limit applies only to the conventional understanding of imaging. For example, in the case of fluorescence microscopy, the fine details of a specimen were made visible by using fluorescent proteins. Similarly, in PET, the metabolic processes can be visualized using different radiotracers. In the proposed method, we reimagined the ultrasound by replacing the conventional focused beam with a wavefront of random interference. The new interference-based approach allowed us to spatially separate individual scatterers based on spatial impulse responses and via advanced signal processing techniques.

Chapter 3

A Novel Interference-based Imaging

3.1. Motivation

In conventional ultrasound imaging, beamforming is usually used to focus ultrasound waves. However, due to acoustic diffraction, the ability to focus an ultrasound beam is limited, which leads to low spatial and contrast resolutions. Recently, advanced statistical and signal processing techniques have allowed the development of imaging methods that are radically different from our traditional understanding of imaging [44]. Such imaging modalities utilize intentionally created randomness in the image acquisition process and extend the boundaries of imaging beyond the existing limits. We show that the resolution of ultrasound systems can be significantly improved if we use an incident ultrasound wavefront of random interference instead of a focused ultrasound beam.

Figure 3.1 shows a schematic illustration of the proposed imaging method. First, the incident ultrasound wavefront is generated by exciting elements of the transducer array using signals coded with random sequences. In these circumstances, individual array elements emit

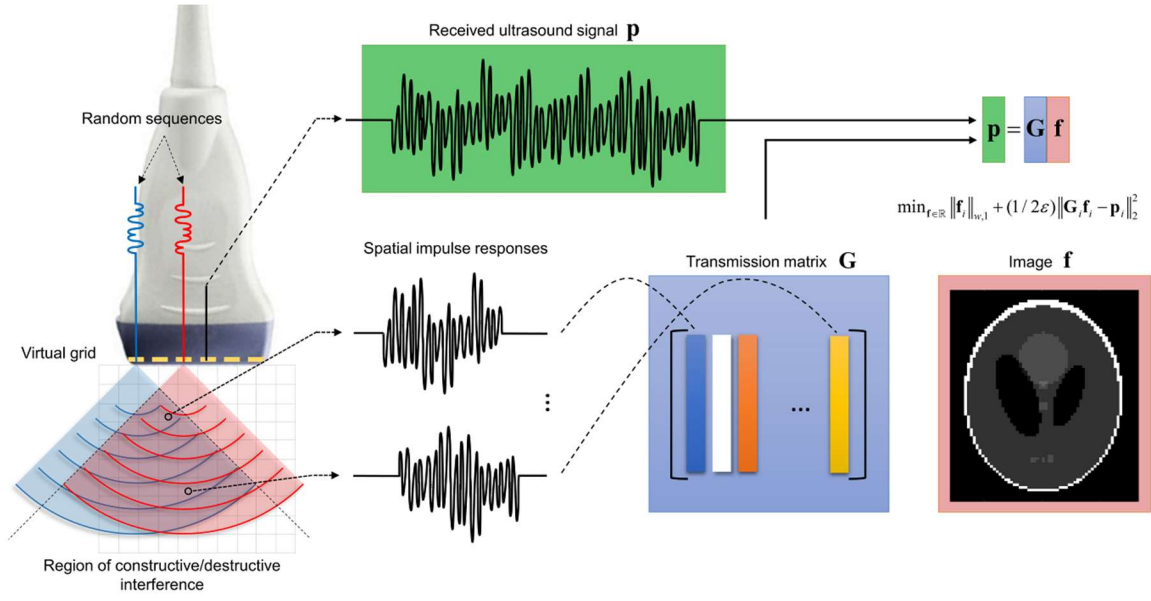


Figure 3.1 System description of the proposed method. The elements of the linear transducer are excited with random signals. The transmitted wavefront has a spatially randomized pressure distribution due to the interference of several ultrasound waves. The columns of the transmission matrix are derived from the spatial impulse response of individual points on the virtual grid. Owing to the effect of interference of random signals, the spatial impulse responses have low mutual coherence. The high-resolution ultrasound images can be reconstructed from recorder ultrasound echo signals and the transmission matrix.

ultrasound waves corresponding to the applied excitation signals. All emitted waves collectively yield a complex ultrasound wavefront of constructive and destructive interference, which we simply named random interference. Traditionally, interference in ultrasound imaging is treated as an undesirable effect that degrades image quality and creates speckle noise. In our proposed work, we aim to utilize random interference and intentionally cause spatial impulse responses of individual point scatterers to be mutually incoherent. Under such an effort, we can recover high-resolution images using both the *a priori* measurements of spatial impulse responses and the l_1 -norm minimization algorithm.

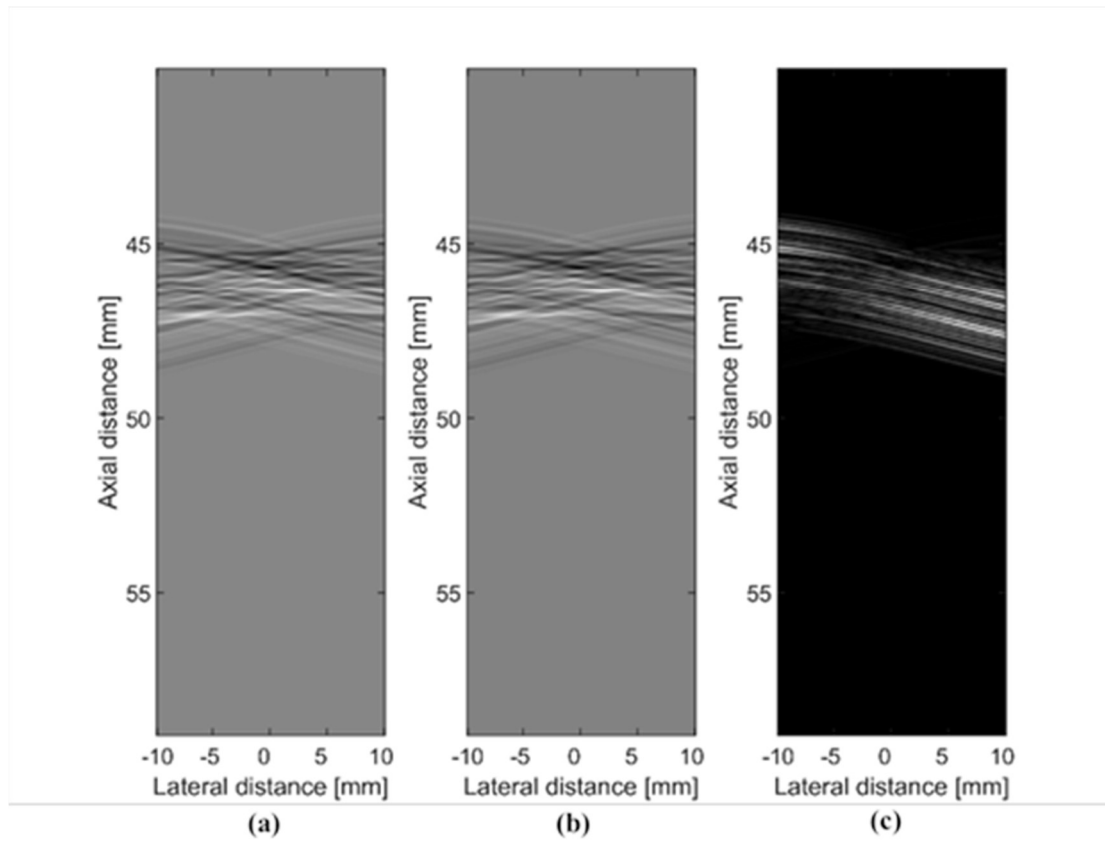


Figure 3.2 A wavefront of random interference is reflected from a group of scatterers and received echo signals visualized as grayscale images: (a) the group of point scatterers consists of four points located at lateral distances of -5, -1, 1, and 5 mm, respectively; (b) the group of point scatterers located at lateral distances of -4.75, -1, 1, and 5 mm respectively; and c) absolute difference between image (a) and image (b).

3.2. Random Interference

In conventional ultrasound imaging, beamforming is used to spatially divide the ROI into several scanlines. An ultrasound image is then acquired one scanline at a time by using beamforming to focus the transmit and receive ultrasound pulses. The image is reconstructed

based on the assumption that the received ultrasound signals consist of echoes reflected only from inhomogeneity within the given scanline. However, in practice, owing to the diffraction effect, the incident wavefront reflects from the medium within the scanline and its adjunct areas [5][6]. In conventional ultrasound, owing to the imperfect coherence of echo signals at the receiver, the beamformed signal is corrupted by interference patterns known as speckle noise [33][34][35]. Thus, in conventional focused methods, ultrasound interference is a highly undesired effect that degrades the image resolution.

Unlike conventional beamforming-based methods, we intentionally create an unfocused ultrasound wavefront of random interference, which yields spatial impulse responses of individual point scatterers in the ROI to be mutually incoherent [1]. Thus spatial resolution can be achieved by identifying individual point scatterers based on their spatial impulse responses.

Here, we demonstrate the effect of random interference using numerical simulation, where a small change in the ROI incurs a significant difference in the received RF signals. In Figure 3.2(a), we show the echo signals of the incident wavefront of random interference reflected from a group of scatterers as grayscale images. In Figure 3.2(a), the ROI includes a group of scatterers consisting of four points located at an axial distance of 45 mm and lateral distances of -5, -1, 1, and 5 mm respectively. In Figure 3.2(b), a group of point scatterers consists of four points located at lateral distances of -4.75, -1, 1, and 5 mm. In Figure 3.2(b), the position of the first scatterer was changed from -5 mm to -4.75 mm. Figure 3.2(c) depicts the absolute difference between the images shown in Figure 3.2(a) and Figure 3.2(b). From Figure 3.2(c), we can see that the effect of random interference yields a significant difference in the received echo signals even when we make a small change to the scatterer map. Using random interference and its effect on the scatterers in the ROI, we can design an imaging scheme where

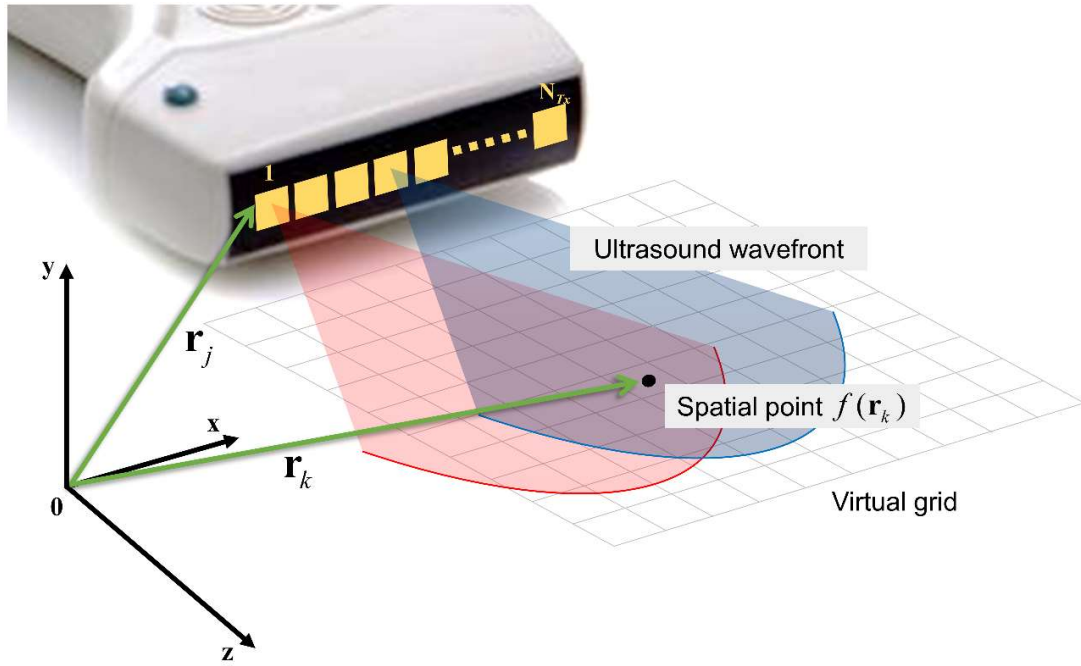


Figure 3.3 Illustration of an acoustic system model.

an ultrasound image is reconstructed using *a priori* information about wave propagation. We represent the entire ROI as a set of individual spatial points. Then, the RF signals received at the sensor array can be decomposed into a set of echo signals reflected from individual point scatterers in the ROI. In a simulation study, *a priori* information can be acquired by generating RF signals for every point scatterer in the ROI, see Chapter 5.1. In the experimental study, *a priori* information can be generated from measurements of a plastic plane submerged into a water tank, see Chapter 5.2.1.

3.3. Interference-based Imaging

We propose using a novel unfocused transmission of excitation signals coded with pseudorandom sequences that yields an incident wavefront of random interference. The received echo signals are the result of multiple reflections of the incident ultrasound wavefront from the scatterers. High-resolution ultrasound images are reconstructed using the *a priori* measurements of spatial impulse responses of individual point scatterers and an L1-norm minimization algorithm. An ultrasound research system has been developed that is capable of generating a wavefront of random interference. The feasibility of the proposed method has been tested using numerical simulations and real phantom experiments.

3.3.1. System Description

Let us consider the pulse-echo ultrasound system shown in Figure 3.3. We consider a linear transducer array with N_{Tx} identical array elements. During transmission, all N_{Tx} elements of the transducer array are simultaneously excited with random signals. During the reception, the same transducer array is used to record the reflected ultrasound signals. We let \mathbf{r}_j , \mathbf{r}_i be the vectors in three-dimensional space. We use \mathbf{r}_j for each $j \in \{1, 2, \dots, N_{Tx}\}$ to indicate the position of the j -th transmitting element. Likewise, the vector \mathbf{r}_i for each $i \in \{1, 2, \dots, N_{Rx}\}$ indicates the position of the i -th receiving element. Similarly, we let the vector \mathbf{r}_k for each $k \in \{1, 2, \dots, N_{Sc}\}$ be the three-dimensional vector which indicates the position of the k -th scatterer on the virtual grid. Thus, there are a total of N_{Sc} scatterers.

We define an ultrasound echo signal reflected off a single scatterer and received at the i -th array element as follows:

$$p_{\text{single}}(\mathbf{r}_i, t) = v(t) \otimes_t f(\mathbf{r}_k) \otimes_r h(\mathbf{r}_k, \mathbf{r}_i, t), \quad (3)$$

where $v(t)$ is the oscillation of the transducer array (i.e., the proposed random excitation signals); $f(\mathbf{r}_k)$ is the signal of interest at the location \mathbf{r}_k ; and $h(\mathbf{r}_k, \mathbf{r}_i, t)$ is the pulse-echo impulse response of the transducer array. We denote the spatial and temporal convolutions using \otimes_r and \otimes_t , respectively.

When the ultrasound wavefront travels through the medium, it is scattered and reflected off a volumetric object within which the density and the propagation velocity differ from those of the surroundings. The signal $f(\mathbf{r}_k)$ of a single scatter object at the location \mathbf{r}_k in (3) is defined as follows:

$$f(\mathbf{r}_k) = \frac{\Delta\rho(\mathbf{r}_k)}{\rho_0} - \frac{2\Delta c(\mathbf{r}_k)}{c_0}, \quad (4)$$

where ρ_0 is the mean density of the medium, c_0 is the speed of sound in the medium, $\Delta\rho$ is the change in density, and Δc is the change in speed at the location \mathbf{r}_k . Here, $f(\mathbf{r}_k)$ represents the signal that we aim to reconstruct from the echo signal $p_{\text{single}}(\mathbf{r}_i, t)$. The equation (3) indicates how the signal of interest $f(\mathbf{r}_k)$ is observed at a receiving element such that it is blurred by the pulse-echo spatial impulse response of the array $h(\mathbf{r}_k, \mathbf{r}_i, t)$ and the transducer oscillation $v(t)$.

The oscillation $v_j(t)$ of the j -th transmit element \mathbf{r}_j in (3) is expressed as

$$v_j(t) = \frac{\rho}{2c^2} E_m(t) \otimes_t \frac{\partial^3 w_j(t)}{\partial t^3}, \quad (5)$$

where $E_m(t)$ is an electro-mechanical response from the transducer; $w_j(t)$ for each $j \in \{1, 2, \dots, N_{Tx}\}$ corresponds to the excitation signal applied to the j -th transmit element. In this Chapter, we propose a new imaging method that requires echo signals reflected from individual point scatterers to be mutually incoherent. The incoherency is obtained by controlling the ultrasound wavefront of random interference. A wavefront of random interference can be generated by exciting each array element with a transmitting signal coded with a random sequence, see $w_j(t)$ in Section 3.3.4. Once emitted, all the random excitation signals $w_j(t)$'s constructively and destructively interfere with each other and produce random interference.

To derive a received ultrasound echo signal, we need to find the pulse-echo impulse response $h(\mathbf{r}_k, \mathbf{r}_i, t)$ of the array. We define the pulse-echo impulse response of the array as

$$h(\mathbf{r}_k, \mathbf{r}_i, t) = \sum_{j=1}^n h_{Tx}(\mathbf{r}_k, \mathbf{r}_j, t) \otimes_t h_{Rx}(\mathbf{r}_i, \mathbf{r}_k, t), \quad (6)$$

where h_{Tx} is the impulse response of the transmitting transducer array, h_{Rx} is the impulse response of the receiving transducer array. In the proposed method, all N_{Tx} elements of the transducer array are simultaneously excited with random signals. The impulse responses h_{Tx} and h_{Rx} are found from

$$h(\mathbf{r}_1, \mathbf{r}_2, t) = \int_S \frac{\delta(t - (|\mathbf{r}_1 - \mathbf{r}_2|/c))}{2\pi|\mathbf{r}_1 - \mathbf{r}_2|} dS, \quad (7)$$

where \mathbf{r}_1 is the location of observation and \mathbf{r}_2 is the origin of the ultrasound wave. The pulse-echo impulse response (6) is the function of the relative distances from each transmitting element \mathbf{r}_j , for each $j \in \{1, 2, \dots, N_{Tx}\}$, to the scatterer at the spatial point \mathbf{r}_k , and back to the receiver at \mathbf{r}_i . The integral over the transducer surface, S , denotes Huygens' Principle.

3.3.2. Image Reconstruction – Compound

Let us consider the region of interest (ROI) from 35 mm to 55 mm in the axial direction and from -10 mm to 10 mm in the lateral direction. We define an ultrasound image as a collection of scatterers on a virtual grid, as shown in Figure 3.3. If we define scatterers in the ROI at equal distance, $d = 0.25$ mm, then we obtain a square region with 81 points in the axial and the lateral directions and a total of $N_{Sc} = 6,561$ point scatterers. To simplify this, we represent a group of scatterers on the virtual grid as a vector, $\mathbf{f} := [f(\mathbf{r}_1) \ f(\mathbf{r}_2) \ \dots f(\mathbf{r}_{N_{Sc}})]$.

We use (3) to find the echo signal reflected from a single scatterer at \mathbf{r}_k . In our simulation, we assume that the propagation of ultrasound waves is linear; thus, we can find echo signals reflected from a group of scatterers, \mathbf{f} , by measuring the impulse responses of individual scatterers and summing them together. Then, the echo signal reflected from a group of scatterers is given by

$$\begin{aligned} p_{\text{group}}(\mathbf{r}_i, t) &= \sum_{k=1}^{N_{Sc}} p_{\text{single}}(\mathbf{r}_i, t) \\ &= \sum_{k=1}^{N_{Sc}} v(t) \otimes_t f(\mathbf{r}_k) \otimes_r h(\mathbf{r}_k, \mathbf{r}_i, t). \end{aligned} \quad (8)$$

Using matrix and vector notations, we can express (8) as

$$\mathbf{p}_i = \mathbf{G}_i \mathbf{f}_i, \quad (9)$$

where $\mathbf{p}_i \in \mathbb{R}^M$ is the column vector representation of a received ultrasound signal, $\mathbf{G}_i \in \mathbb{R}^{M \times N_{sc}}$ is the transmission matrix, and $\mathbf{f}_i \in \mathbb{R}^{N_{sc}}$ is a vectorized object image. Here, M is the number of signal samples and N_{sc} is the total number of point scatterers. The echo signal \mathbf{p}_i at the i -th receiving element is the summation of spatial impulse responses reflected off the scatterers in the ROI. The elements of \mathbf{f} represent the scattering strength of the corresponding spatial point.

In the simulation study, the transmission matrix \mathbf{G}_i is generated from *a priori* measurement of spatial impulse responses obtained in Field II ultrasound software [36][37], see Chapter 5.1.1. The columns of the matrix $\mathbf{G}_i := [\mathbf{g}_{i,1} \ \mathbf{g}_{i,2} \ \mathbf{g}_{i,3} \ \dots \ \mathbf{g}_{i,N_{sc}}]$ represent the spatial responses of individual scatterers, i.e., $\mathbf{g}_{i,k} := p_{\text{single}}(\mathbf{r}_i, t)$. In the experimental study, we propose generating transmission matrices from the measurements of random excitation signals obtained in a water tank experiment, see Chapter 5.2.1.

According to the linear property of the proposed imaging system, any echo signal \mathbf{p}_i of an object image \mathbf{f}_i in (9) can be represented as a combination of columns of the matrix \mathbf{G}_i . In our ultrasound imaging model, we need to reconstruct the unknown object image \mathbf{f}_i given the echo signal \mathbf{p}_i and transmission matrix \mathbf{G}_i . The reconstruction quality of the object image \mathbf{f}_i improves with increasing incoherence of the responses of the point scatterers. To make the spatial impulse responses more incoherent, we propose using unfocused transmission of random excitation signals, see Section 3.3.4. Then, we can reconstruct the image $\hat{\mathbf{f}}_i$ by solving the following optimization problem:

$$\hat{\mathbf{f}}_i := \min_{\mathbf{f}} \|\mathbf{f}_i\|_1 \quad \text{subject to} \quad \|\mathbf{G}_i \mathbf{f}_i - \mathbf{p}_i\|_2^2 \leq \varepsilon, \quad (10)$$

where $\|\cdot\|_1$ denotes the L1-norm and $\varepsilon \geq 0$ is a regularization value. We use the L1-norm minimization algorithm which can provide reliably accurate estimation for sparsely representable signals [31][32]. In [52][53][54], it is shown that the regularization parameter ε affects the quality of a solution to the general L1-norm minimization problem $\min \|x\|_1 + 1/2\varepsilon \|y - Ax\|_2^2$. The best practice of finding a regularization value ε that produces a sub-optimal solution (10) is to find it empirically for each specific case. For example, in [52], the regularization parameter was chosen as $\|2A^T x\|_\infty$. Likewise, in [53], the regularization parameter was chosen as $2\sigma\sqrt{\log n}$. Similarly, the authors in [54] set the regularization parameter as $2\sigma\sqrt{\log n}$ or 10^{-4} . We have chosen ε according to [53][54]. Throughout this study, the regularization parameter ε is set to $\varepsilon = 3 \times 10^{-3}$, which is shown to be efficient in terms of image quality.

In a single pulse-echo transmission, we use $N_{Rx} = 128$ array elements to record raw echo signals. Thus, we solve 128 equations independently, one for each receiving element in the array, as follows:

$$\begin{aligned} \mathbf{p}_1 &= \mathbf{G}_1 \mathbf{f}_1 \\ \mathbf{p}_2 &= \mathbf{G}_2 \mathbf{f}_2 \\ &\vdots \\ \mathbf{p}_{128} &= \mathbf{G}_{128} \mathbf{f}_{128}. \end{aligned} \tag{11}$$

Here, the ultrasound echo signals \mathbf{p}_i and the transmission matrix \mathbf{G}_i depend on the position of the corresponding receiving element i . The object image \mathbf{f}_i itself shall remain the

same throughout each receiving element $i \in \{1, 2, \dots, N_{Rx}\}$. Thus, we can obtain a high-resolution compound image $\mathbf{f}_{compound}$ by summing together all reconstructed images $\hat{\mathbf{f}}_i$ and dividing by a total number of images as follows:

$$\mathbf{f}_{compound} = \left(\sum_{i=1}^{N_{Rx}} \hat{\mathbf{f}}_i \right) / N_{Rx}, \quad (12)$$

where \sum is a sum of all reconstructed images for each receiving element $i \in \{1, 2, \dots, N_{Rx}\}$. In Section 3.3.4, we further discuss how the number of reconstructed images \mathbf{f}_i affects the quality of the final compound image $\mathbf{f}_{compound}$.

The optimization problem (10) can best recover the object image \mathbf{f}_i when the mutual coherence μ among the columns of the matrix \mathbf{G}_i is low. For example, we define the mutual coherence μ of the spatial responses of two points separated by the distance d as follows:

$$\mu(d) := \max_{\substack{k \neq l \\ k, l \in \{1, \dots, N_{Sc}\}}} \frac{|\langle \mathbf{g}_k, \mathbf{g}_l \rangle|}{\|\mathbf{g}_k\|_2 \|\mathbf{g}_l\|_2} \quad (13)$$

where \mathbf{g}_k is the spatial response of the respective point scatterer at \mathbf{r}_k position, \mathbf{g}_l is the spatial response of the point scatterer at \mathbf{r}_l position, and $\langle \cdot, \cdot \rangle$ denotes the inner product. Note that the spatial responses are the result of interference between transmitted excitation signals. If we define the distance d between virtual points as a very small value, then the difference in the path traveled by the transmitted signals would be insignificant; this will yield spatial points with highly coherent spatial responses. In Section 3.3.4, we explain how the proposed random excitation signals $w_j(t)$ affect the coherence of the matrix \mathbf{G}_i . In Section 3.3.5, we

explain the relationship between the proposed excitation signals, the level of coherence of the matrix \mathbf{G}_i , and the best achievable resolution.

3.3.3. Image Reconstruction – Joint

Here, we further improve our results by proposing a joint image reconstruction scheme that combines RF signals from all elements of the sensor array in a single L1-norm minimization problem. As a result, the new proposed imaging scheme is capable of reconstructing more accurate ultrasound images.

When an ultrasound wavefront of random interference propagates through the medium, its energy is partially reflected and received at the transducer array. The RF signals carry information about the same object image $\mathbf{f}_{\text{Object}}$ observed at slightly different angles. In the interference-based joint image reconstruction method, we propose directly reconstructing a high-resolution image by utilizing all signals from the array in a single optimization problem.

First, to estimate the image \mathbf{f} , we need to obtain transmission matrices that carry information about the propagation of the proposed ultrasound wavefront of random interference. We use the spatial impulse responses of individual point scatterers as *a priori* information. We can then reconstruct the ultrasound image using (10). In Equation (9), the image \mathbf{f}_i is reconstructed from an echo signal \mathbf{p}_i acquired at a single receiving channel i . In a single pulse-echo transmission, we use all elements of the array to receive the reflected echo signals. Therefore, we have 128 different versions of (9), one for each receiving element in the array, as in (11). Owing to the effect of random interference, the received ultrasound signals \mathbf{p}_i and the trans-

mission matrices \mathbf{G}_i for each $i \in \{1, 2, \dots, N_{Rx}\}$ carry unique information about the image of interest \mathbf{f}_i . In the previous Section, an ultrasound image is reconstructed by applying the optimization problem in (10) to the individual equations in (11). The obtained images $\hat{\mathbf{f}}_i$ for $i \in \{1, 2, \dots, N_{Rx}\}$ were combined to form a high-resolution image as in (12). However, a better and more accurate approach is to utilize the fact that the image of interest $\mathbf{f}_{\text{Object}}$ does not change depending on the receiving element number i . Therefore, the RF-signals \mathbf{p}_i for $i \in \{1, 2, \dots, N_{Rx}\}$ include information about the same object image $\mathbf{f}_{\text{Object}}$. In such a case, we can use a joint image reconstruction scheme to further enhance the reconstruction accuracy and image resolution. As a simple solution to the joint reconstruction problem, we will next discuss a matrix inversion approach. First, we rearrange the measurement signals \mathbf{p}_i and transmission matrices \mathbf{G}_i in (11) as follows:

$$\begin{bmatrix} \mathbf{p}_1 \\ \mathbf{p}_2 \\ \vdots \\ \mathbf{p}_{128} \end{bmatrix} = \begin{bmatrix} \mathbf{G}_1 \\ \mathbf{G}_2 \\ \vdots \\ \mathbf{G}_{128} \end{bmatrix} \begin{bmatrix} \mathbf{f}_{\text{Object}} \end{bmatrix}. \quad (14)$$

For simplicity, let us use a subscript T to denote the tall matrix and tall vector in (14) as follows:

$$\mathbf{p}_T = \mathbf{G}_T \mathbf{f}_{\text{Object}}. \quad (15)$$

Then, a matrix inversion solution to (15) can be written as

$$\mathbf{G}_T' \mathbf{p}_T = \mathbf{G}_T' \mathbf{G}_T \mathbf{f}_{\text{Object}}, \quad (16)$$

where $(\cdot)'$ denotes a transpose. Then, the object image is equal to

$$\mathbf{f}_{\text{Object}} = (\mathbf{G}_T' \mathbf{G}_T)^{-1} \mathbf{G}_T' \mathbf{p}_T. \quad (17)$$

In such a case, we can directly reconstruct a high-resolution image by utilizing information across the elements of the array. Similarly, we can use the optimization problem in (10) to recover the image $\hat{\mathbf{f}}_{\text{Object}}$ as follows:

$$\hat{\mathbf{f}}_{\text{Object}} := \arg \min_{\mathbf{f}} \|\mathbf{f}_{\text{Object}}\|_1 \text{ subject to } \|\mathbf{G}_T \mathbf{f}_{\text{Object}} - \mathbf{p}_T\|_2^2 \leq \varepsilon, \quad (18)$$

where $\|\cdot\|_1$ denotes the L1-norm and $\varepsilon \geq 0$. To successfully reconstruct an object image $\hat{\mathbf{f}}_{\text{Object}}$, the transmission matrix in (18) needs to be incoherent. We achieved incoherency by transmitting an ultrasound wavefront of random interference. We measure the incoherence of the transmission matrix \mathbf{G} using the Gram matrix $\mathbf{D} = \mathbf{G}^* \mathbf{G}$. We assume that each column of the matrix \mathbf{G} is normalized to one. The absolute value of the off-diagonal elements $|d_{i,j}|$ of matrix \mathbf{D} represents a cross-correlation value between the corresponding pair of columns i and j of the matrix \mathbf{G} .

3.3.4. Random Excitation Signals

We propose using excitation signals coded with random sequences to make spatial responses of individual point scatterers to be mutually incoherent. In such a case, the proposed method can reconstruct high-resolution ultrasound images as described in Section 3.3.2. The procedures to generate and upload excitation signals to the research scanner are given in Chapter 4.3. The following steps are used to generate the j -th excitation signal for each element $j \in \{1, 2, \dots, N_{Tx}\}$:

- Generate a binary pseudorandom sequence of length N_w $\mathbf{w}_j = [w_{j,1} \ w_{j,2} \ \dots \ w_{j,N_w}]$

where each element $w_{j,n}$, i.e., $n \in \{1, 2, \dots, N_w\}$, is drawn from the binary set $\{-1, 1\}$ following the uniform distribution.

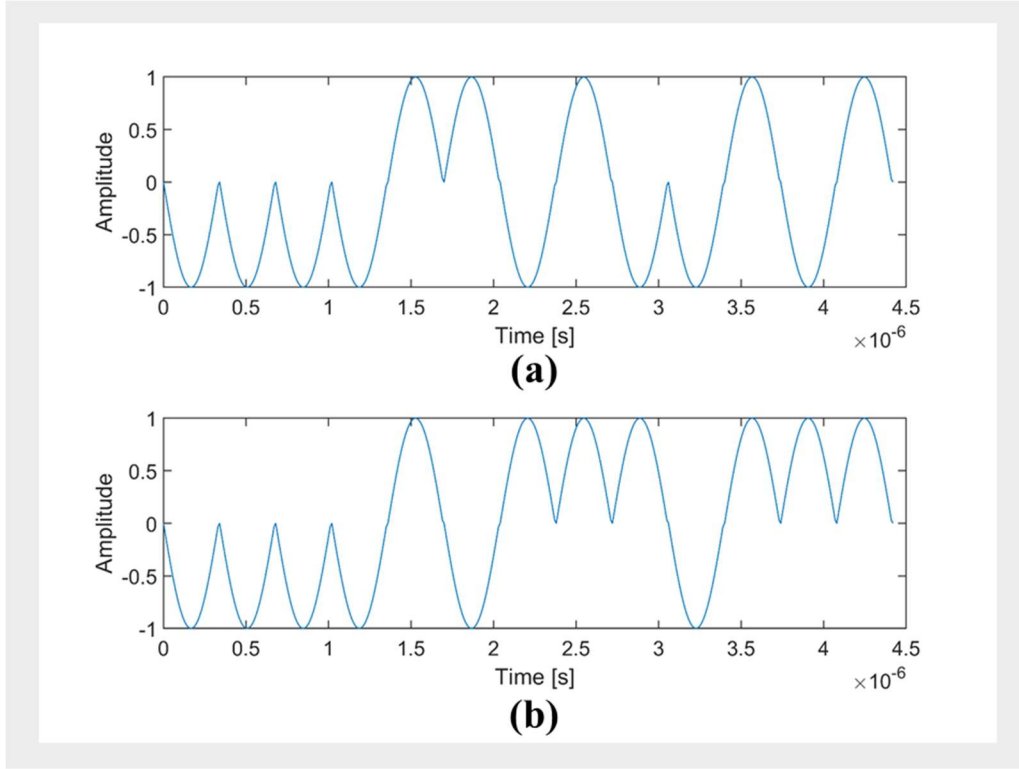


Figure 3.4. Examples of random excitation signals. (a) random excitation signal $w_1(t)$ and (b) random excitation signal $w_2(t)$

- Convolve every element of the sequence \mathbf{w}_j with the base signal of a half-cycle sine wave at the nominal frequency of f_c .
- Repeat steps 1 and 2 for each j -th element in the array.

We can now define the proposed excitation signals $w_j(t)$, coded with random sequences \mathbf{w}_j , in (5) as follows:

$$w_j(t) = \sum_{n=1}^{N_w} w_{j,n} u(t - T(2n-1)/2), \quad (19)$$

where $u(t) := A \cos(2\pi f_c t) \Pi(t/T)$ is the half-cycle base signal; $\Pi(t/T)$ is the rectangular signal which is equal to 1 inside the interval $[-T/2, T/2]$ and 0 otherwise; $2T = 1/f_c$ is

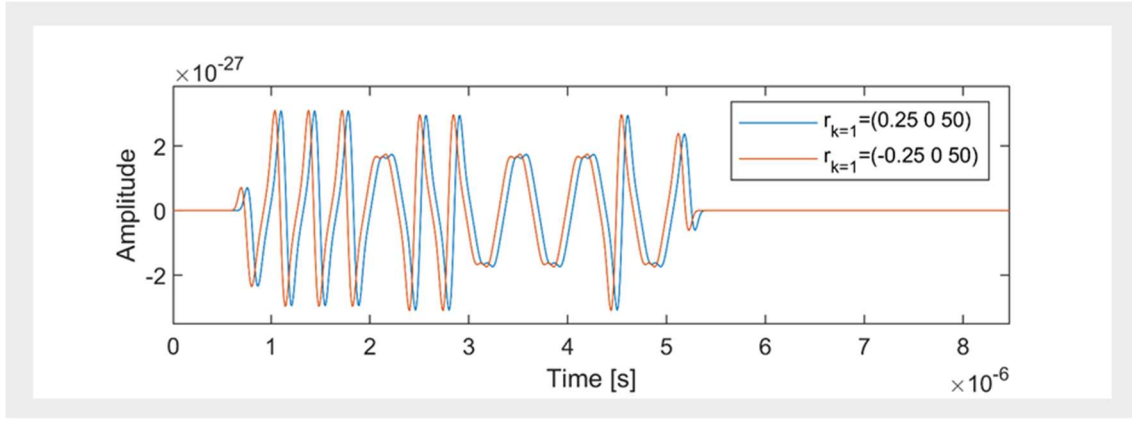


Figure 3.5. Simulated ultrasound signals of two point scatterers with lateral separation of 0.5 mm: when only two array elements transmitted random signals.

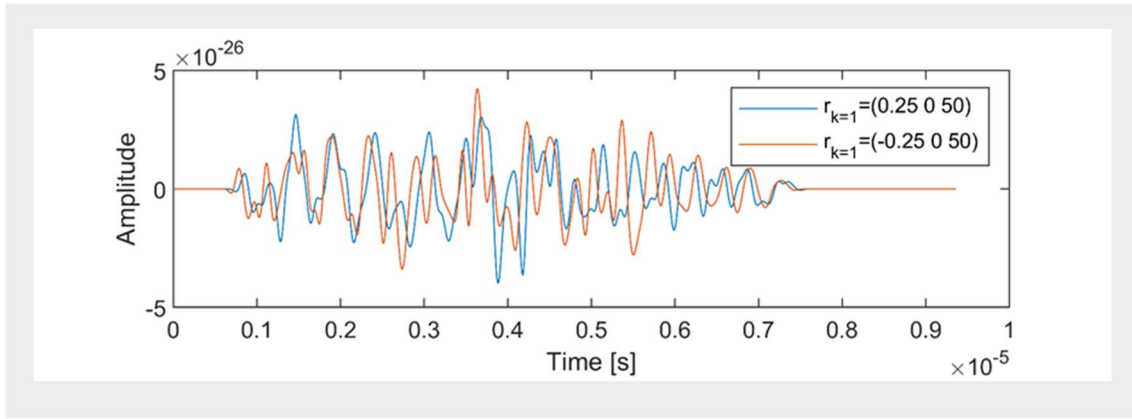


Figure 3.6. Simulated ultrasound signals of point scatterers with lateral separation of 0.5 mm: when all 128 array elements transmitted random signals.

the period of the base signal; A is the amplitude. Ideally, we want excitation signals to be completely random which would make spatial responses even more incoherent; however, a rapid oscillation of excitation signals can potentially be damaging to the piezo-electric crystals. Therefore, we smoothed the sequences \mathbf{w}_j using a sine wave as given in (19). The duration of excitation signals can be controlled by either changing the frequency f_c of the sine wave

or the length N_w of the binary random sequences \mathbf{w}_j . In our study, we produce excitation signals with binary sequences of the length $N_w = 13$ and the nominal frequency $f_c = 3$ MHz. This gives excitation signals with $4.5 \mu\text{s}$ duration. For example, we set the random sequences \mathbf{w}_j for $j = 1, 2$ as

$$\mathbf{w}_1 = (-1, -1, -1, -1, 1, 1, -1, 1, -1, -1, 1, -1, 1) \text{ and}$$

$$\mathbf{w}_2 = (-1, -1, -1, -1, 1, -1, 1, 1, 1, -1, 1, 1, 1);$$

then, the corresponding random excitation signals are shown in Figure 3.4. Let us consider two spatial points described by a vector $\mathbf{r}_k = (x, y, z)$ for $k = 1, 2$ with the coordinates $\mathbf{r}_{k=1} = (0.25, 0, 50)$ mm and $\mathbf{r}_{k=2} = (-0.25, 0, 50)$ mm.

When we transmit random excitation signals $w_j(t)$ from two array elements, the spatial response of the scatterer at $\mathbf{r}_{k=1}$ is shown in blue in Figure 3.5. The spatial response of the scatterer at $\mathbf{r}_{k=2}$ is shown in red in Figure 3.5. The shapes of the spatial responses are a direct result of the constructive and destructive interference that occurs between the transmitted random excitation signals.

By increasing the number of transmitted random signals $w_j(t)$ for $j \in \{1, 2, \dots, N_{Tx}\}$ we can further reduce the correlation between two different adjacent spatial points. With Eq. (13), the coherence μ between any two column vectors \mathbf{g}_k and \mathbf{g}_l can be measured. Similarly, we measure the coherence of a random excitation signal $w_1(t)$ and $w_2(t - \tau)$ a delayed random excitation signal $w_2(t)$, i.e.,

$$\langle w_1(t), w_2(t - \tau) \rangle = \frac{\int_0^{N_w T + \tau} w_1(t) w_2(t - \tau) dt}{\int w_1(t)^2 dt \int w_2(t)^2 dt} \quad (20)$$

where $N_w T$ is the duration of each excitation signal $w_j(t)$, and τ is the difference between the arrival time of the signal $w_1(t)$ and that of $w_2(t)$ at the observation point \mathbf{r}_k . The arrival time-delay τ shall depend upon the difference of total distance the wave has traveled. Thus delay τ depends on the spacing $\|\mathbf{r}_1 - \mathbf{r}_2\|$ between the transducer elements. When the more number of array elements are used to transmit the proposed random signals, the more random the interference pattern becomes, and the more incoherent the spatial responses of the relevant point scatterers become. For example, we let $N_{Tx} = 128$, and use all 128 elements to emit random signals $w_j(t)$ for all $j \in \{1, 2, \dots, N_{Tx}\}$. Then, the spatial response of the scatterer at $\mathbf{r}_{k=1}$ is shown in Figure 3.6. in blue. The spatial response of the scatterer at $\mathbf{r}_{k=2}$ is shown in red. In this particular case, the mutual coherence (13) of the two impulse responses equals 0.04.

3.3.5. Theoretical Resolution

Conventional ultrasound systems that use delay-and-sum beamforming are diffraction-limited. The diffraction resolution limit is $\lambda/2$, [5]. According to [7], the best lateral resolution of conventional ultrasound systems is one wavelength λ of the transmit pulse. For typical frequencies in the range of 3–15 MHz, the lateral resolution corresponds to 0.5 mm to 0.1 mm. The best axial resolution is two wavelengths 2λ [7]. For typical frequencies in the range of 3–15 MHz, the axial resolution corresponds to 1.0 mm to 0.2 mm.

In our approach, the resolution limit is the grid size d , a real-valued scalar. We aim to minimize d while having the maximum correlation μ remain to be small. If the grid size

d is set too small, the coherence μ of a transmission matrix will be high, thus making it difficult to reconstruct the image $\hat{\mathbf{f}}_i$. Given a set of excitation signals $\{w_j(t) : j = 1, 2, \dots, N_{Tx}\}$ and a receiver element $i \in \{1, 2, \dots, N_{Rx}\}$, we can obtain the transmission matrix \mathbf{G}_i and find the smallest distance d subject to sufficiently small mutual coherence μ of \mathbf{G}_i , i.e., $\mu < \delta$. Thus, the resolution limit of the proposed method is closely related to the optimization problem (10). The maximum achievable resolution \hat{d} is then formally given in terms of the mutual coherence (13) of the matrix \mathbf{G}_i as

$$\hat{d} := \min_d \mu(d) \text{ s.t. } \mu < \delta \quad (21)$$

where $\delta > 0$ is a utility parameter of a positive real number. For example, when the distance d between two point scatterers decreases, the value of the coherence μ will naturally increase because the phase shift between the transmitted random signals at two spatial points will become less and less noticeable. The theoretical resolution of the proposed method is not limited by the diffraction, but rather by the coherence of the matrix \mathbf{G}_i . The coherence of the transmission matrix describes the correlation between spatial responses of point scatterers. Therefore, we identify the tradeoffs that exist between the achievable image resolution (the distance d separating the scatterers on the virtual grid) and the coherence of the matrix \mathbf{G}_i .

In Section 3.3.4, we have discussed that a more complex wavefront of random interference can be used to reduce the coherence of a transmission matrix and thus improve image resolution. Likewise, the coherence of the matrix \mathbf{G}_i depends on the nominal frequency and length of pseudorandom sequences. It would be too difficult to obtain the optimal solution based on all possible combinatorial variations of these parameters. We now want to discuss

how we have found the excitation signal set $\{w_j(t) : j = 1, 2, \dots, N_{Tx}\}$ and maximum resolution \hat{d} . To diminish the complexity, we have devised a reduced complexity setting. Under this setting, calculation of the mutual coherence is done only for a reference set of the lateral point scatterers. Over this reference set, the optimization in (21) is performed for a certain selected δ . We refer to this as μ_L the local coherence. There are several reference sets we have tried. We let $\delta = 0.35$ and aim to find the minimum grid size. The optimal reference set is the lateral point scatterers which are separated by 0.25 mm and located at the depth of 50 mm. On this set of lateral points, the proposed set of excitation signals, the proposed nominal frequency, and the length of the pseudorandom sequence has been found. They are the nominal frequency of $f_c = 3$ MHz and the length of the pseudorandom sequence of $N_w = 13$. We further discuss how these parameters are related to each other. We let the speed of sound $c_0 = 1540$ m/sec and the sampling frequency $f_s = 40$ Msamples/sec. The grid size of $d = 0.25$ mm is obtained from μ_L for $\delta = 0.35$. The local mutual coherence is $\mu_L = 0.3$ and the mutual coherence is $\mu = 0.79$. Any excitation signals generated with the same parameters would produce the desired effect of random interference and can be used to reconstruct high-resolution images.

Chapter 4

Research Equipment

In this chapter, we provide a detailed description of the research equipment, a step-by-step guide to control the ultrasound scanner. The content of this Chapter is organized as follows:

- We describe the parameters of our ultrasound research scanner and a linear transducer array.
- We provide a step-by-step guide that shows how to control the scanner using a control panel and a system control script.
- We provide instructions to generate system-control-script, explain which parameters accessible for control, and methods to generate a script.
- We provide an overview of data acquisition procedures, measurement tests, and calibration techniques.

4.1. Research Ultrasound Equipment

In our experimental study, we use a research ultrasound scanner capable of generating the proposed ultrasound wavefront of random interference. The ultrasound research scanner is

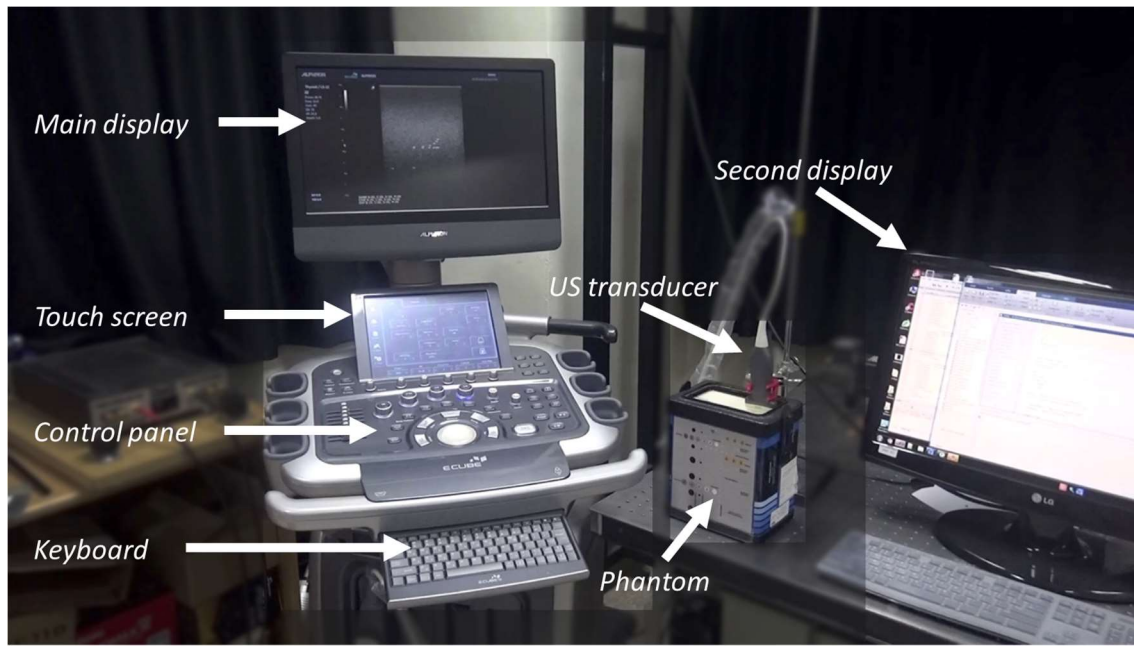


Figure 4.1. Image of the experimental setup.

a COSMOS research unit developed in collaboration with Alpinion Medical Systems. The image of the research scanner is shown in Figure 4.1. The scanner consists of a display, a control panel with a touch screen, an ultrasound probe, front-end electronics, and a computer system that serves as a digital back-end. The control panel provides the ability to view and change system settings. The display shows an US image and scanner's parameters (central frequency, imaging depth, power of US pulse, gain compensation, imaging depth, focusing points, gray-scale bar). The block diagram of the scanner is shown in Figure 4.2. The parameters of the scanner can be controlled using a research interface and a system-control-script (Matlab file). System-control-script contains instructions for each instance of transmission (Tx) and reception (Rx) events. The system-control-script can be generated using a Python script, see Section 4.3. To achieve our research objective, the scanner was equipped with a special module called Arbitrary Wave Generator (AWG). The AWG has a dedicated memory that is used to

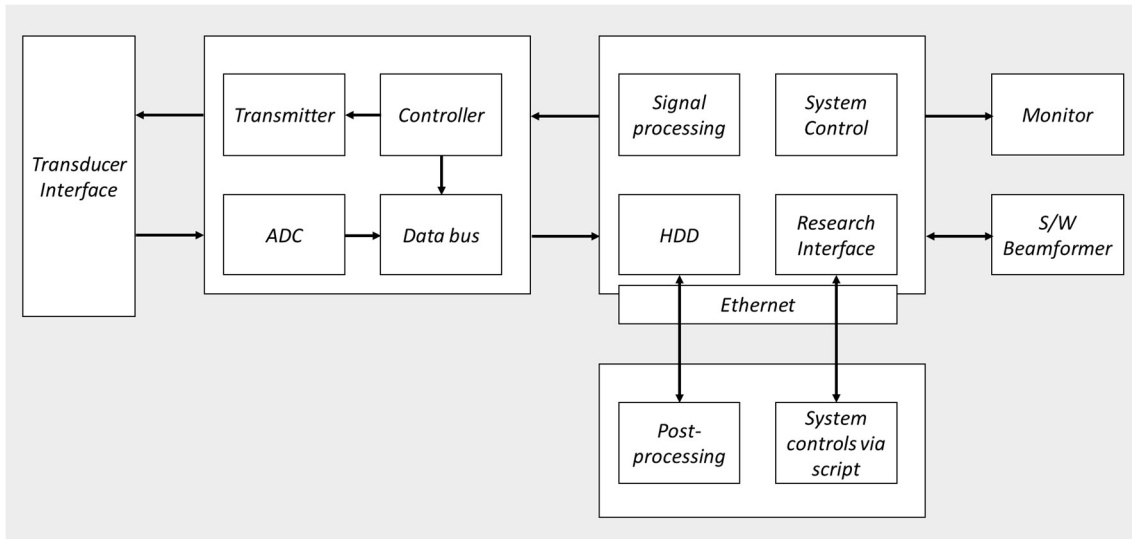


Figure 4.2. Block-diagram of research scanner.

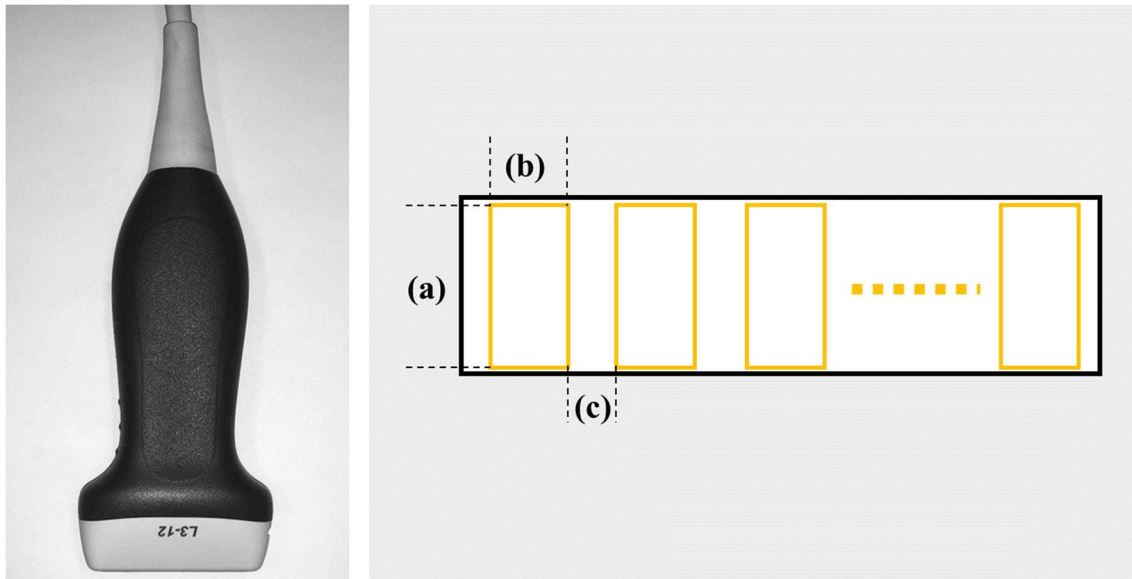


Figure 4.3. Transducer and dimension of the piezoelectric elements; a) height, b) width, and c) separation of elements.

store the proposed random excitation signals. The memory can store an array of size 128×2048 of eight-bit data where each row is assigned to the corresponding transmitting element of the transducer array. We use a linear transducer array that has 128 identical piezo-

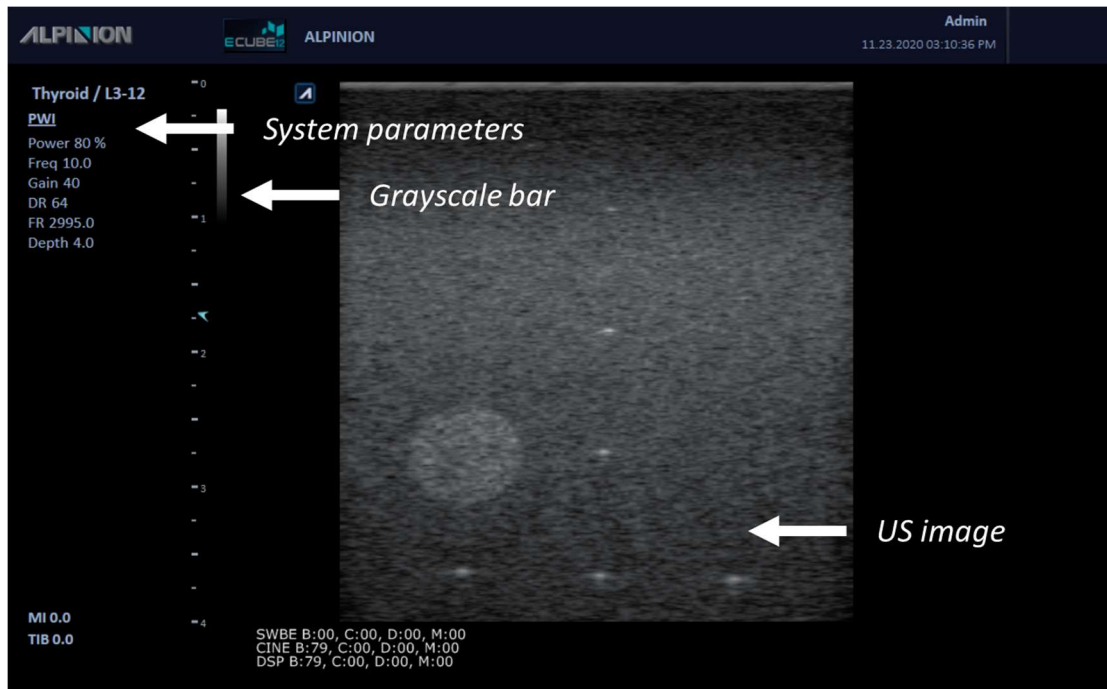


Figure 4.4. User interface – main display.

electric elements. The array elements are 4.5 mm high, 0.3 mm wide, and the elements are evenly separated from each other with a 0.03-mm gap. The image of the transducer array is shown in Figure 4.3.

4.2. Operating Instructions

To start the ultrasound scanner, press the On/Off button in the top-left corner of the control panel. The research scanner by default will boot into be Windows embedded operating system (OS). Once Windows is live, launch the "E-cube 12" ultrasound program from the start menu. After a few seconds, a window of the program and US image will be shown on the main display, see Figure 4.4. The user interface (UI) will be shown on the touch screen, see Figure 4.5. From "2D tab", on the touch screen, we can change ultrasound pulse and other parameters.

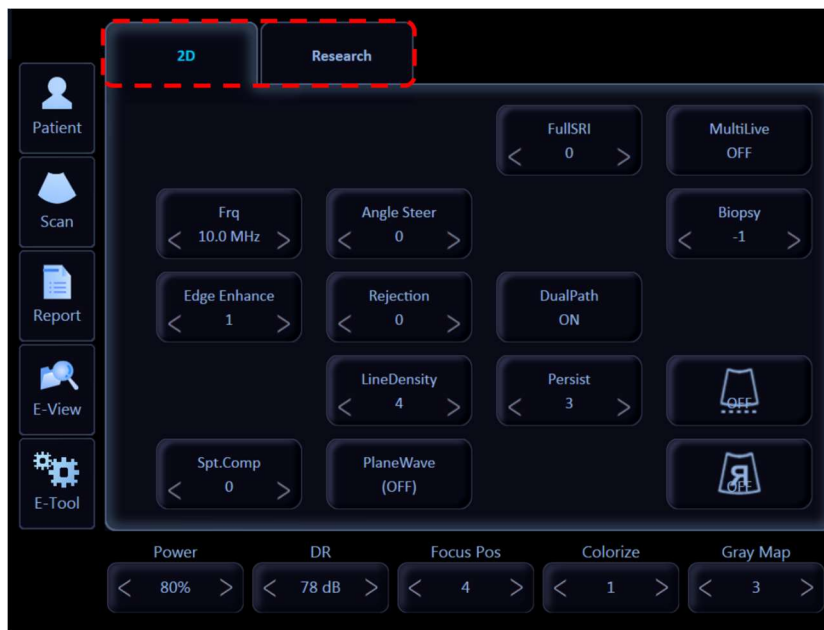


Figure 4.5. 2D imaging controls (UI – touch screen).



Figure 4.6. Research system controls (UI – touch screen).

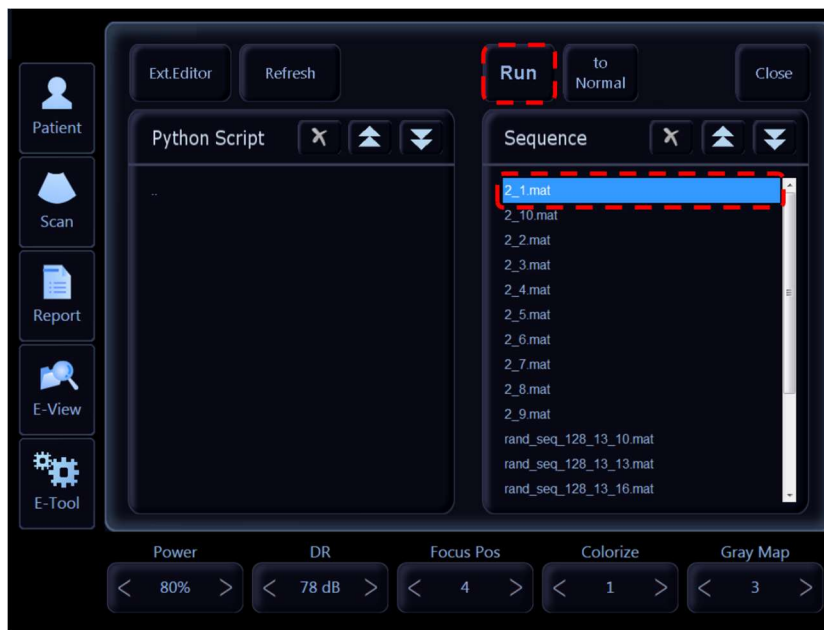


Figure 4.7. Script controls (UI – touch screen).



Figure 4.8. Script controls (UI – touch screen).

From the "Research tab", on the touch screen, we can execute a system control script that contains instructions for each Tx and Rx instances. To launch the scanner in research mode, first, navigate to the "Research tab" and select a preferred type of data to be exported. Then press the "Open Script" button to navigate to the folder containing a script and execute the system-control-script by pressing the "Run" button, see Figure 4.6 and Figure 4.7. After executing the system control script, the main window of the scanner will change to research mode and the scanner will display the image according to the Tx and Rx instruction, see Figure 4.8. The scanner follows instruction in the system-control-script and acquires RF data in a loop cycle. The data is stored in the buffer and overridden with the beginning of a new loop. To stop the acquisition, press the "Freeze" button. Then the RF data from the buffer can be saved by pressing the "Export" button on the touch screen, see Figure 4.6. Next, we explain the structure of the system control script.

4.3. System Control Script

The research ultrasound scanner operates in a loop cycle of transmitting and receiving instances. The cycle loop starts from 0 and continues until value N which depends on the amount of data stored in the buffer. Each instance of the loop cycle is defined in the system-control-script. The main parameters in the system-control-script are a transmit waveform (T_w), a configuration of the transmit array (Tx), and a configuration of the reception array (Rx). In this section, we use *Italic* fonts to refer to code syntax.

An example of a system-control-script is given in Figure 4.9, where, in line 2, we define one transmit waveform T_w by defining a set of excitation sequences using a 128x2048

```

1  # Transmit waveform structure
2  tw_num = 1
3  excitation_seq = np.transpose(f['excitation_signals_c'])*1
4
5  Tw = SysLib.init_object("Tw",tw_num)
6  for i in range(0, tw_num, 1):
7      Tw[i]['waveformType'] = "Waveform"
8      Tw[i]['freqMHz'] = 3.0
9      Tw[i]['burstCount'] = 1
10     Tw[i]['pulseLengthDuty'] = 50
11     Tw[i]['hvNo'] = 0
12     Tw[i]['apod'] = ones(128)
13     Tw[i]['waveA'] = rand_wave
14

```

Figure 4.9. An example of transmit waveform Tw defined in a script.

```

1  # TX structure array
2  tx_num = 129
3  elementCnt = System['Transducer']['elementCnt']
4  spacing = System['Transducer']['spacing']
5
6  Tx = SysLib.init_object("Tx",tx_num)
7  for i in range(0, (tx_num-1), 1):
8      Tx[i]['twNo'] = 0
9      Tx[i]['steerAngleDeg'] = 0
10     Tx[i]['focalPosCm'] = 0
11     Tx[i]['fNum'] = 0.0
12     Tx[i]['apod'] = ones(transNumElement)
13     Tx[i]['delay'] = SysLib.computeTXDelay(Tx[0],System,Parameter[0])
14     Tx[i]['apertureCtrlF'] = 1
15     Tx[i]['aperture'] = ones(128)
16     Tx[i]['aperture'][i] = zeros(1)
17 Tx[128]['twNo'] = 0
18 Tx[128]['steerAngleDeg'] = 0
19 Tx[128]['focalPosCm'] = 0
20 Tx[128]['fNum'] = 0.0
21 Tx[128]['apod'] = ones(transNumElement)
22 Tx[128]['delay'] = SysLib.computeTXDelay(Tx[0],System,Parameter[0])
23 Tx[128]['apertureCtrlF'] = 1
24 Tx[128]['aperture'] = zeros(128)

```

Figure 4.10. An example of transmit instance Tx defined in a script.

array *excitation_seq*. In the conventional ultrasound, a sine chirp is used to excite all the array elements. In the proposed Random Interference method, the rows of *excitation_seq* array are random excitation signals. We discussed methods to generate excitation signals in the next section 3.3.4.

```

1  # Rx controls
2  numFrames = 155
3  acqNum = 2
4
5  Rx = SysLib.init_object("Rx",2)
6  for i in range(0, 2):
7      Rx[i]['acqNum'] = acqNum
8      Rx[i]['tgcNo'] = 0
9      Rx[i]['numFrames'] = numFrames
10     Rx[i]['roiNo'] = 0
11     Rx[i]['originElement'] = 32 + (64*i)
12     Rx[i]['aperture'] = SysLib.computeRXAperture(Rx[i],System['Transducer'])

```

Figure 4.11. An example of receipt Rx instance defined in a script.

```

1  # Specify Rx buffer
2
3  numFrames = 155
4  acqNum = 2
5  index = 0
6
7  RcvBuffer = SysLib.init_object("RcvBuffer", acqNum*numFrames)
8  for i in range(0,numFrames,1):
9      for j in range(0,acqNum,1):
10         RcvBuffer[index]['index'] = index
11         RcvBuffer[index]['acqNo'] = j
12         RcvBuffer[index]['frameNo'] = i
13         index = index + 1
14

```

Figure 4.12. An example of buffer defined in a script.

In Figure 4.10, we define 128 instances of Tx , where $twNo$ in line 8 refers to the wavefront Tw that was defined earlier. The script assigns a set of the same excitation signals to all Tx -instances. In line 15, $Tx[i]['aperture'] = ones(128)$ indicates that all elements in the array are inactive. In line 16, we change the status of i -th element of the array to 0, which indicates that at i -th Tx -instance only i -th element of the array emits i -th excitation sequence from $twNo$ (It is counterintuitive but 0 was assigned to indicate the Turn-On state of the array element by the developers.)

In Figure 4.11, we define 155 frames of data. Each frame consists of 2 acquisition events $acqNum$ and two configurations of Rx arrays. The research systems allow to simultaneously record up to 64 Rx channels. In Figure 4.10, line 11, we define how to organize

```

1  # Sequence structure array
2
3  index = 0 # SeqItem number
4  for i in range(0,numFrames,1):
5      for j in range(0,acqNum,1):
6          if i > tx_num -1:
7              SeqItem[index]['txNo'] = 128
8              SeqItem[index]['rxNo'] = j
9              SeqItem[index]['bufNo'] = acqNum*i+j
10             SeqItem[index]['ctrlNo'] = 0
11             index = index + 1
12         else:
13             SeqItem[index]['txNo'] = i
14             SeqItem[index]['rxNo'] = j
15             SeqItem[index]['bufNo'] = acqNum*i+j
16             SeqItem[index]['ctrlNo'] = 0
17             index = index + 1

```

Figure 4.13. An example of buffer defined in a script.

ultrasound data in the frame. The *originElement* variable is used to determine which half of the array is used during the Rx instance.

In Figure 4.12, we define a buffer to store ultrasound data for each Tx/Rx instance. The code in Figure 4.12, is used to assign buffer index to each combination of *acqNum* and *numFrames*.

In Figure 4.13, we collect *Tw*, *Tx*, *Rx*, and *RcvBuffer* into a sequence structure *SeqItem* which is then stored as a Matlab file. Then, we can upload a Matlab file to the scanner to acquire ultrasound data.

4.4. Data Acquisition and Test Measurements

In previous sections of this Chapter, we discussed how to use and control ultrasound equipment via system-control-script. The system-control-script allows us to design a custom pulse-echo acquisition mode by defining transmit and reception arrays. We now discuss our experimental setup and procedures used to acquire and calibrate research data. The image reconstruction scheme of the proposed interference-based imaging requires *a priori*

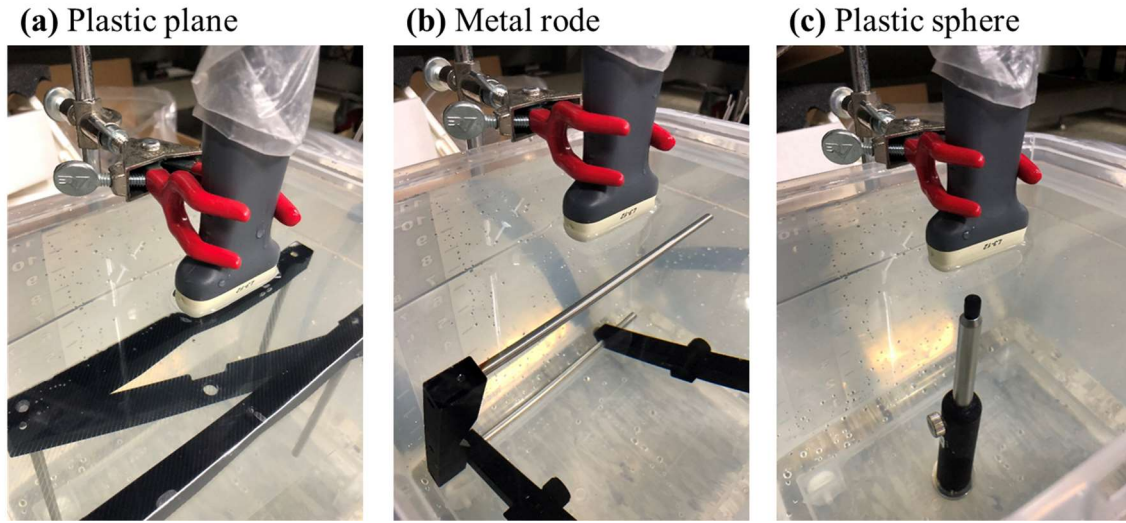


Figure 4.14. Experimental setup three different targets: a plastic plane mounted on metal frame, a metal rode, and a plastic sphere.

information consisting of the spatial impulse responses. In the simulation study, the spatial impulse responses can be easily generated using numerical calculations. However, simulated spatial impulse responses are not suited to reconstruct an image from experimental ultrasound data. Simulated spatial responses do not accurately represent the actual spatial responses in the real experiment. We propose to generate spatial impulse response using measured in the water tank excitation signals. Here, we study how to obtain accurate measurements of the excitation signals and whether these measurements can be used to generate transmission matrices. We recognize that spatial responses can be synthesized as a superposition of excitation signals. In order to maximize the accuracy of such spatial responses, we use measure excitation signals in the water tank. In Figure 4.14, we use a water tank experiment to measure echo signals reflected off a plastic plane, a metal rod, and a small plastic sphere. In Figure 4.15, we use a proposed wavefront of random interference and three targets (a plane, a rode, a sphere) to measure reflected echo signals using the linear transducer. The signals shown in Figure 4.15, are

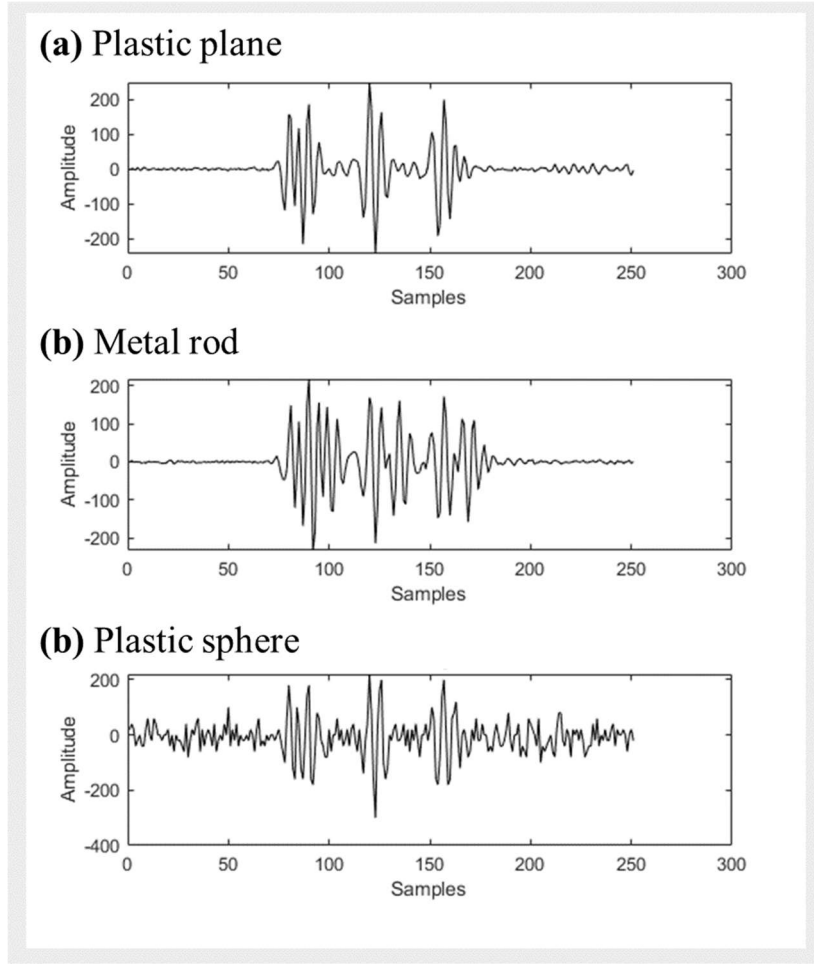


Figure 4.15. Water tank measurements of echo signal reflected off a plastic plane, a metal rod, and a plastic sphere.

correlated more than 85% with each other which allows us to conclude that one of the targets can be used in synthesizing spatial impulse responses for transmission matrices $\mathbf{G}_i \in \mathbb{R}^{M \times N_{sc}}$ (9). We explain procedures used to obtain transmission matrices for experimental setup in Section 5.2.1.

In our experiments, we use a water tank setup shown in Figure 4.16, where a linear transducer is mounted on a clamp stand with a hydrophone pointing towards the surface of the

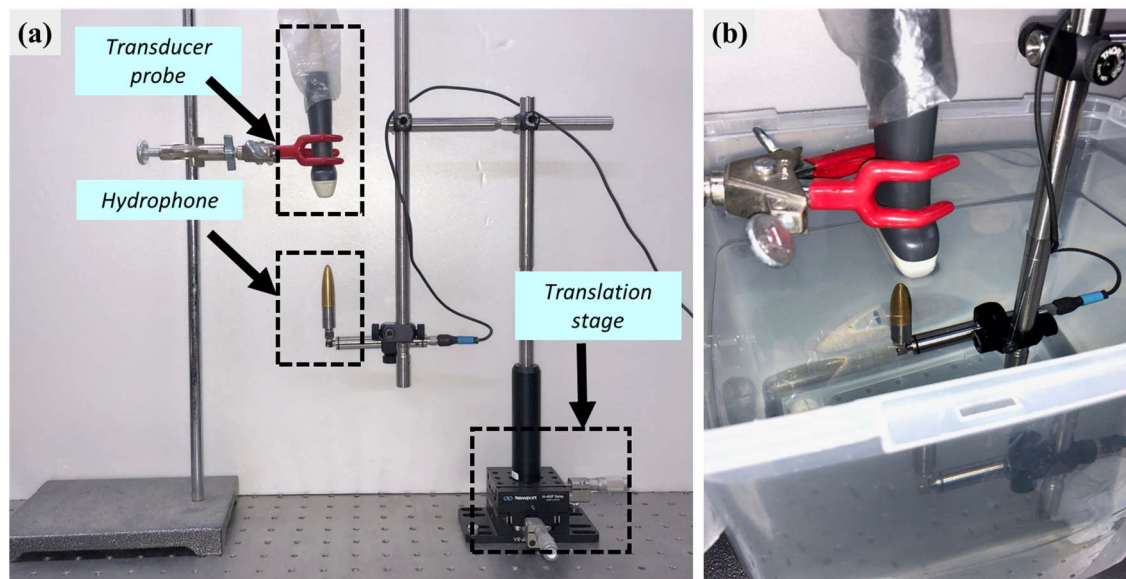


Figure 4.16. Experimental setup with a hydrophone.

transducer. The hydrophone is mounted on a two-dimensional translation stage which allows us to perform manual measurements in the plane parallel to the surface of the transducer. The hydrophone is HGL-series Golden Lipstick Hydrophone developed by Onda Corp. Figure 4.16, shows the transducer and hydrophone submerged into a water tank. We use this setup to measure an ultrasound beam profile of a single array element.

Chapter 5

Simulation and Experimental Results

In this chapter, we present simulation and experimental results; we use several phantoms to verify the proposed method. The proposed method shows much better image resolution when compared to the conventional methods that use delay-and-sum beamforming techniques. In the simulation, we have achieved a 0.25-mm resolution on non-sparse objects. In the experiment, we demonstrate successfully reconstructed images of a tissue-mimicking phantom.

5.1. Simulation Study

The simulation was performed using Field II ultrasound software [36][37][38]. A linear transducer with 128 elements was simulated where each array element was excited with a random signal as described in Section 3.3.4. In the simulation, we defined a transducer array similar to the transducer array that was available for experimental study. The elements of the transducer array were 4.5 mm high and 0.3 mm wide, and they were separated by 0.03-mm gaps. The central frequency and sampling frequency were set to 3 MHz and 40 MHz, respectively. The ROI was set from 35 mm to 55 mm in the axial direction and from -10 mm to

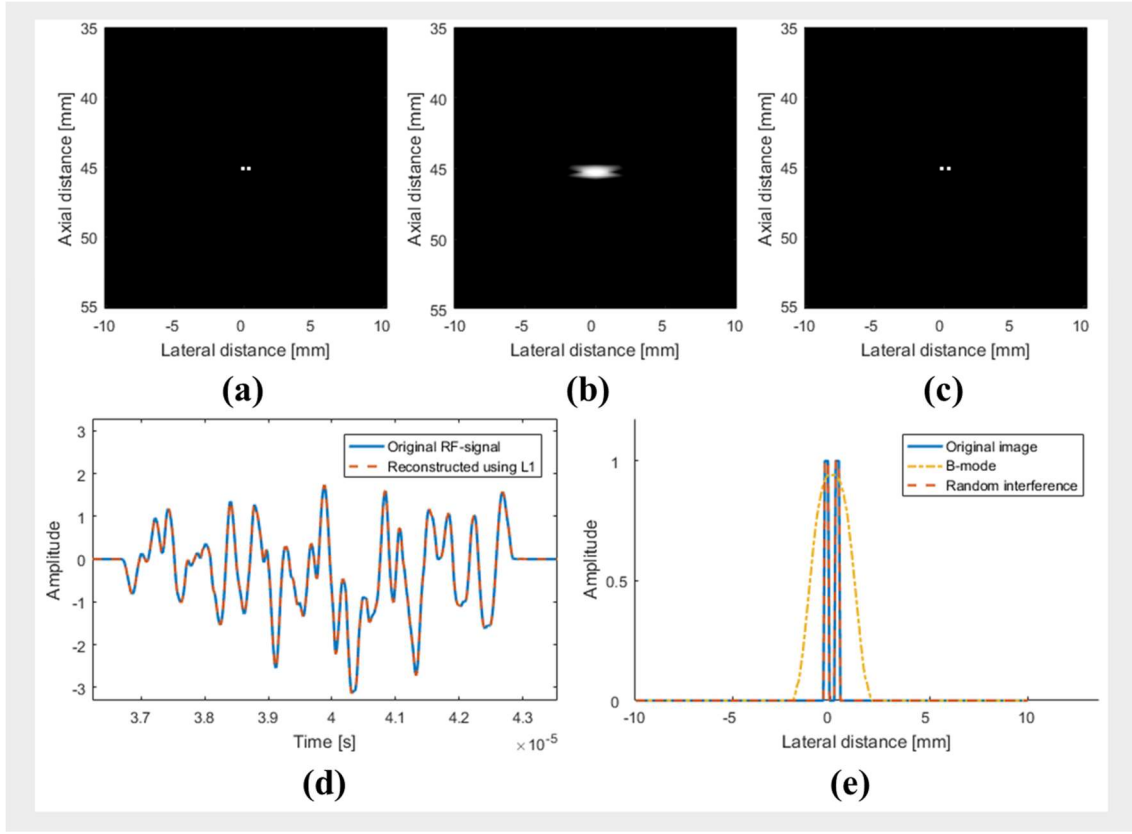


Figure 5.1. Simulation study using a two-point phantom. The phantom features two point targets that are 45 mm from the transducer array with a 0.25-mm separation in the lateral direction between the targets. (a) Image of the scatterer map; (b) image of the focused B-mode method; (c) image of the proposed method. (d) The ultrasound signal acquired at the single receiving channel is plotted in blue; this signal consists of the superposition of impulse responses that correspond to two point targets. The red plot is the reconstructed signal using the interference-based method. (e) Plot of the intensity profiles of the original image, focused B-mode image, and the image obtained using the proposed method. Images are shown with a 60 dB dynamic range.

10 mm in the lateral direction. Synthetic phantoms were defined on a virtual grid with a resolution of $d = 0.25$ mm. This gave us a square image with 81 points in the axial/lateral directions and $N = 6,561$ point scatterers. The speed of sound is again set to $c_0 = 1540$ m/s. The

density of the phantom is set to $D = 1000 \text{ kg} / \text{m}^3$. The acoustic impedance is equal to $Z = 1.54 \times 10^6 \text{ kg} / (\text{m}^2 \cdot \text{s})$. The frequency-dependent attenuation around 3 MHz is 0.5 dB/(MHz · cm). The simulation study was performed using a small ROI due to the extensive time required to generate transmission matrices.

5.1.1. Image Reconstruction – Compound

First, we simulate a synthetic phantom with two closely placed point targets as shown in Figure 5.1. Two-point scatterers are placed at a depth of 45 mm with 0.25-mm separation in the lateral direction. The scatterer map is as shown in Figure 5.1(a). We show a side-by-side comparison of the images obtained using the conventional focused B-mode method and the proposed interference-based method. Figure 5.1(b) shows the image obtained using the focused method. The image was reconstructed using 128 scanlines with the focal point set to 45 mm in the axial direction. With the B-mode method, two-point targets appear with sidelobes and cannot be resolved from each other. However, with the proposed method, we can reconstruct the image of the two points as shown in Figure 5.1(c). The location and intensity of reconstructed scatterers precisely match the scatterer map. Moreover, the radio frequency (RF) signal acquired at a single channel (in blue) and a signal reconstructed using the proposed method (in red) perfectly match as shown in Figure 5.1(d). The RF signal is a superposition of the impulse responses of the two-point scatterers. Therefore, a correct combination of impulse responses, which corresponds to our targets, has been found. In Figure 5.1(e), we plot the intensity profiles taken at the 45-mm position of the scatterer map (blue), its B-mode image (yellow), and the image reconstructed using the proposed method (red). Figure 5.1(e) shows that the proposed

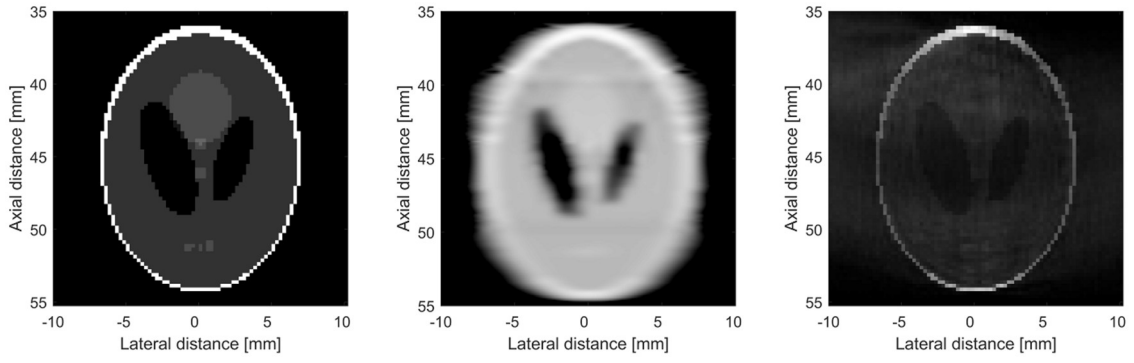


Figure 5.2. Simulation study using the Shepp–Logan phantom. (a) Original phantom image; (b) reconstruction using the focused b-mode method; (c) reconstruction using the interference based method. Images are shown with 60 dB dynamic range.

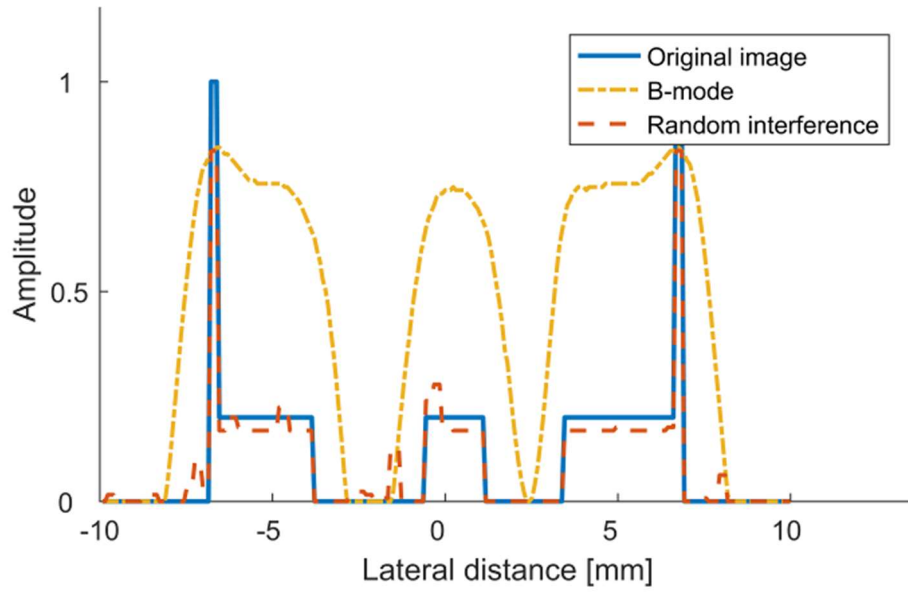


Figure 5.3. Intensity profiles from the Shepp–Logan phantom study. Image intensity profiles are taken at 45 mm in the axial direction. Blue color indicates intensity profile of the original scatterer map. Orange color indicates intensity profile of focused B-mode, and red color indicates intensity profile of interference-based method.

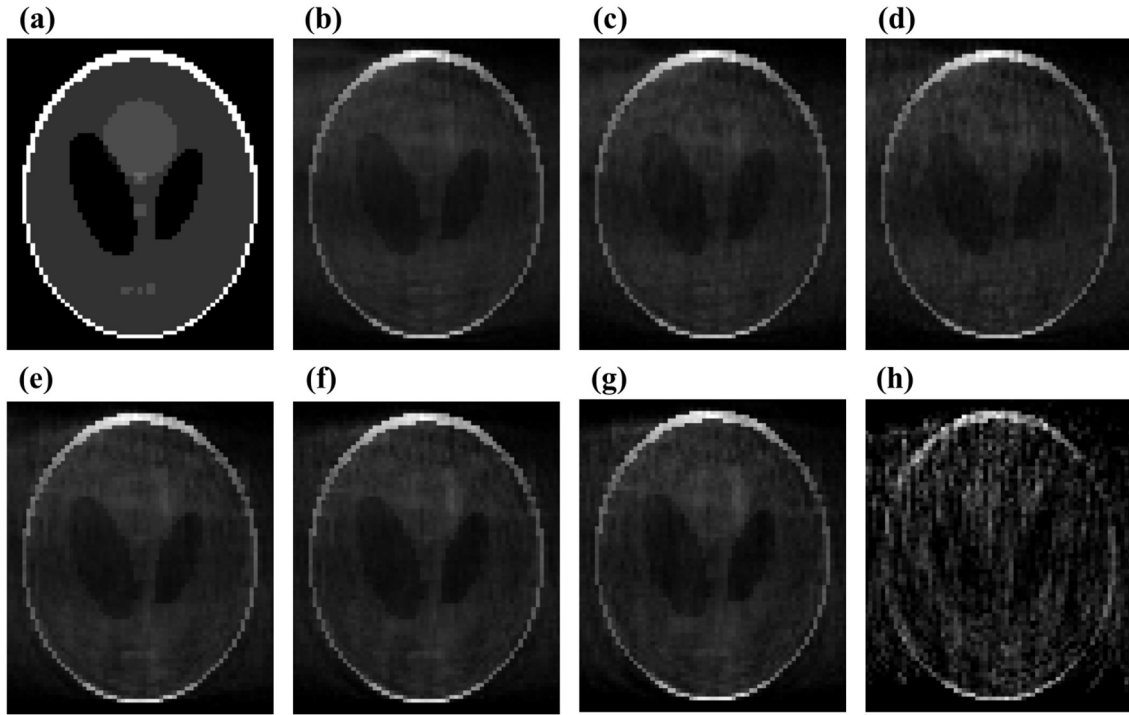


Figure 5.4. Simulation study on dependence of image quality on the number of receiving elements. (a) original image of the Shepp–Logan phantom. (b)-(h) represent corresponding ultrasound images when different numbers of receiving elements are used. The details of different array configurations are given in Table I. Images are shown with 60 dB dynamic range.

method can recover the exact position and amplitude of the point scatterers, whereas the scatterers are not distinguishable in the conventional B-mode method.

In Figure 5.2, a Shepp–Logan phantom is used to evaluate the reconstruction performance of the proposed method on non-sparse objects. The phantom consists of a large number of scatterers of varying intensities, as shown in Figure 5.2(a). The image obtained with the conventional focused B-mode method is shown in Figure 5.2(b). The image is blurred; in particular, the details inside the circle are not visible. In the proposed interference-based method, the image contains accurate details of the phantom structures where the phantom boundaries

and inner circles are clearly identifiable, as shown in Figure 5.2(c). Moreover, the contrast in the image is much closer to that of the original phantom image. The image of the proposed method in Figure 5.2(c) shows that the overall details and contrast are much better than the image obtained using the conventional beamforming based methods.

To demonstrate the proposed method's accuracy, we plotted the intensity profiles of the Shepp–Logan phantom at 45-mm depth, as shown in Figure 5.3. The intensity profiles for the scatterer map, the focused B-mode method, and the interference-based method are shown in blue, yellow, and red, respectively. In Figure 5.3, we can observe that the focused B-mode fails to provide details for the phantom's boundaries. Due to the sidelobes, the intensity profile of the scatterers inside the phantom does not match that of the scatterer map. In Figure 5.3, the proposed method can reconstruct the phantom image with high accuracy. The image of the proposed method in Figure 5.2 shows that the overall details and contrast are much better than the image obtained using the conventional beamforming based methods.

Using a single transmission of the proposed wavefront of random interference, we can reconstruct up to 128 images $\hat{\mathbf{f}}_i$, one for each receiving element $i \in \{1, 2, \dots, N_{Rx}\}$. To achieve high spatial resolution, we compound together all 128 images $\hat{\mathbf{f}}_i$ as given in (12). In addition to the resolution improvements, we are interested in evaluating the dependency of the image quality given a different number of compounding images. The results are shown in Figure 5.4. We consider seven different configurations for the receiving array; Table I summarizes the details of proposed array configurations including information about the total number of active elements in the receiving array, mean squared error (MSE), peak signal-to-noise ratio (PSNR), and signal-to-noise ratio (SNR). The results of MSE, PSNR, and SNR are given with respect to the original Shepp–Logan phantom shown in Figure 5.4(a). For example, the image shown

Table 1.1 Dependency of Image Quality On The Number of Array Elements

	Name	Total number of elements	MSE	PSNR [dB]	SNR [dB]
(a)	Original phantom image	~	~	~	~
(b)	All elements of the array	128	0.0158	17.99	5.60
(c)	Every 3rd element	43	0.0162	17.90	5.51
(d)	Every 5th element	26	0.0164	17.86	5.47
(e)	Elements in the interval [30,98]	69	0.0120	19.21	6.81
(f)	Elements in the interval [40,88]	49	0.0119	19.23	6.84
(g)	Every 2nd element in the interval [50,78]	15	0.0122	19.20	6.80
(h)	Single element [64]	1	0.0255	15.93	3.54

in Figure 5.4(b) was compounded using 128 images. The image provides clear details of the synthetic phantom. The image shown in Figure 5.4(g) was reconstructed using only 15 receiving array elements. Table I shows that MSE becomes smaller when a subset of elements in the middle of the array is used. According to the MSE, we conclude that fewer receiving elements are sufficient to achieve image resolution similar to Figure 5.4(b). This phenomenon can be explained by the acceptance angle of the array elements. The effect of random interference depends on the number of interfering waves. Thus, the random interference is stronger in

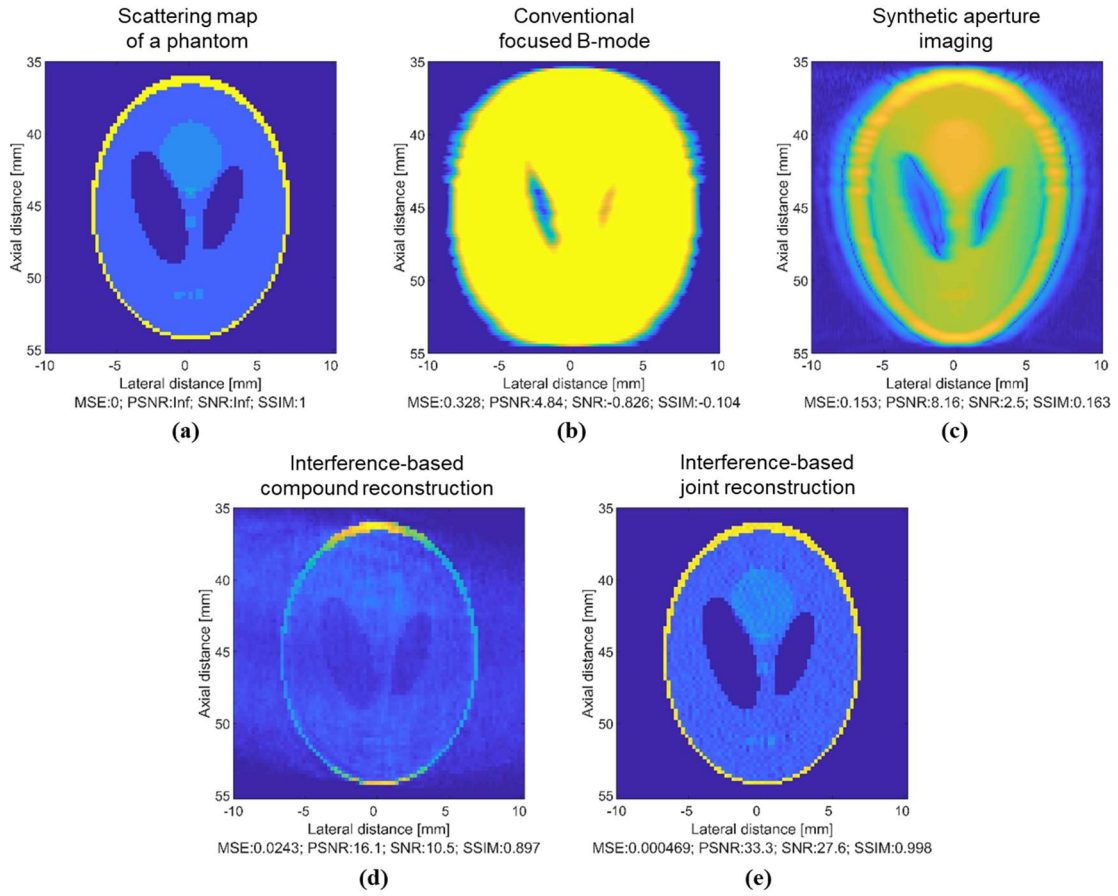


Figure 5.5. Simulation results: (a) scattering map of a Shepp–Logan phantom; (b) an image reconstructed using conventional focused B-mode; (c) an image reconstructed using synthetic aperture beamforming; (d) an image reconstructed using previously proposed interference-based compound reconstruction method; and (e) an image reconstructed using the proposed interference-based joint image reconstruction method.

the center of the ROI. As a result, we observe fewer errors when reconstructing images using RF-data from elements in the middle of the array. Similarly, the PSNR and SNR improves as we increased the number of reconstructed images used to obtain a compound image (12), see Table I. Besides, we would like to emphasize that in the simulation study, the proposed method can reconstruct a 2D image from a single receiving element, the image is shown in Figure

5.4(h). The image is corrupted by noise artifacts; however, strong reflecting points such as the boundaries of the phantom have been reconstructed correctly.

5.1.2. Image Reconstruction – Joint

In Figure 3, we provide a side-by-side comparison of different reconstruction methods. The scattering map of the phantom is shown in Figure 5.5(a). In Figure 5.5(b), we show an image reconstructed using a conventional focused B-mode method. The image was reconstructed using 128 scanlines. The focal point was set to 45 mm depth. The image of the phantom appears with large sidelobes and the details of the phantom cannot be properly reconstructed. In Figure, 3(c) we show an image reconstructed using synthetic aperture imaging provided in the “Beamformation toolbox” [46]. The image was simulated using 65 emissions and beam-formed with 180 lines. In Figure 5.5(d), we show an image reconstructed using the interference-based compound method proposed in [23]. The reconstructed image features a more accurate location and intensity of the scatterers that precisely matches the original scatterer map of the phantom image. However, in the case of the compound method, the image in Figure 5.5(d) is corrupted by noise from the compounding operation. The presence of noise affects the visibility of small elements of the phantom at a lateral distance of 0 mm. In Figure 5.5(e) we show an image reconstructed using the proposed joint image reconstruction scheme. The proposed joint reconstruction scheme allows us to successfully reconstruct a high-resolution image of the phantom. Figure 5.5(e) shows an image obtained using the proposed joint image reconstruction scheme. The image in Figure 5.5(e) has accurate spatial and contrast resolutions. The noise specific to the image in Figure 5.5(d) was eliminated, and the small details of the phantom at a lateral distance of 0 mm are accurately reconstructed. The image

Table 1.2 Mean-squared error (MSE), peak signal-to-noise ratio (PSNR), signal-to-noise ratio (SNR), and structural similarity index (SSIM) values for conventional and proposed imaging methods.

	Method	MSE	PSNR	SNR	SSIM
1.	Conventional focused B-mode	0.328	4.84	-0.826	-0.104
2.	Synthetic aperture beamforming	0.153	8.16	2.5	0.163
3.	Interference-based Compound method	0.0243	16.0	10.5	0.897
4.	Interference-based Joint reconstruction	0.000469	33.3	27.6	0.998

reconstructed using the newly proposed method exhibits less speckle noise and a more accurate representation of small components of Shepp–Logan phantom. We compare the results from the Shepp–Logan phantom study in Table 1.2. The proposed interference-based joint reconstruction method, among all methods, has a lower MSE, higher PSNR and SNR, and extremely high value for SSIM.

5.2. Experimental Study

In the previous sections, we described the details of our simulation study. In this section, we analyze the obtained results. To verify our proposed method, we developed a research ultrasound system capable of generating the proposed ultrasound wavefront of random interference. The ultrasound system is a COSMOS research unit developed in collaboration

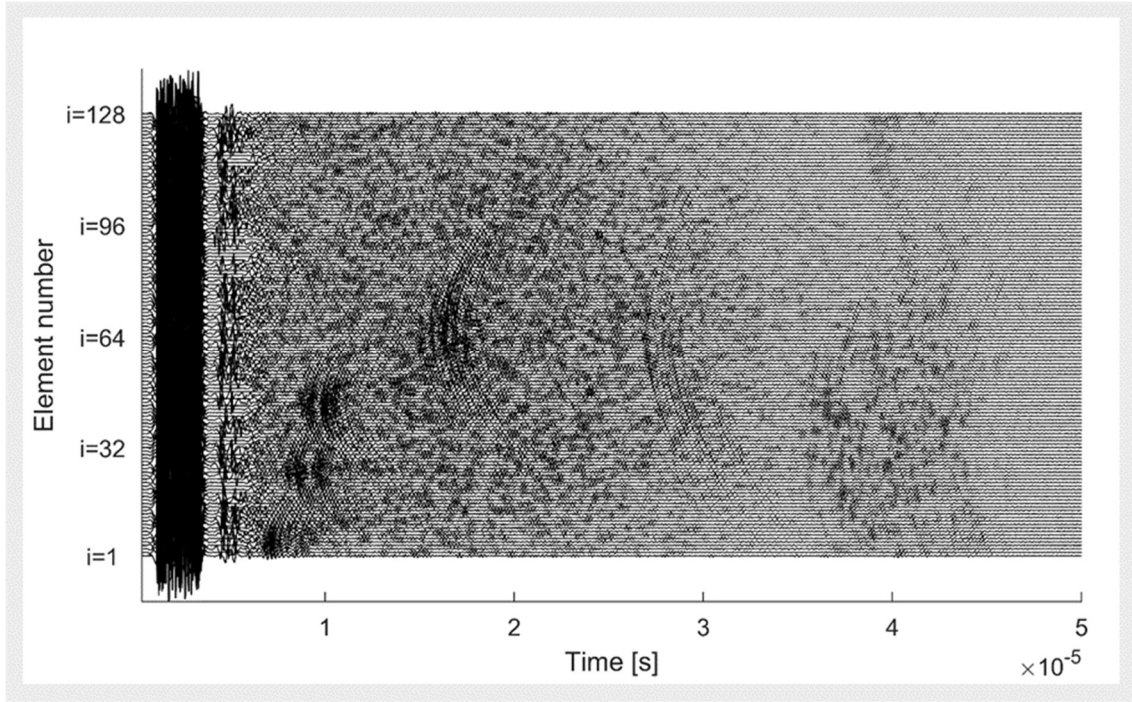


Figure 5.6. Raw RF data acquired during a real phantom experiment. Each line corresponds to a single RF signal acquired using one of the 128 array elements when all of the array's elements were simultaneously excited with the proposed random excitation signals.

with Alpinion medical systems. The system features a linear transducer array with 128 piezoelectric elements and a central frequency of 3–12 MHz. The array elements are 4.5 mm high and 0.3 mm wide, and the elements are evenly separated from each other with a 0.03-mm gap. The sampling frequency is set to 40 MHz and the frequency of the transmitted ultrasound wave is 3 MHz. All parameters in the experimental study were set to reproduce our simulation protocol. The system is equipped with an arbitrary wave generator (AWG) to enable the transmission of random signals. The AWG has a dedicated memory that is used to store random excitation signals for every transmitting channel. The memory can store an array of size 128×2048 of eight-bit data where each row is assigned to the corresponding transmitting element of the transducer array.

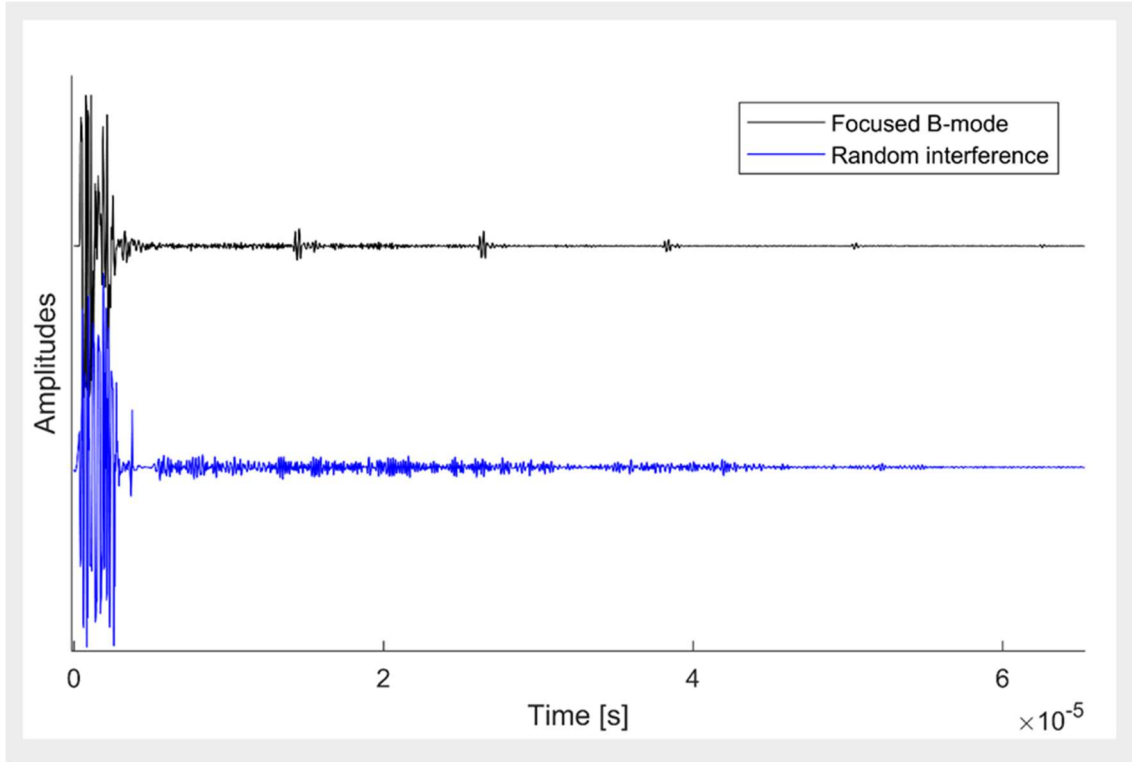
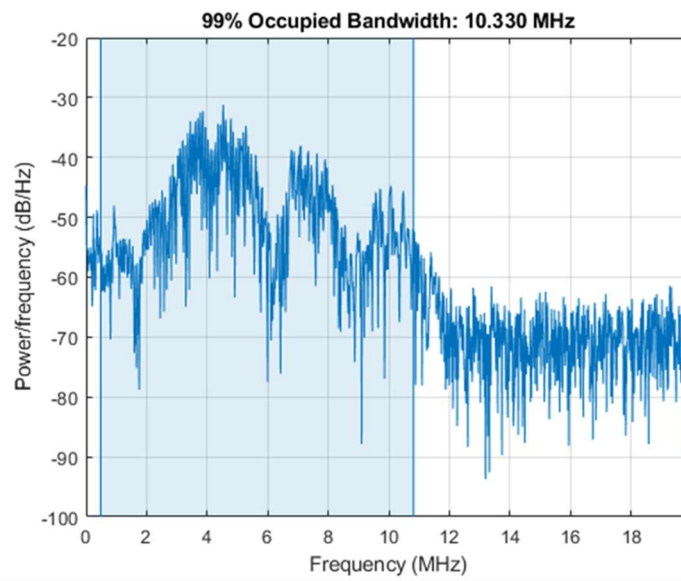
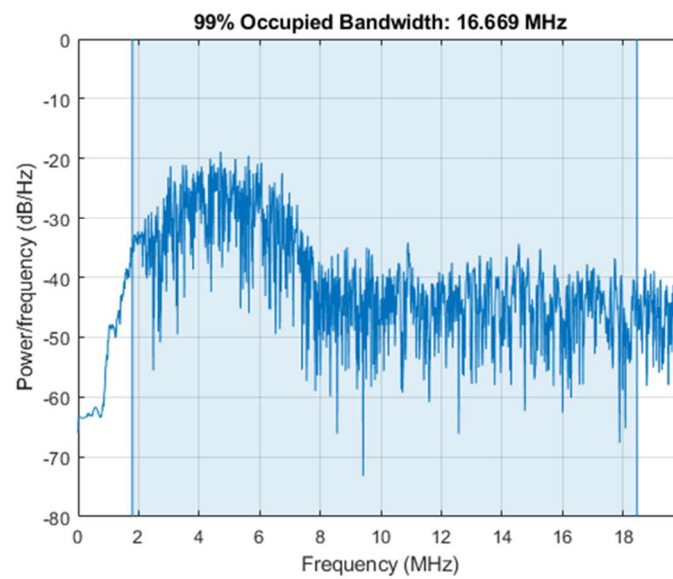


Figure 5.7. Raw RF data acquired during a real phantom experiment. Comparison of the RF signals acquired using 64-th element of the array. The RF signal acquired using the conventional focused B-mode method is plotted in black; the sampled RF signal features strong reflections from nylon wires at 1, 2, 3 and 4 cm depths, respectively. The RF signal acquired at the 64-th element of the array using the proposed interference-based method is plotted in blue; the sampled RF signal features strong echo reflections across all time samples.

In this experiment, we use a commercially available phantom CIRS Model 040GSE. The phantom is made of a solid elastic hydrogel that mimics the properties of human tissue. To demonstrate differences between the conventional beamforming-based method and the



(a)



(b)

Figure 5.8. Analysis of the bandwidth of echo signals. a) bandwidth of echo signal acquired using conventional focused B-mode, b) bandwidth of echo signal acquired using random interference method.

proposed interference-based method, we first provide a side-by-side comparison of RF-data. The transducer array was aligned such that the 64-th element of the array was perpendicular to the vertical distance group consisting of nylon wires. All elements of the transducer array are simultaneously excited with the proposed random excitation signals which yield an incident wavefront of random interference. In Figure 5.7, we provided a side-by-side comparison of echo signals acquired at 64-th array element using the conventional beamforming-based method and the proposed interference-based method. Figure 5.7 shows the fundamental differences between the two methods. The echo signal acquired using a beamforming-based method is shown in black in Figure 5.7. The signal features strong echoes reflected from the nylon wires at corresponding depths of 1, 2, 3, and 4 cm respectively. The echo signal acquired using the proposed interference-based method is shown in blue in Figure 5.7. Due to the use of the unfocused transmission of random excitation signals, the signal shown in blue in Figure 5.7 features multiple reflections from different spatial directions. Note that in the case of the proposed method, the strength of the echo signals is comparable to the level of the strength of echo signals in the conventional beamforming-based method. The transducer array was aligned such that the 64-th element of the array was perpendicular to the vertical distance group consisting of nylon wires. All elements of the transducer array are simultaneously excited with the proposed random excitation signals which yield an incident wavefront of random interference. The full set of array signals acquired during a single transmission of random excitation signals is shown in Figure 5.6.

In Figure 5.8, we analyze the bandwidth of the RF signals previously shown in Figure 5.7. In Figure 5.8(a), we show the bandwidth of echo signal acquired during transmission of conventional focused pulse, the energy of the signal occupied 10.3 MHz bandwidth. In Figure

5.8(b), we show the bandwidth of the echo signal acquired during transmission of the wavefront of random interference, the energy of the signal occupied 16.6 MHz bandwidth. The difference in the bandwidth is noticeable and explained by the fact that the echo signal in the proposed random interference method is a mixture of echoes reflected from all directions. In this case, we believe that signal with higher bandwidth carries more information about the object.

5.2.1. Transmission Matrices – Experimental Study

In this section, we provide a description of procedures to generate transmission matrices \mathbf{G}_i used in the real phantom experiments. The direct method of obtaining spatial responses for the experimental study would be using a hydrophone with a translation stage. However, it is a time-consuming and error-prone method because a hydrophone has to be perfectly aligned with a large number of different spatial points. Therefore, we propose an alternative method of obtaining spatial responses. We first measure the echo signals of the random excitation signals reflected from a plastic plane in a simple water tank experiment setup. Then, we generate approximations of spatial responses as the sum of delayed versions of measured random signals. Next, we describe a step-by-step procedure used to obtain transmission matrices \mathbf{G}_i 's for $i \in \{1, 2, \dots, N_{Rx}\}$.

First, the linear transducer array was aligned perpendicular to the plastic plane, which was placed at 4-cm depth in a water tank. We assigned random excitation signals (19) to all array elements. Next, in a series of pulse-echo transmissions, we activated one by one each transmitting element and measured the ultrasound wavefront reflected from the plastic plane. We used the same transducer array to record the reflection of the plastic plane echo signals. Let \mathbf{A} be an $M \times N_{Tx} \times N_{Rx}$ three-dimensional real-valued matrix where M is the total number

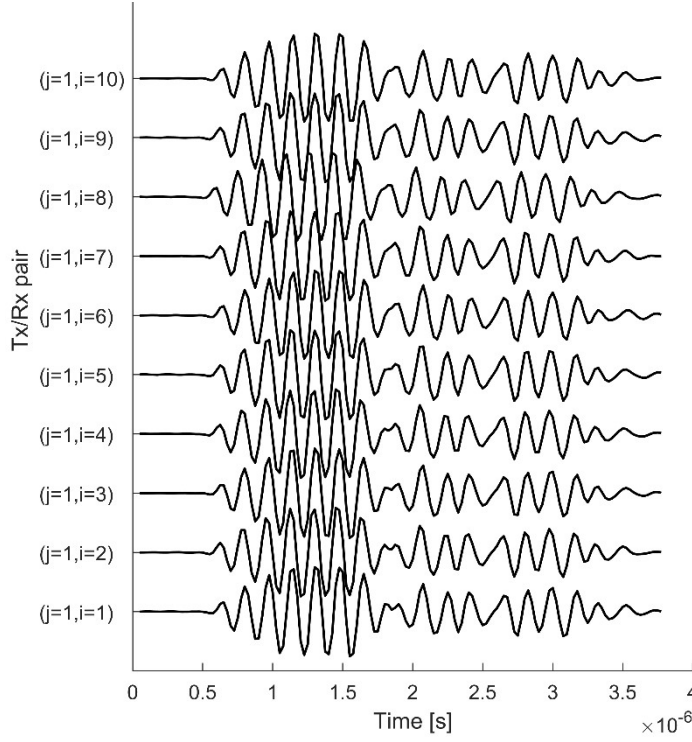


Figure 5.9. Echo signals of the proposed excitation signals measured in the water tank experiment for the corresponding pair of transducer elements (j,i) . Only the first $j = 1$ transmitting element were activated; all N_{Rx} receiving elements were used to receive the echo signals

of signal samples, N_{Tx} is the number of transmitting elements, and N_{Rx} is the number of receiving elements. $\mathbf{A}[s,j,i]$ denotes the (s,j,i) component of an array \mathbf{A} for each $s \in \{1,2,\dots,M\}$, $j \in \{1,2,\dots,N_{Tx}\}$, and $i \in \{1,2,\dots,N_{Rx}\}$. Fixing one variable, i.e., $\mathbf{A}[M, j=1, N_{Rx}]$ notation, is to means a two-dimensional matrix of the matrix \mathbf{A} .

In Figure 5.9, we show the echo signals acquired when only $j = 1$ element emitted a random signal $w_1(t)$. The echo signals were normalized and aligned by applying time-delays. We arranged the measured echo signals into a three-dimensional matrix \mathbf{A} . Then,

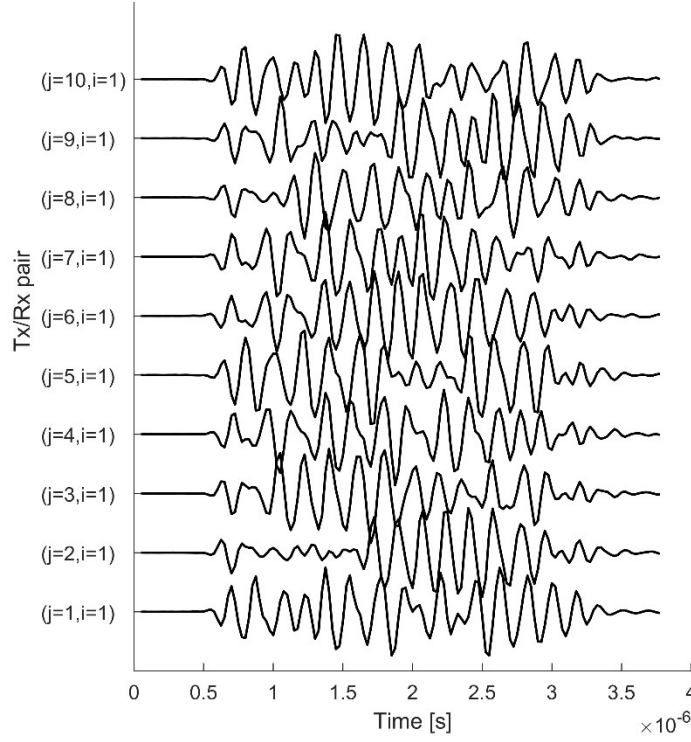


Figure 5.10. Echo signals of the proposed excitation signals measured in the water tank experiment for the corresponding pair of transducer elements (j,i) . Each transmitting element j was assigned with a unique random excitation signal. The transmitting elements were activated one by one. The receiving element $i = 1$ is used to record echo signals.

$\mathbf{A}[M, j = 1, N_{Rx}]$ corresponds to a two-dimensional matrix $M \times N_{Rx}$ with each column representing an echo signal as shown in Figure 5.9. These echo signals exhibited a very small variation and that the shape of the reflected echo signals was identical. We measured echo signals individually for every pair of transmitting and receiving elements. The echo signals of the matrix $\mathbf{A}[M, j = 1, N_{Rx}]$ are shown in Figure 5.9. Similarly, $\mathbf{A}[M, j = 2, N_{Rx}]$ would represent echo signals acquired using all $N_{Rx} = 128$ receiving elements when only the second $j = 2$ element transmits the random excitation signal $w_2(t)$. Likewise, Figure 5.10. shows the

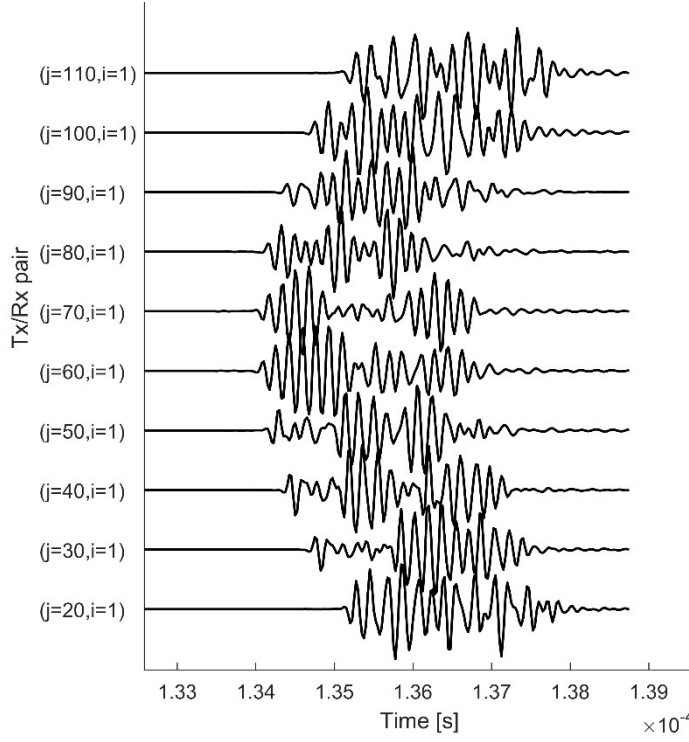


Figure 5.11. The delayed echo signals of the proposed excitation signals measured in the water tank experiment for the corresponding pair of transducer elements (j,i) and the spatial point at \mathbf{r}_k .

matrix $\mathbf{A}[M, N_{Tx}, i = 1]$ that corresponds to the echo signals acquired using the receiving element $i = 1$ when all $j \in \{1, 2, \dots, N_{Tx}\}$ elements individually transmit a corresponding random signal $w_j(t)$.

Let \mathbf{B} be an $N_{Tx} \times N_{Sc}$ two-dimensional real-valued matrix. $\mathbf{B}[j, k]$ denotes the (j, k) component of \mathbf{B} for each $j \in \{1, 2, \dots, N_{Tx}\}$ and $k \in \{1, 2, \dots, N_{Sc}\}$. Next, we define ROI as a two-dimensional virtual grid, shown in Figure 3.3. We use $\|\mathbf{r}_j - \mathbf{r}_k\|$ to find the distance information from every array element to every spatial point on the virtual grid. We arrange distance information into the matrix \mathbf{B} . Using the matrix \mathbf{B} , we can calculate the time

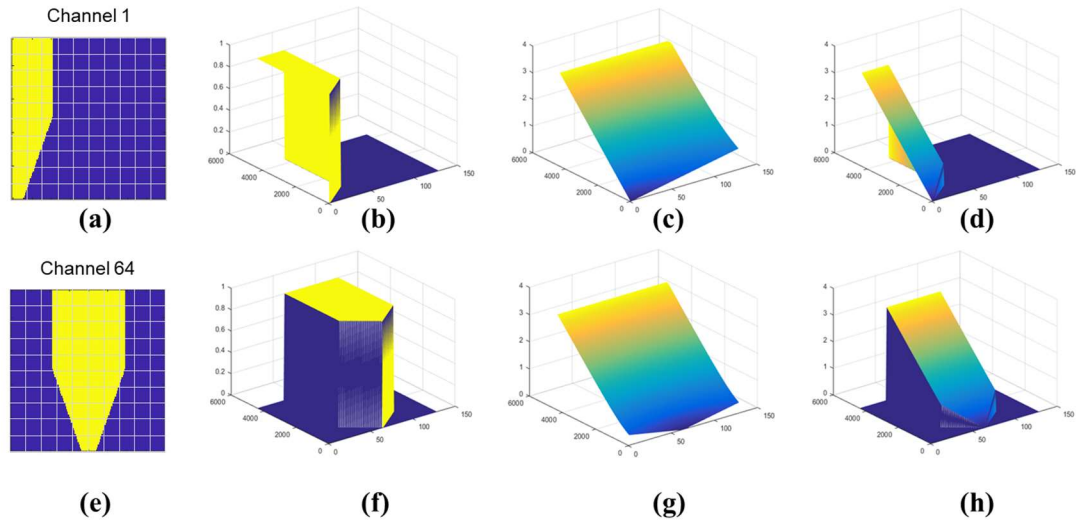


Figure 5.12. Illustration of how a subset of spatial points is selected using acceptance angle of the array element.

required for a transmitted random signal to travel to the spatial point and return to the receiving element. Then, we can find the spatial impulse response of the spatial point at \mathbf{r}_k by applying the corresponding time-delay from the matrix \mathbf{B} to the measured echo signals in the matrix \mathbf{A} ; the delayed echo signals of corresponding random excitation signals are shown in Figure 5.11. Then, the spatial impulse response \mathbf{g}_k is found by summing and normalizing the delayed versions of measured random excitation signals. We repeat this procedure for every spatial point k in the ROI. We use the procedure described above to generate the matrix \mathbf{G}_i for our real phantom experiment.

The elements of the transducer array have acceptance angles, and not all spatial points contribute to the echo signal received by the i -th transducer element. Therefore, in (9), we

use a submatrix of \mathbf{G}_i and subset of \mathbf{f}_i that represents only point scatterers within the acceptance angle of the receiving element. For example, in Figure 5.12, we show the acceptance angles for channels 1 and 64.

In summary, we share different approaches used to generate transmission matrices for our experimental study. In the beginning, we have attempted to reconstruct an image of the real phantom using transmission matrices from the simulation study. However, the limited bandwidth of the transducer means that simulated spatial responses do not accurately represent the actual spatial responses in the real experiment [54]. Thus, the resulting reconstructed images have suffered from low resolution. Also, we considered using a wire and a point target instead of a plastic plane. However, it was difficult to measure the responses of the excitation signals throughout the whole experiment. Since the target object is small, it reflected a weak noisy signal. To obtain consistent measurements, besides, a smaller target has to be much more precisely aligned with the transmitting array element. A high precision alignment was difficult to be achieved in our experimental setup because transducer elements are separated by a very small distance of 0.03-mm and embedded in a closed housing.

5.2.2. Experimental Results – Compound

The sampling frequency is set to 40 MHz and the frequency of the transmitted ultrasound wave is 3 MHz. All parameters in the experimental study were set to reproduce our simulation protocol, Section 5.1.

In this experiment, we use a commercially available phantom CIRS Model 040GSE. To demonstrate that the proposed interference-based method improves spatial resolution, we have selected two regions of the phantom. The ROI spans 55 mm in the axial direction and 40

mm in the lateral direction. The resolution of the virtual grid was $d = 0.25$ mm. This gave us an image with $N_{sc} = 38,801$ point scatterers. In the simulation study, the images are reconstructed using RF-data from one pulse-echo transmission of random signals. In the experimental study, the images are reconstructed using RF-data acquired using ten pulse-echo transmissions due to strong acoustic noise and attenuation. In each pulse-echo transmission, we use a different set of randomly generated signals. In total, we reconstruct and compound together 1280 images. On a standard computer with Intel Core i7-6800K CPU and NVIDIA GTX 1060 GPU using a single thread, one image is reconstructed in approximately 4 seconds. The final compounded image is reconstructed in approximately two hours. The RF-data was pre-processed using direct current (DC) cancelation and time gain compensation (TGC).

The first region includes vertical/horizontal groups. The images of the first region are shown in Figure 5.13. The ROI includes eight 0.1-mm-diameter nylon wires and a cyst. The nylon wires were separated by 10-mm gaps, with the first wire located at 10 mm depth from the transducer. In Figure 5.13 (a), we show an image reconstructed using the conventional focused B-mode method with 128 scanlines. In Figure 5.13 (b), we show an image reconstructed using the proposed interference-based method. The nylon wires in the case of the proposed method can be clearly observed without sidelobes. Besides, the level of speckle-noise is significantly reduced in the proposed method. The image region with cyst target was also accurately reconstructed. The proposed interference-based method is a clear improvement over the conventional B-mode method.

The second region includes axial/lateral resolution groups; see Figure 5.14. The group includes twelve 0.08-mm-diameter nylon wires. The wires are separated by 4, 3, 2, 1, 0.5, and 0.25 mm in the axial and lateral directions. The image obtained using the conventional focused

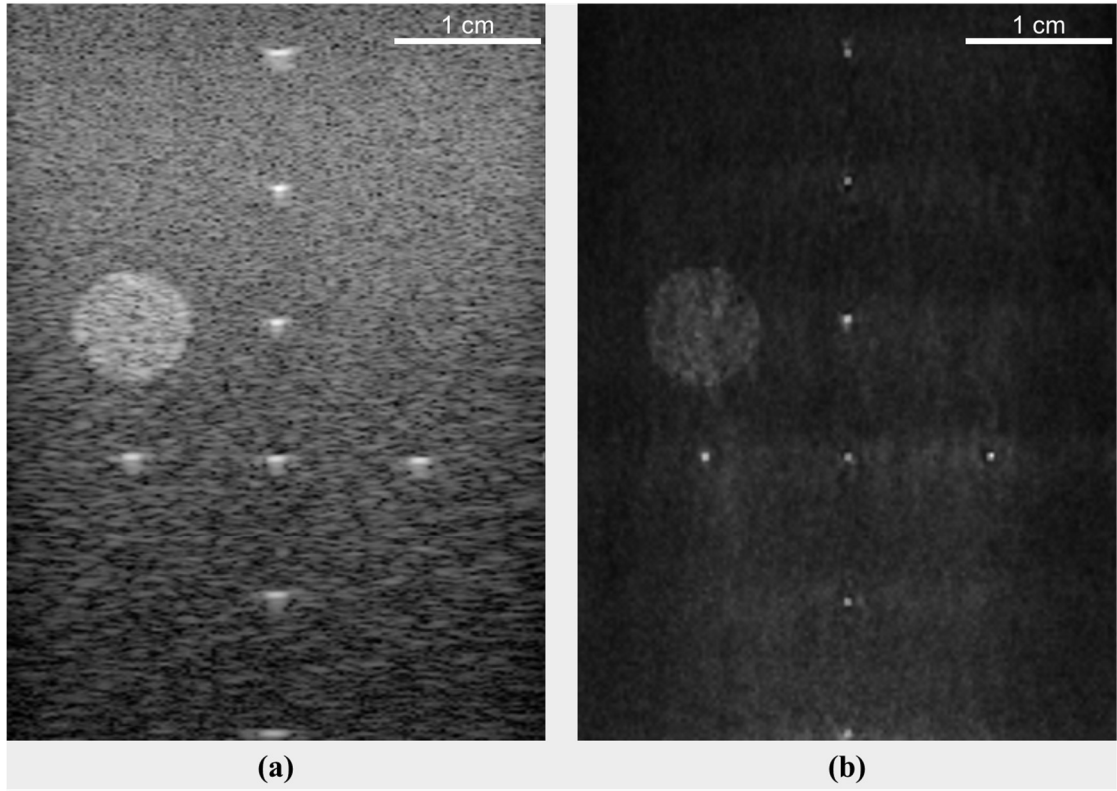


Figure 5.13. Experimental results using a vertical/horizontal target groups of the tissue mimicking phantom. A side-by-side comparison of the region with vertical/horizontal groups (a) the image reconstructed using the conventional focused B-mode (delay-and-sum-beam-forming) method; (b) an image reconstructed using the proposed interference-based method. Images are shown with 60 dB dynamic range.

B-mode method with 128 scanlines is shown in Figure 5.14 (a). The ultrasound image reconstructed using the proposed interference-based method is shown in Figure 5.14 (b). A two time magnified images of axial/lateral resolution groups are shown in Figure 5.14 (c–d). Figure 5.14 shows that the proposed method provides much better details of nylon wires compared to the conventional method.

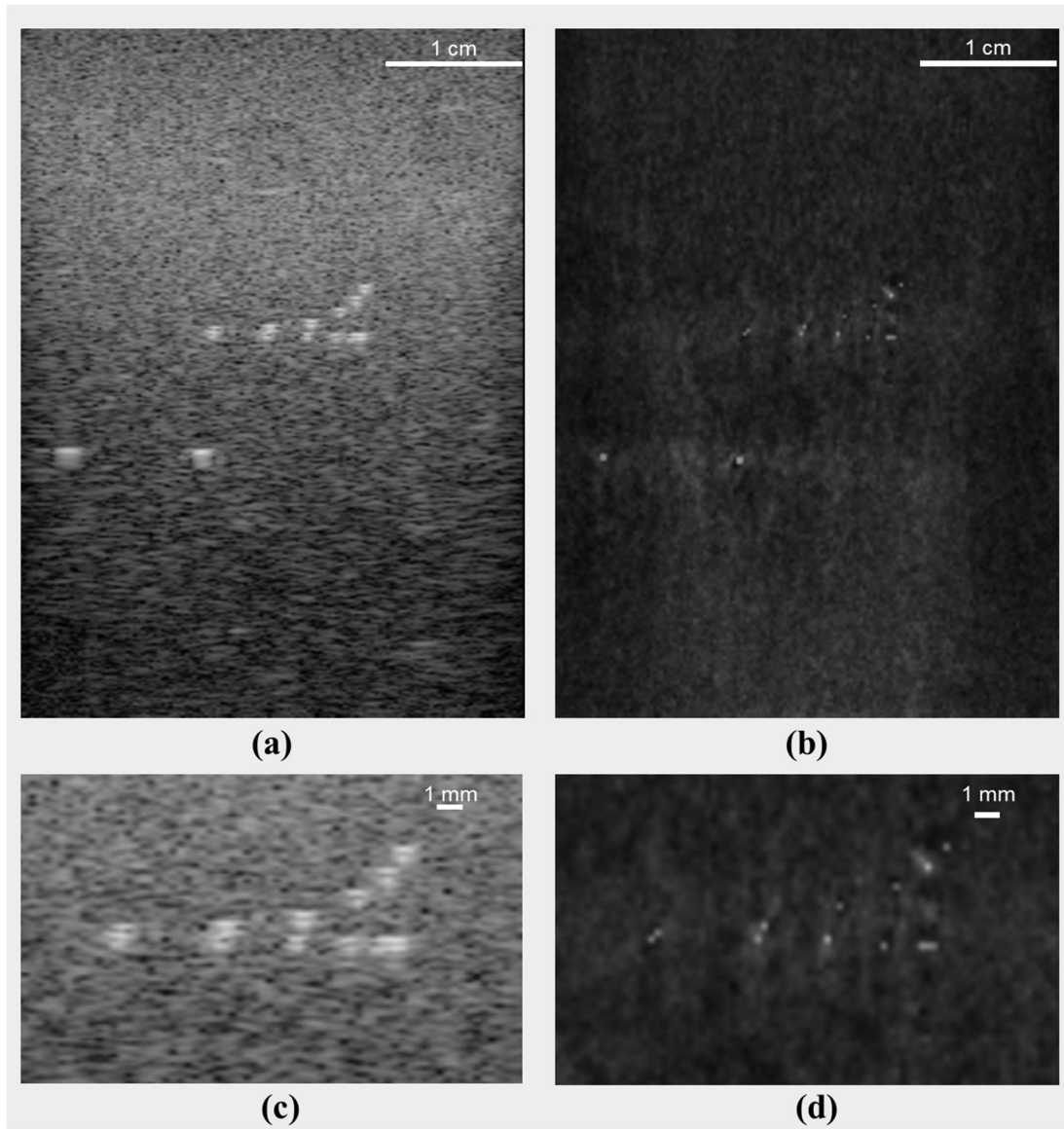


Figure 5.14. Experimental results using a high-resolution target groups of the tissue mimicking phantom. (a) the image reconstructed using the conventional focused B-mode method (delay-and-sum-beamforming); (b) an image reconstructed using the proposed interference-based method. (c)–(d) a two time magnified images of the conventional and the proposed methods. All images are shown with 60 dB dynamic range.

In the proposed interference-based method, the ultrasound images are reconstructed using *a priori* measurements of incoherent spatial impulse responses. We demonstrated the

successful reconstruction of high-resolution ultrasound images, both in simulation and experimental studies. In the simulation study, the proposed method can achieve a resolution of 0.25 mm, which represents a four-fold improvement over conventional beamforming-based methods. In the experimental study, the proposed method can reconstruct ultrasound images of 0.08-mm-diameter nylon wires. Thus, we have demonstrated that the proposed interference-based method can improve spatial and contrast resolutions.

In this section, we compare the results of the proposed method with a few recently published papers. Conventional ultrasound methods require multiple transmissions of the focused ultrasound pulse. For example, a focused B-mode imaging scheme based on delay-and-sum beamforming requires approximately 120 pulse-echo transmissions to reconstruct a single 2D image. Each pulse-echo transmission uses up to 128 receiving channels to acquire the RF signals. This results in a large amount of data being processed in real-time. Therefore, the authors in [30] proposed a sub-Nyquist sampling scheme based on CS to reduce the amount of data required to reconstruct an ultrasound image. They achieved an eight-fold reduction in the sampling rate by integrating the beamforming process directly with the low-rate sampling process. Likewise, a CS theory was applied to STA imaging in [39] to increase the system's frame rate by reducing the total number of required pulse-echo firings. STA imaging requires 128 firings, one for each element in the transducer array. During the reception, all array elements are used to acquire the reflected ultrasound signals. The full STA dataset consists of 16,384 RF signals. The authors in [39] proposed a CS-STA algorithm that could reduce the number of firings from 128 to 32 by combining multiple firings where only 4,096 RF signals were acquired. The CS scheme was used to reconstruct the full STA dataset with the given 4,096 RF signals. This method achieved four-fold data reduction at the cost required to solve 16,384 CS

problems. High-frame-rate STA imaging can be achieved if all CS problems are solved in real-time. Unlike conventional methods that use delay-and-sum beamforming [30][39], the proposed interference-based ultrasound does not use any beamforming techniques. Instead, we can directly reconstruct the final ultrasound image's pixel values by finding the correct combination of impulse responses that are present in the measurement signal. Moreover, the 2D image can be reconstructed using only ten pulse-echo firings. A CS framework derived from the ultrasound propagation theory was described in [40], where a complete ultrasound image can be reconstructed from the transmission of only a single plane wave. This is by far the most relevant work to our proposed interference-based ultrasound method. However, it was reported that the method in [40] could only be used to reconstruct images of sparse objects in the water tank (that consist of few point scatterers) owing to the high coherence in the transmission matrix. In our work, we describe the use of random interference that solves the issue of high coherence in the transmission matrix. Our results show that the proposed method can be used with a tissue-mimicking phantom. Compressed 3D ultrasound imaging using a single transducer element that features a coded aperture mask was recently proposed in [48]. The acoustic mask is placed in front of the transducer and used to disturb the outgoing ultrasound pulse. Ultrasound signals are acquired at 72 different positions when the coded mask rotates around its axes. The transmission matrix is designed by measuring the spatial impulse responses using a hydrophone and translation stage. The experimental study demonstrates a 3D ultrasound image of two letters placed in a water tank. The authors in [48] achieved a very simple imaging modality by replacing the multi-element arrays with a single element transducer. Such an imaging setup can be used to create a portable ultrasound system. However, in our study, we intentionally used an array of transducers to generate random interference because arrays are essential in many other

applications such as Doppler imaging, contrast-agent imaging, and high-intensity focused ultrasound ablation. Besides, generating random interference utilizing measured in the water tank random excitation signals provides greater flexibility for achieving different interference patterns. Furthermore, the mechanical rotation of a physical acoustic lens requires extra time, but the random interference in the proposed method can be changed quickly by using different excitation signals. The authors in [43] proposed a super-resolution ultrasound imaging technique that utilizes *a priori* measurements of the focused ultrasound pulse in water. Then, the image is reconstructed by finding the best spectral candidate. The results in [43] are impressive which have shown practical applications in transmission-mode imaging such as ultrasound microscopy. Our method is, on the contrary, reflection-mode imaging and hence is more practical for noninvasive diagnostic applications such as traditional B-mode imaging.

5.2.3. Experimental Results – Joint

In Figure 5.15, we compare images of dental floss submerged into a water tank and reconstructed using different methods. In Figure 5.15(a), we show an image reconstructed using a conventional focused B-mode method that can be found in all modern ultrasound systems. In Figure 5.15(b), we show an image reconstructed using plane-wave imaging with 30 plane wave transmissions. In Figure 5.15(c), we show an image reconstructed using synthetic aperture imaging. In Figure 5.15(d), we show an image reconstructed using the proposed interference-based joint reconstruction method. The images in Figure 5.15(a–c) appear with sidelobes caused by strong reflections of ultrasound waves that corrupt image scanline during beamforming operation. Meantime, the proposed method is capable to reconstruct a more accurate image

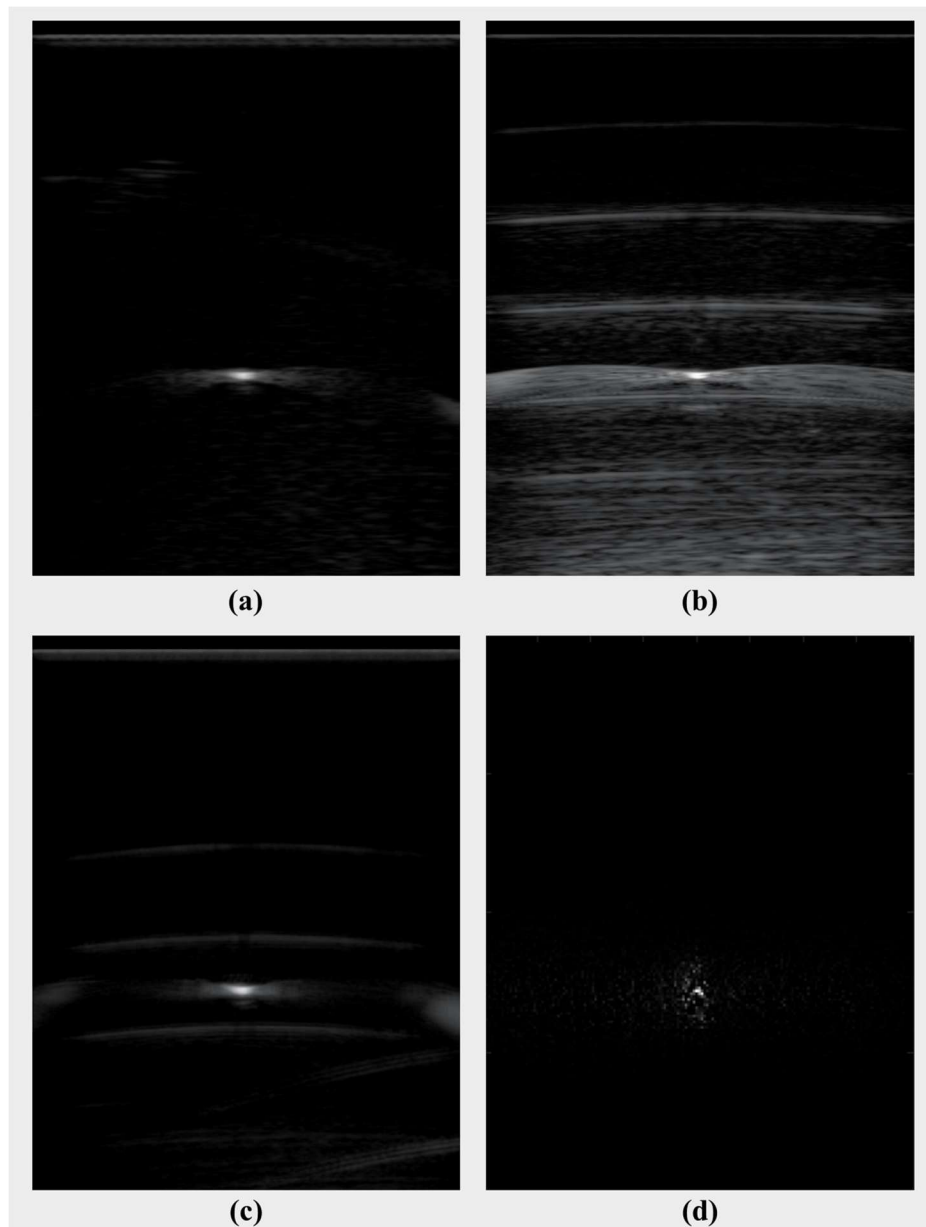


Figure 5.15. Experimental results. Images of a dental floss in the water tank: a) conventional B-mode, b) plane-wave mode, c) synthetic aperture, d) joint image reconstruction method using random interference

of a wire without side lobes. The image in Figure 5.15(d), was reconstructed using data from a single pulse-echo transmission of random interference wave.

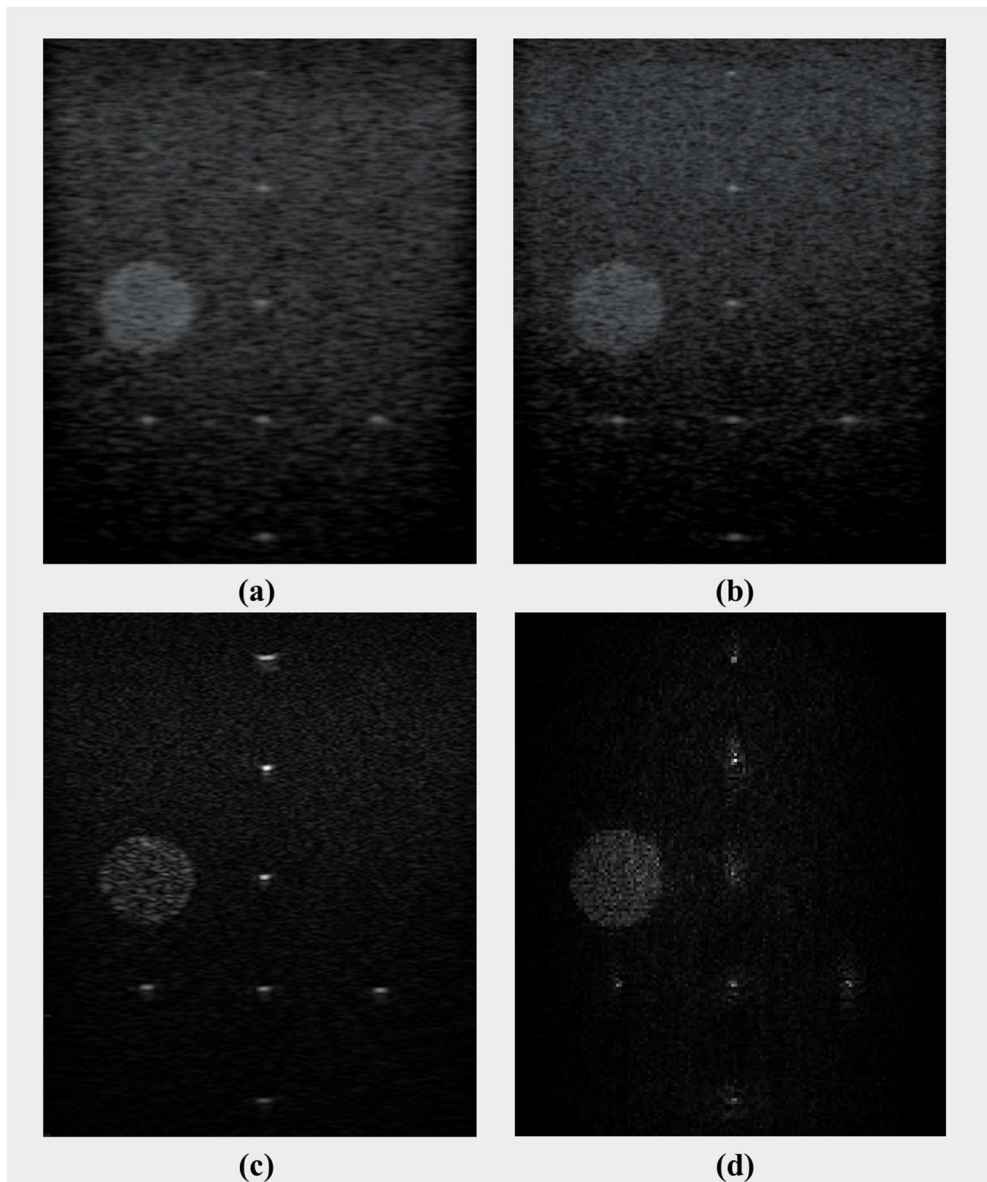


Figure 5.16. Experimental results using tissue mimicking phantom. The ROI includes seven 0.1-mm-diameter nylon wires and a cyst. a) conventional B-mode, b) plane-wave mode, c) synthetic aperture, d) joint image reconstructions method using random interference

In Figure 5.16, we compare images of a tissue-mimicking phantom reconstructed using different methods. The ROI includes vertical/horizontal groups with eight 0.1-mm-diameter nylon wires and a cyst. The nylon wires were separated by 10-mm gaps, with the first wire

located at 10 mm depth from the transducer. In Figure 5.16(a), we show an image of a tissue-mimicking phantom reconstructed using a conventional focused B-mode method. In Figure 5.16(b), we show an image reconstructed using plane-wave imaging. In Figure 5.16(c), we show an image reconstructed using synthetic aperture imaging. In Figure 5.16(d), we show an image reconstructed using the proposed interference-based joint reconstruction method. From Figure 5.16, it can be observed that the proposed method reconstructs cyst and nylon wires with greater accuracy. The diameter of the nylon wires appears much closer to that of the original. Similarly, the speckle noise has been removed. The proposed joint image reconstruction method further improves the resolution of interference-based ultrasound.

In Figure 5.17, we compare images of a high-resolution region of a tissue-mimicking phantom. The ROI includes twelve 0.08-mm-diameter nylon wires. The wires are separated by 4, 3, 2, 1, 0.5, and 0.25 mm in the axial and lateral directions. In Figure 5.17, we show images reconstructed using conventional focused B-mode, plane-wave, synthetic aperture, and interference-based joint reconstruction methods respectively. The proposed method capable to reconstruct nylon wires with less speckle noise and better spatial resolution.

The experimental results shown in Figure 5.16 and Figure 5.17 are consistent with our simulation study shown in Figure 5.5. The image in Figure 5.16(d), was reconstructed using data from ten pulse-echo transmissions of random interference wave. The theoretical temporal resolution of the proposed method is equal to the time required to perform 10 pulse-echo transmissions. However, a significant amount of time required to reconstruct high-resolution images. We use a PC equipped with Intel Xeon Gold 6240R, 256 GB RAM, and an installed MATLAB environment. The maximum size of the array that can be efficiently processed using the available PC is $40 \times 3300 \times 38801$. A single subarray image is reconstructed in about 110 seconds.

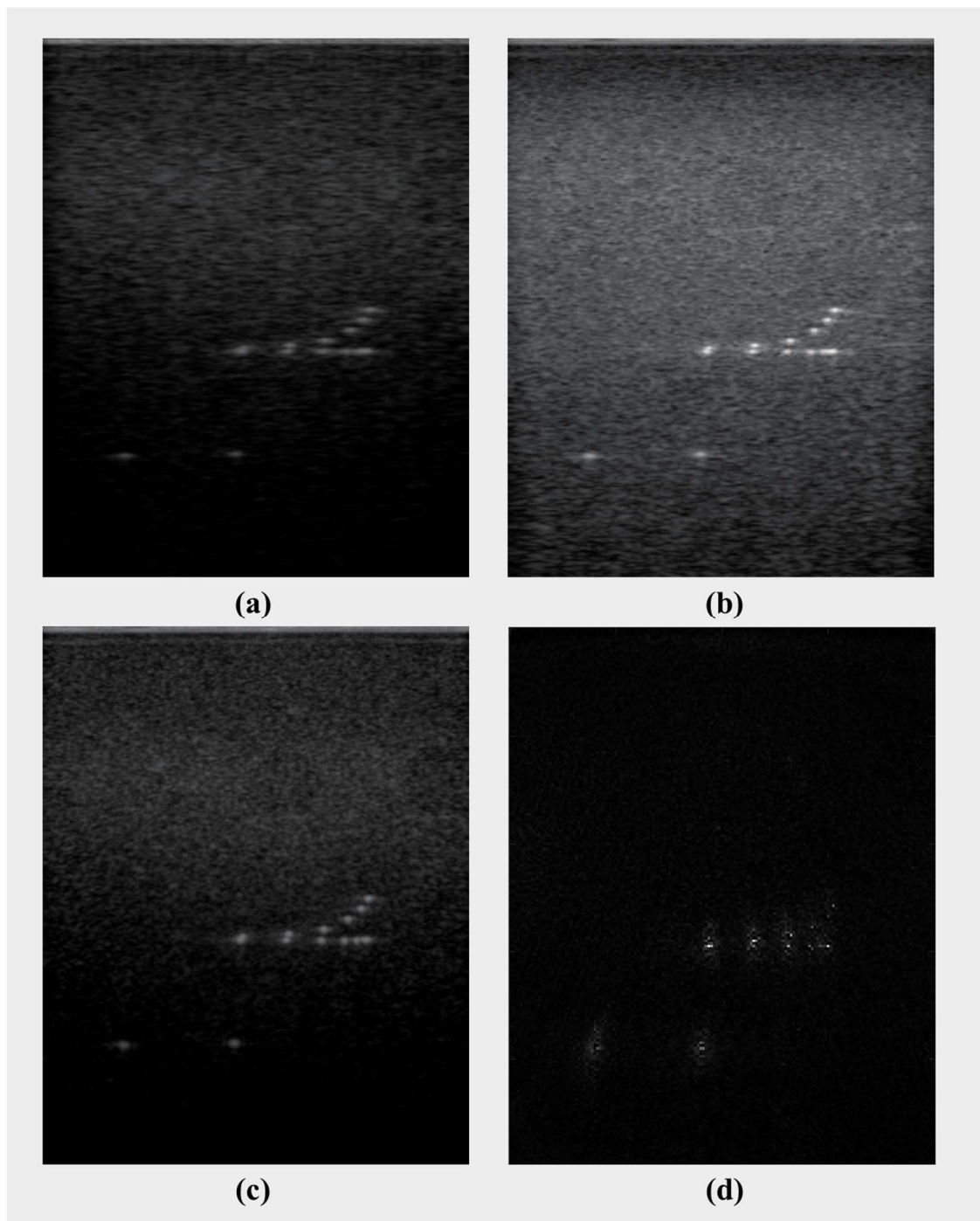


Figure 5.17. Experimental results using tissue mimicking phantom. The ROI includes twelve 0.08-mm-diameter nylon wires. a) conventional B-mode, b) plane-wave mode, c) synthetic aperture, d) joint image reconstructions method using random interference

In this work, we claim that by combining a novel interference-based image acquisition method with a joint image reconstruction algorithm we can achieve very accurate ultrasound images at 0.25 mm resolution with strong SNR and precise SSIM. The proposed joint reconstruction method uses echo signals across all array elements to directly estimate a high-resolution image. The proposed method does not require a focused ultrasound beam, thereby removing the speckle noise caused by diffraction.

Chapter 6

Conclusion

In this work, we have proposed replacing the conventional focused ultrasound pulse with an unfocused ultrasound wavefront of random interference. The proposed method eliminates the need to focus and steer the ultrasound pulse, thereby removing the diffraction resolution limit. Super-resolution images are reconstructed by identifying spatial impulse responses in the echo signals rather than using the conventional approach of visualizing the strength of echo signals. Simulation and experimental results suggest that ultrasound images can be successfully reconstructed by using an ultrasound wavefront of random interference. In the simulation study, the proposed method achieved a resolution of 0.25 mm, representing a four-fold improvement over conventional beamforming-based methods. In the real phantom experiment, we demonstrated that the proposed method can successfully reconstruct ultrasound images of nylon wires as small as 0.08 mm in diameter using a tissue-mimicking phantom.

We believe that the presented analytical and experimental results of this study will unlock a wide range of new ultrasound imaging capabilities. While this study demonstrates only images of sparse objects, an algorithm that reconstructs a three-dimensional image based on *a priori* information would significantly improve the sensing capabilities of random inter-

ference imaging. The remaining challenge in developing such a three-dimensional reconstruction algorithm is to design a method to dynamically generate transmission matrices depending on the structure of the object.

Acknowledgment

It has been a long journey for me in pursuit of knowledge and meaning in my life. I would like to thank my parents, who raised and tough me well, who have always stand by my side, who always will be my best friends and supporters. I would like to thank my brother and my sister who raised me together with my parents and who tough me all the cool things.

I was fortunate to have this opportunity to pursue my Ph.D. degree without ever worrying about paying for tuition. Hence, I would like to extend my gratitude to the Korean Government, all Faculty, and all members of GIST for giving us, the students, this privilege to study for free.

I would like to express my sincere gratitude to my advisor Professor Heung-No Lee. The Professor accepted me as an intern to his research group in 2011 and supported me during my eight long years at GIST. I would also extend my deepest gratitude to the Professors who served on my Ph.D. committee. I truly am thankful for the opportunity to attend your lectures, and to collaborate on research projects.

I am thankful to all fellow students, especially to my lab members who shared with me this beautiful academic year at GIST.

Curriculum Vitae

Name : **Pavel S. Ni** Birth Date: 1987/02/07
E-mail : pni@gist.ac.kr Birth Place: Tashkent, UZ
Permanent Address : 123 Cheomdangwagi-ro (Oryong-dong), Buk-gu, Gwangju

Research Interests

Biomedical Imaging, Deep Learning

Education

2005.9 – 2009.6	B.S.	Electrical Eng.,	Tashkent Univ. of Info. and Tech.
2012.3 – 2021.2	M.S./Ph.D.	Electrical Eng. and CS	Gwangju Inst. of Sci. and Tech.

Korean Patent

1. Pavel S. Ni, and Heung-No Lee, “Apparatus of ultrasound imaging using random interference and method of the same”, No. P20-0073-KR01, 2019.

International Journal Papers (SCI / SCIE)

1. Pavel S. Ni, and Heung-No Lee*, “High-Resolution Ultrasound Imaging Using Random Interference“, IEEE Transactions on Ultrasonics, Ferroelectrics, and Frequency Control (T-UFFC), March. 2020. (Impact Factor: 2.989, Do-Yak project).
2. Pavel S. Ni, Heung-No Lee*, “High-Resolution Ultrasound Imaging Enabled by Random Interference and Joint Image Reconstruction”, Sensors 2020, 20(22), 6434 (Impact Factor: 3.275, Do-Yak project)

International Conference

1. Pavel S. Ni, Heung-No Lee, “Ultrasound Image Reconstruction using Compressive Sensing”, The 39th Annual International Conference of the IEEE Engineering in Medicine and Biology Society, Jeju-do South Korea, July 11-15 2017.
2. Pavel S. Ni, Sangjun Park, and Heung-No Lee, “Design of Unfocused Ultrasound Imaging System using Compressive Sensing”, 37th Annual International Conference of the IEEE Engineering in Medicine and Biology Society, Milan, Italy, August 24-29, 2015.

References

- [1] P. S. Ni and H. N. Lee, "High-Resolution Ultrasound Imaging Using Random Interference," *IEEE Trans. Ultrason. Ferroelectr. Freq. Control*. vol. 67(9), pp. 1785–1799, 2020.
- [2] P. S. Ni and H. N. Lee, "High-Resolution Ultrasound Imaging Enabled by Random Interference and Joint Image Reconstruction", *Sensors*, 20(22), pp. 6434, 2020.
- [3] O. Ramm and S. W. Smith, *Beam Steering with Linear Arrays*. pp. 438-452, 1983.
- [4] A. A. Maznev and O. B. Wright, "Upholding the diffraction limit in the focusing of light and sound," *Wave Motion*, vol. 68, pp. 182-189, 2017.
- [5] A. N. a. J. Swanevelder, "Resolution in ultrasound imaging,". *Contin. Educ. Anaesth. Crit. Care Pain*, vol. 11, pp. 186–192, 2011.
- [6] B. Cox and P. Beard, "Imaging techniques: Super-resolution ultrasound," *Nature*, vol. 527, no. 7579, pp. 451-2, Nov 26 2015.
- [7] T. Szabo, *Diagnostic Ultrasound Imaging—Inside Out*. 2004.
- [8] L. Schermelleh, A. Ferrand, T. Huser, et al. "Super-resolution microscopy demystified". *Nat Cell Biol* 21, 72–84, 2019.
- [9] Young-Don Son, Zang-Hee Cho. et al. "Individually Differentiated Serotonergic Raphe Nuclei Measured with Brain PET/MR Imaging". *Radiology* vol. 272, no. 2, pp 541-548, 2014.
- [10] G. Montaldo, M. Tanter, J. Bercoff, N. Benech, and M. Fink, "Coherent plane-wave compounding for very high frame rate ultrasonography and transient elastography,". *IEEE Transactions on Ultrasonics Ferroelectrics and Frequency Control*, vol. 56, no. 3, pp. 489-506, Mar. 2009.
- [11] J. A. Jensen, S. I. Nikolov, K. L. Gammelmark, and M. H. Pedersen, "Synthetic aperture ultrasound imaging,". *Ultrasonics*, vol. 44, pp. E5-E15, Dec 22, 2006.
- [12] J. F. Synnevag, A. Austeng, and S. Holm, "Adaptive beamforming applied to medical ultrasound imaging,". *IEEE Transactions on Ultrasonics Ferroelectrics and Frequency Control*, vol. 54, no. 8, pp. 1606-1613, Aug. 2007.
- [13] J. Kang, J. Y. Lee, and Y. Yoo, "A new feature-enhanced speckle reduction method based on multiscale analysis for ultrasound b-mode imaging,". *IEEE Transactions on Biomedical Engineering*, vol. 63, no. 6, pp. 1178-1191, Jun. 2016.

- [14] P. C. Tay, C. D. Garson, S. T. Acton, and J. A. Hossack, "Ultrasound despeckling for contrast enhancement," *IEEE Transactions on Image Processing*, vol. 19, no. 7, pp. 1847-1860, Jul. 2010.
- [15] I. Trots, Y. Tasinkevych, A. Nowicki, and M. Lewandowski, "Golay coded sequences in synthetic aperture imaging systems," *Archives of Acoustics*, vol. 36, no. 4, pp. 913-926, 2011.
- [16] P. Gong, M. C. Kolios, and Y. Xu, "Delay-encoded transmission and image reconstruction method in synthetic transmit aperture imaging," *IEEE Trans Ultrason Ferroelectr Freq Control*, vol. 62, no. 10, pp. 1745-56, Oct. 2015.
- [17] Candès, E.; Romberg, J.; and Tao, T. Robust uncertainty principles: Exact signal reconstruction from highly incomplete frequency information. *IEEE Trans. on Information Theory*, 2006, 52(2) pp. 489–509.
- [18] Candès, E.; Romberg, J. Quantitative robust uncertainty principles and optimally sparse decompositions. *Foundations of Comput. Math.*, 2006, 6(2), pp. 227–254.
- [19] D. L. Donoho, "Compressed sensing," *IEEE Transactions on Information Theory*, vol. 52, no. 4, pp. 1289-1306, Apr. 2006.
- [20] R. G. Baraniuk, "Compressive sensing," *IEEE Signal Processing Magazine*, vol. 24, no. 4, pp. 118-121, Jul. 2007.
- [21] E. J. Candes and M. B. Wakin, "An introduction to compressive sampling," *IEEE Signal Processing Magazine*, vol. 25, no. 2, pp. 21-30, Mar. 2008.
- [22] Baboulaz, L.; Dragotti, P. L. Exact feature extraction using finite rate of innovation principles with an application to image super-resolution. *IEEE Trans. Image Process.*, 2009, 18(2), pp. 281–298.
- [23] Jung, H.; Sung, K.; Nayak, K.S.; Kim, E.Y.; Ye, J.C. k-t FOCUSS: A general compressed sensing framework for high resolution dynamic MRI. *Magn Reson Med*, 2009.
- [24] Herman, M.A.; Strohmer, T. High-resolution radar via compressed sensing. *IEEE Trans. Signal Process.*, 2009, 57(6), pp. 2275–2284.
- [25] Oliver, J.; Lee, W.B.; Park, S.J.; Lee, H.N. Improving resolution of miniature spectrometers by exploiting sparse nature of signals. *Opt. Express*, 2012, 20(3), pp. 2613–2625.

- [26] Jang, H.; Yoon, C.H.; Chung, E.H.; Choi, W.S.; Lee, H.N. Speckle suppression via sparse representation for wide-field imaging through turbid media. *Opt. Express*, 2014, 22(13), pp. 16619–16628.
- [27] Mishra, K. V.; Cho, M.; Kruger, A.; Xu, W. Spectral super-resolution with prior knowledge. *IEEE Trans. Signal Process.*, 2015, 63(20), pp. 5342–5357.
- [28] Lee, W.B.; Jang, H.C.; Park, S.J.; Song, Y.M.; and Lee, H.N. COMPU-EYE: A high resolution computational compound eye. *Opt. Express*, 2016, 24(3), pp. 2013–2026.
- [29] N. Wagner, Y. C. Eldar, A. Feuer, G. Danin, and Z. Friedman, "Xampling in ultrasound imaging," in *SPIE Medical Imaging*, 2011, vol. 7968, p. 17: SPIE.
- [30] N. Wagner, Y. C. Eldar, and Z. Friedman, "Compressed beamforming in ultrasound imaging," *IEEE Transactions on Signal Processing*, vol. 60, no. 9, pp. 4643–4657, Sep. 2012.
- [31] J. F. Yang and Y. Zhang, "Alternating direction algorithms for L1-problems in compressive sensing," *Siam Journal on Scientific Computing*, vol. 33, no. 1, pp. 250–278, 2011.
- [32] W. Y. W. Deng, and Y. Zhang, "Group sparse optimization by alternating direction method," *Rice CAAM Report*, vol. TR11-06, 2011.
- [33] Goodman, J. W. Some fundamental properties of speckle. *J. Opt. Soc. Amer.*, 1976, 66(11), pp. 1145–1150.
- [34] Burckhardt, C. B. Speckle in ultrasound B-mode scans. *IEEE Transactions on Sonics and Ultrasonics*, 1978, 25(1), pp. 1–6.
- [35] Abbott, J. G.; Thurstone, F. L. Acoustic speckle: Theory and experimental analysis, *Ultrasound Imag.*, 1979, 1, pp. 303–324.
- [36] J. A. Jensen, "Linear description of ultrasound imaging systems," *Notes for the International Summer School on Advanced Ultrasound Imaging, Technical University of Denmark*, June 10, 1999.
- [37] J. A. Jensen and N. B. Svendsen, "Calculation of pressure fields from arbitrarily shaped, apodized, and excited ultrasound transducers," *IEEE Trans Ultrason Ferroelectr Freq Control*, vol. 39, no. 2, pp. 262–7, 1992.
- [38] J. A. Jensen, "Field: A Program for Simulating Ultrasound Systems," *Medical & Biological Engineering & Computing*, vol. 34, pp. 351–353, 1996.
- [39] J. Liu, Q. He, and J. Luo, "A compressed sensing strategy for synthetic transmit aperture ultrasound imaging," *IEEE Trans Med Imaging*, vol. 36, no. 4, pp. 878–891, Apr. 2017.

- [40] G. David, J. L. Robert, B. Zhang, and A. F. Laine, "Time domain compressive beam forming of ultrasound signals," *J Acoust Soc Am*, vol. 137, no. 5, pp. 2773-84, May. 2015.
- [41] P. Song, A. Manduca, J. D. Trzasko, R. E. Daigle, and S. Chen, "On the effects of spatial sampling quantization in super-resolution ultrasound microvessel imaging," *IEEE Trans Ultrason Ferroelectr Freq Control*, May 4 2018.
- [42] P. F. Song *et al.*, "Improved super-resolution ultrasound microvessel imaging with spatiotemporal nonlocal means filtering and bipartite graph-based microbubble tracking," *IEEE Transactions on Ultrasonics Ferroelectrics and Frequency Control*, vol. 65, no. 2, pp. 149-167, Feb 2018.
- [43] G. T. Clement, J. Huttunen, and K. Hynynen, "Superresolution ultrasound imaging using back-projected reconstruction," *J Acoust Soc Am*, vol. 118, no. 6, pp. 3953-60, Dec 2005.
- [44] D. Stork and A. Ozcan, *Imaging Without Lenses*. 2018, p. 28.
- [45] A. Liutkus *et al.*, "Imaging with nature: Compressive imaging using a multiply scattering medium," *Scientific Reports*, Article vol. 4, p. 5552, 07/09/online 2014.
- [46] H. Jang, C. Yoon, E. Chung, W. Choi, and H. N. Lee, "Speckle suppression via sparse representation for wide-field imaging through turbid media," *Optics Express*, vol. 22, no. 13, pp. 16619-16628, Jun 30, 2014.
- [47] Y. Choi *et al.*, "Overcoming the diffraction limit using multiple light scattering in a highly disordered medium," *Physical Review Letters*, vol. 107, no. 2, Jul 6, 2011.
- [48] P. v. d. M. Pieter Kruizinga*, Andrejs Fedjajevs, Frits Mastik, Geert Springeling, Nico de Jong, Johannes G. Bosch and Geert Leus, "Compressive 3D ultrasound imaging using a single sensor," *Science Advances*, vol. 3, Dec 08, 2017.
- [49] Y. B. Xie *et al.*, "Acoustic holographic rendering with two-dimensional metamaterial-based passive phased array," *Scientific Reports*, vol. 6, Oct 14, 2016.
- [50] P. Ni, S. Park, and H.-N. Lee, "Design of unfocused ultrasound imaging system using compressive sensing," *37th Annual International Conference of the IEEE Engineering in Medicine and Biology Society (EMBC'15)*, Poster 2015.
- [51] M. D. Brown, D. I. Nikitichev, B. E. Treeby, and B. T. Cox, "Generating arbitrary ultrasound fields with tailored optoacoustic surface profiles," *Applied Physics Letters*, vol. 110, no. 9, Feb 27, 2017.

- [52] S. J. Kim, K. Koh, M. Lustig, S. Boyd, and D. Gorinevsky, "An interior-point method for large-scale l_1 -regularized least squares," in *IEEE Journal of Selected Topics in Signal Processing*, vol. 1, no. 4, pp. 606-617, Dec 2007.
- [53] S. S. B. Chen, D. L. Donoho, and M. A. Saunders, "Atomic decomposition by basis pursuit," *Siam Review*, vol. 43, no. 1, pp. 129-159, Mar 2001.
- [54] S. Park and H. N. Lee, "Fast mixed integer quadratic programming for sparse signal estimation," in *IEEE Access*, vol. 6, pp. 58439-58449, 2018.
- [55] A. Nowicki, Z. Klimonda, M. Lewandowski, J. Litniewski, P. A. Lewin, and I. Trots, "Comparison of sound fields generated by different coded excitations - Experimental results," in *Ultrasonics*, vol. 44, no. 1, pp. 121-129, Jan 2006.